ARISTOTLE UNIVERSITY OF THESSALONIKI
FACULTY OF SCIENCES
SCHOOL OF GEOLOGY
DEPARTMENT OF GEOLOGY

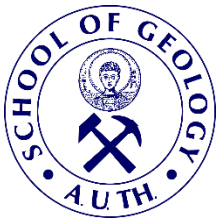

IOANNIS KARAMITROS

Geologist

APPLICATIONS OF TERRESTRIAL LASER SCANNING TECHNOLOGY IN STRUCTURAL GEOLOGY

MASTER THESIS

THESSALONIKI
2016

ΑΡΙΣΤΟΤΕΛΕΙΟ ΠΑΝΕΠΙΣΤΗΜΙΟ ΘΕΣΣΑΛΟΝΙΚΗΣ
ΣΧΟΛΗ ΘΕΤΙΚΩΝ ΕΠΙΣΤΗΜΩΝ
ΤΜΗΜΑ ΓΕΩΛΟΓΙΑΣ
ΤΟΜΕΑΣ ΓΕΩΛΟΓΙΑΣ

ΙΟΑΝΝΗΣ ΚΑΡΑΜΗΤΡΟΣ

Πτυχιούχος Γεωλόγος

ΕΦΑΡΜΟΓΕΣ ΤΗΣ ΤΕΧΝΟΛΟΓΙΑΣ TERRESTRIAL LASER SCANNING ΣΤΗΝ ΤΕΚΤΟΝΙΚΗ ΓΕΩΛΟΓΙΑ

ΜΕΤΑΠΤΥΧΙΑΚΗ ΔΙΑΤΡΙΒΗ ΕΙΔΙΚΕΥΣΗΣ

ΘΕΣΣΑΛΟΝΙΚΗ

2016

Ioannis Karamitros

Geologist

APPLICATIONS OF TERRESTRIAL LASER SCANNING TECHNOLOGY IN STRUCTURAL GEOLOGY

Programme of Postgraduate Studies

Geology and Geoenviroment

Structural Geology and Stratigraphy

Advisory Committee:

Assistant Professor Alexandros Chatzipetros, Advisor

Professor Spyros Pavlides, Advisory Committee Member

Lecturer Antonios Mouratidis, Advisory Committee Member

Table of Contents

Preamble 6

Background 6

Objectives 6

Acknowledgements 8

1. Introduction 10

2. Methodology 11

2.1. Basic Principles of LIDAR Technology 11

2.1.1. Information about LIDAR systems 11

2.1.2. Terrestrial Laser Scanning Systems 13

2.1.3. LIDAR Applications in Geology 16

2.2. Examples of LIDAR applications in geology 18

2.3 Software used 22

2.4 Methodology 25

2.4.1. Point Cloud Classification 25

2.4.2. Morphological Analysis and Morphotectonic Parameters 27

2.4.3. Normal Computation 27

2.4.4. Curvature Analysis 28

2.4.5. Surface Roughness 30

2.4.6. Planar Facets Analysis 31

3. Regional Setting and Methodology 31

3.1. Heraklion Basin – Stavrakia Fault 31

3.1.1. Regional Setting 31

3.1.2. Methodology 36

3.2. Tyrnavos and Gyrtoni Faults 48

3.2.1. Regional Setting 48

3.2.2. Methodology 54

3.2.2.1 Data Acquisition 54

3.2.2.2 Data Processing 56

3.3. Messinia Basin – Pidima Fault 59

3.3.1. Regional Setting 59

3.3.2. Methodology 62

3.4. Petrified Forest of Lesvos Island 78

3.4.1. Regional Setting 78

3.4.2. Methodology 81

4. Conclusions 86

4.1. Discussion of Results and future work 86

4.2. Concluding remarks 88

5. References 92

Appendix 96

Preamble

Background

The assignment of this Master Thesis has taken place in February 2015 and the advisory committee was assigned on 27 November 2015 and had its title and language changed to English at 12 of June 2016. It consists of Ass. Professor Alexandros Chatzipetros, as supervisor, and Professor Spyridon Pavlides and Lecturer Antonis Mouratidis as members, based on their research experience and the multidisciplinary aspects of this Thesis.

Objectives

The aim of this Master Thesis is to examine the possibilities of integration of LIDAR (Light Detection and Ranging) and point cloud creation technologies in general, to Stuctural Geology. As LIDAR offers a lot of new tools for the science of Geology, there is an increased demand on methods that utilize these tools. There are new and older software platforms that try to fit that role and provide the researcher with a new arsenal to use for his needs. This Master Thesis attempts to explore the possibilities of LIDAR technologies in assisting with the current geological methods of analysis, as well as, the emergence of new ones. Also, apart from just listing the current developments in the geological approach of LIDAR, the application of existing methods and also new approaches on them was attempted on existing point clouds.

In order to achieve the abovementioned Thesis goals, an extensive bibliographic review was first made on articles concerning geological applications in association with point clouds of surfaces and objects of geological interest. In addition, research was also done on improving traditional geological methods of analysis using terrestrial scanning methods. Several methods were chosen for testing, along with some software platforms, in order to create a methodology compatible with the resources available at the host institute (Department of Geology, Aristotle University of Thessaloniki). Data from scanning expeditions of 2014 was available and was supplemented with point cloud data from two fault systems that was acquired during the period of the Master studies. The Stavrakia fault

in Crete and Pidima fault in Messinia surveyed in the framework of this Thesis and were chosen as the prime targets of the structural analysis methods that were tested. The methods applied were chosen for point cloud editing and tectonic analysis of geological features. The final step was to evaluate the level that LIDAR technologies have helped improving geological research, in addition discuss the results of the methods used for this Master Thesis.

Acknowledgements

I take this opportunity to gratefully acknowledge the contribution of those who made this thesis possible. First of all, I would like to thank my supervisors Ass. Prof. Alexandros Chatzipetros, Prof. Spyros Pavlides and Lecturer Dr. Antonios Mouratidis for their confidence, encouragement, support, advice and help. I am especially grateful to Dr. Haralambos Fassoulas and the Natural History Museum of Crete for providing the funds and valuable information for the field trip in the Stavrakia fault area in Crete. Additionally, I would like to acknowledge Dr. Athanasios Ganas, Prof. Ioannis Koukouvelas and Dr. Vasiliki Zygouri attribution in the Pidima fault scanning sessions and information about the two cites that we visited there.

For the valuable data that was provided for the current Master Thesis, for the Tyrnavos – Gyrtoni areas I would like to thank Prof. Riccardo Caputo, Prof. Bruno Helly, Prof. Ioannis Koukouvelas, Ilias Lazos and Dr. Ioannis Tsodoulos and for the Petrified forest of Lesvos, Ass. Prof. Nikos Zouros and The Natural History Museum of the Lesvos Petrified Forest, Dr. Triantafyllos Kaklis, Prof. Demosthenis, Mountrakis, Anastasios Plougarlis, Vasilis Rozakis and Dr. Efimia Thomaidou.

During the course of my Master studies and Thesis, I am also thankful for various discussions, advice and encouragement of Pr. Markos Tranos, Giorgos Georgiadis, Petros Neofotistos, Anastasios Plougarlis, Dr Vagelis Vlachos, Vaios Vlachos, Georgia Kostaki, Aliki Kokkala and Giouli Venetsanou. I cannot continue without giving my thanks to my close colleagues Ilias Lazos and Maria Chatzopoulou for their support and advice they provided me during all this time. For his invaluable help in the building of my Master Thesis I would like to give special thanks to Dr. Stratos Delogos.

I wish to thank my family and my friends for their love and support. I can also never thank enough my close friend and colleague Christina for her encouragement and support.

Thank you all very much!

Giannis

1. Introduction

For this Master Thesis five areas were chosen for study due to their availability of point cloud data and research interest, all of them in Greece. All of the areas, apart from one, were chosen for their neotectonic significance.

Figure 1. Map of Greece with the areas that provided the laser data; 1. Stavrakia-Siva fault, Crete 2. Tyrnavos Palaeoseismic trench, 3. Gyrtoni fault, 4. Pidima fault and Palaeoseismic trench, 5. Lesvos Petrified Forest Geopark.

For their data availability, Tyrnavos and Gyrtoni areas in Thessaly basin and Sigri area in Lesvos Island were chosen due to the fact that data scans had already been made for research purposes, but had not been analyzed until the initiation of this Master Thesis. Tyrnavos and Gyrtoni villages in Thessaly (central Greece) are in close proximity from two fault zones named after them. Any additional information about these fault zones has great

value as it may help in understanding more about fault behavior and therefore conduct a more complete analysis of this area. On the other hand, Sigri area contained mostly fossilized tree trunks, scanned mostly for visualization purposes, but only a few small faults of unknown neotectonic importance.

For the purpose of this Master Thesis, two other areas were chosen for their Neotectonic significance, the Stavrakia-Siva area in Heraklion basin, Crete Island, and Pidima village in Messinia basin, Peloponnesus. Both areas are dominated by highly active fault zones, each one close to a major city of Greece, and therefore of significant fundamental and applied research value. The Stavrakia-Siva area demonstrates a large, kilometer scale, fault escarpment covering most of the Northwestern boundaries of Heraklion basin in Crete, reaching on its north part the area close to Heraklion City, the fourth largest city in Greece. The Pidima Vilage fault zone in Messinia Prefecture is also kilometer scale and in contrast with the Stavrakia-Siva fault, demonstrates a few fault plane surfaces allowing for more detailed fault analysis. Specifically designed field trips were made in order to acquire new data and test the applied practices.

2. Methodology

2.1. Basic Principles of LIDAR Technology

2.1.1. Information about LIDAR systems

LIDAR is a remote sensing technology and is an acronym of "Light Detection and Ranging". LIDAR systems operate by emitting intense, focused beams of light to a target, in order to measure the time it takes for the reflected light to be detected by the sensor and finally compute where the object is located in three dimensions (Schmid *et al*., 2012). The information collected is used to calculate the distance between the device and the target and can have a wide range of ground point sampling densities and rapidly record them, in 3D models, at detailed resolutions and with high spatial precision. Moreover, the fact that LIDAR is illuminating a target with a laser and analyzing the reflected light allows scan data to be collected during the night, when the conditions are usually more favorable.

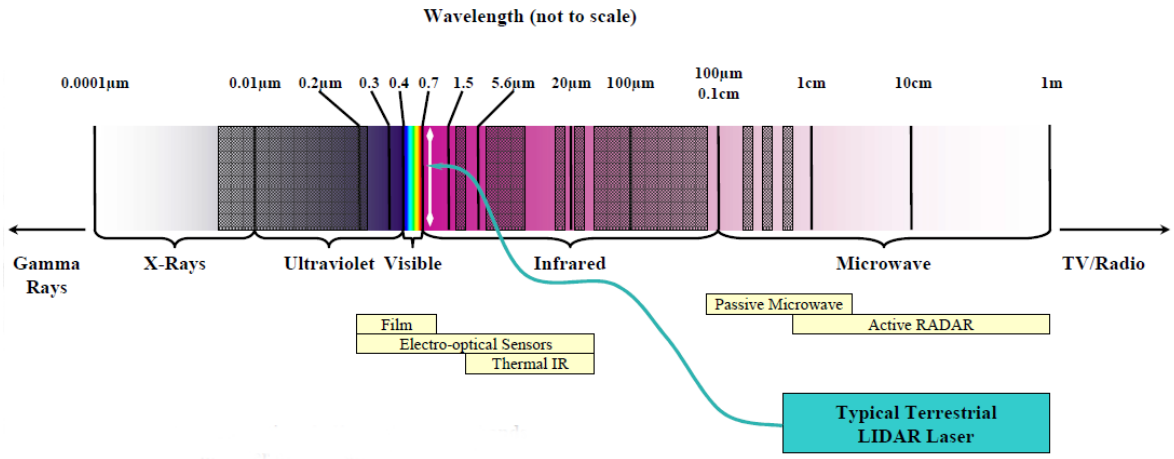

Figure 2. The Electro-Magnetic Spectrum showing the wavelengths that the average TLS is using. Greyed sections indicate significant bands of water or atmospheric absorption (taken from Mike Renslow, Spencer B. Gross, Inc.)

LIDAR technology was developed over 40 years ago as a fixed -position ground- based instrument for studies of atmospheric composition, structure, clouds, and aerosols (Schmid *et al.*, 2012). It was later introduced to the engineering community for the collection of range data and as the LIDAR industry matured, the quality and capabilities of the technology rapidly advanced (Fowler *et al.*, 2011). During the 1980s, with the development of GPS and the use of moving sensors, airborne LIDAR was created and one of its first uses was for collecting bathymetric data. This LIDAR system operates in the green color band to penetrate water and detect bottom features and can be used in areas with relatively clear water to measure seafloor elevations. In the early 1990s the improvement of the inertial measurement unit (IMU) brought the ability of achieving decimeter accuracies. As an example, one the earlier non-bathymetric airborne applications that were used during that period were in the measurement of glaciers and how they were changing. Ground-based LIDAR (terrestrial scanning) is starting to be used as a way to densely map the three-dimensional nature of features and ground surfaces to an extremely high level of accuracy (Schmid *et al.*, 2012).

Nowadays, there are two major categories of LIDAR technology, the TLS (Terrestrial Laser Scanning) or T- LIDAR and the airborne LIDAR. In this Master Thesis we will be focusing on TLS, which is a ground-based form of LIDAR as it is a versatile tool, with a very wide range of applications within geosciences mainly due to the fact that it has high resolution, accuracy and ease of dataset integration of topographic and other surfaces.

2.1.2. Terrestrial Laser Scanning Systems

A TLS system can be mobile or stationary, depending on the target and the area that must be covered. The device operates with the same principles as all LIDAR systems, by emitting a laser pulse at known azimuth and an angle of inclination relative to the scanner towards an object or surface. As mentioned above, the surfaces reflect the electromagnetic waves and the receiver detects portions of the backscattered signal. The time of flight of the emitted pulse and its reflected, returning counterpart is used to calculate the distance between the tripod-mounted laser scanner and a surface. This can be achieved because the speed of light is a known constant. The scanner emits thousands of pulses per second and incrementally is adjusting the direction, horizontally and vertically to sample reflections within its 360° horizontal and 90° vertical line of sight (Bubeck *et al*., 2015; Wilkinson *et al*., 2010). In order for this process to work, the transmitter and the receiver must be located at the same location. The resulting product is a densely spaced network of elevation points based on the Cartesian coordinates (x, y, z) of the reflected points, called **point cloud**. These three-dimensional coordinates of the target objects are computed from the time difference between the laser pulse being emitted and returned in association with the starting angle of the pulse and the absolute location of the sensor on or above the surface of the Earth.

Figure 3. The Optech ILRIS-3D while in a scanning session during an expedition in Crete (2015) in the framework of this Thesis.

Most of TLS technology allows a maximum reliable survey range of about one kilometer (e.g. Optech, 2008; Riegl, 2008) and can produce point data with centimeter or even millimeter accuracy in some cases. This characteristic is the reason why they are often used for localized terrain-mapping applications that require frequent surveys. The instrument resolution is often controlled by an imaginary plane located at the middle range of the vertical field of view and is orthogonal to the sensor's normal sight. The range of the ground point sampling densities is relevant to the scan angle, the average point density of individual scans and the degree of overlap between scans. TLS devices can collect millions of points in few minutes with a high accuracy (for example, 7mm at 100m distance for an ILRIS-3D, from Optech Inc., according to the manufacturer's specifications) in order to acquire a point cloud which can be incorporated into the analysis and interpretation of field data. The created point cloud datasets, constitute an accurate representation of the real world landscape with point spacing of 10mm at 100m range, often comprised of millions, even billions, of data points. As the scanner can only record data in its line of sight, surveying with large vertical angles covers more area and often yields shorter survey times, but at the expense of point sampling density. Multiple scans can be used to collect data over the same geographical location

resulting in increased sampling density and often overcome problems such as shadowing and limited coverage due to vegetation. The resultant point clouds are subsequently aligned and merged based on the identification of overlapping zones and are typically assisted by algorithms implemented within commercial software. Most of these algorithms are based on least-squares surface matching or iterative closest points.

Some laser scanner models are capable of measuring the reflectivity of the material of the target and incorporate them in the data as intensity values. Intensity is the measure of the reflection strength of the laser pulse upon returning to the laser scanner. The intensity is dependent on the reflectivity of the target material, range to the target (due to beam divergence of the laser as the laser pulse becomes wider and less intense with distance) and atmospheric conditions (presence of dust, rain, humidity levels, etc.) (*Hodgetts*, 2013). Higher return intensities are associated with relatively smooth, highly reflective surfaces, while the lower values with darker, as they absorb more of the laser energy, and rougher surfaces because they scatter some of the energy away from the sensor. A smooth reflective surface, however, may also produce lower intensity returns if it is tilted away from the direction of the incoming light pulse and thus reflects most of the energy away from the sensor (MicroImages.org/Lidar, October 2010).

In our study, we used the laser ranging system ILRIS 3D from Optech Inc., Ontario, Canada. The laser scanner was accompanied with additional equipment, such as a self-rotating and tilting base for the scanner, a mounting tripod and a power generator for producing power in the field. Advantages of using this system are its flexible handling, quick availability of a data set with a recording frequency of 2500 points per second, and very high spatial resolution of the data set (depending on the range between scanner and object). Information about reflected laser beam intensity ranges between 0 (low) and 255 (high) without scale unit and the spatial information is recorded in x–y–z-coordinates. The quality of the reflection data depends on the inclination angle of the laser beam, the range between the object and scanner, the material, the color, the surface condition and the spatial resolution.

2.1.3. LIDAR Applications in Geology

The integration of LIDAR in geology has been inevitable as it fills the need for accurate high resolution geological maps and orientation measurements in both industry and research. LIDAR is one of the most effective tools available for the collection of detailed and accurate geological data. Even though it is far from being a replacement for traditional fieldwork, LIDAR technology is a powerful tool to the field geologist's arsenal.

The technique is a non-intrusive visual recording system, and the high spatial and temporal resolution makes it an effective method for morphological reconstructions of geological settings, monitoring, numerical modelling of geological phenomena (Schumann *et al*., 2011; Hu *et al*., 2012; Wiatr *et al*., 2013). In addition, when combined with close-range photogrammetry, enables advanced analysis of weathering and classification of material types in three dimensions. With scaled reflectance, it is possible to determine material types directly from the laser information as well as assess weathering. The increase in data acquisition rates and subsequent reduction of time to scan enables documentation of critical areas for time-sensitive applications. Online waveform analysis enables access to advanced scientific functionality for any user in the field to maximize range, precision and penetration of vegetation (Schmid *et al*., 2012).

The advantages in terms of accuracy and spatial resolution are allowing a growing number of studies to focus more on quantitative research problems, in a way that was impossible using traditional field data alone (e.g. Enge *et al*., 2007; Sagy *et al*., 2007). The biggest advantage, though, of using LIDAR technology is the ease of robust data collection in the field, either by completing data acquisition within a short period of time or providing an alternative data source in terrain inaccessible to direct field site investigation. Collection of elevation data using LIDAR has several advantages over most other techniques. Chief among them are higher resolution, centimeter to millimeter accuracies, and increased ground detection in forested terrain. During the last decade, there has also been a proliferation of articles on this subject, both on techniques and applications, discussing the benefits of digital data acquisition and collection approaches. A variety of attributes like intensity, color, dip, azimuth, co-linearity, co-planarity, is considered as an aid to both manual and automated interpretation approaches.

This technology can generate digital elevation models or virtual outcrop models, either of which retain a wealth of quantitative information (e.g., x, y, and z coordinate values). This results in a virtual model that is suitable for interpretation, digitization and quantitative geological analysis (Buckley *et al*., 2008) such as morphological, structural and sedimentological information. These LIDAR -generated quantitative data can be exported into various software platforms for different kinds of geological analyses.

It has already become an established method for collecting very dense and accurate elevation data across landscapes, shallow-water areas, and project sites. In addition, LIDAR systems are already being used to map viticulture, reconstruct architecture digitally in three dimensions (3D) and monitor slope stability in unprecedented spatial resolution. The technology used is extremely promising for the rapid collection of large amounts of data with various applications to open pit mine sites.

Applications of LIDAR technology, within the fields of structural geology and geomorphology, include measuring structural data from bedding planes and faults, detailed mapping of fault scarps, geologic outcrops, progressive hard rock coastal cliff erosion (Rosser *et al.*, 2005), sedimentological-stratigraphic investigation or even tracing key stratal surfaces between outcrop logs, fault-surface roughness and fracture characterization. Visualizing the model allows the geologist to view parts of the outcrop that are not normally accessible, such as areas of outcrop that cannot be reached or examined from afar or cliff sections flanked by water, and the ability to zoom rapidly in and out from the outcrop provides perspective at different scales of observation. Elevated vantage points can often give a clearer view of stratigraphy, and it is useful to be able to navigate quickly to the exact viewpoint that shows how structures of other geological features are aligned in 3D.

From a virtual outcrop model, information can be derived about facies distribution or lateral variations in stratigraphy, turbidite architectures; the fold geometry, fracture orientation, density and connectivity, and their relation to fold closures and generate 3D fracture distributions (Jones *et al*., 2008). The method, however, shows its true potential in hard to access outcrops or where there is the interference of magnetic fields in deposits of magnetic mineral, that is, magnetite, ilmenite, pyrrhotite, and so on; traditional methods (compass and clinometers) may lead to errors, making it difficult and distorting the

generation of geological models. Therefore, it is necessary to build a methodology for planning, collecting and processing data for geometric data modeling of geological structural plans with the use of TLS. In addition, 3D outcrop models may be used virtually with the support of visualization techniques, making it easier by contributing to cost reduction and planning TLS has become increasingly popular in geomorphologic studies; however, its application in parametric/geometric study of outcrops still needs to be improved. These improvements are related, directly, to the identification and interpretation of geological features, as well as the parameterization of structures in digital outcrop models (DOMs), generated from a dense cloud of three-dimensional points.

Moreover, a very useful application of LIDAR in fault surfaces, includes the measurement of successive micro-scale, postseismic surface motions by repeated data acquisition over a survey time span (Wilkinson, 2012).

Finally, more examples of the integration of this technology in geosciences is its use in the detailed mapping of volcanoes, lava flow, dikes, fissures, glaciers, columnar joints, hillslopes and drainage morphology.

2.2. Examples of LIDAR applications in geology

The innovations that occurred in technology associated with LIDAR in the last decades allowed a wide array of applications in the field of geology. In the last decade there has been a plethora of publications regarding the use and integration of LIDAR systems in the field of geosciences and the number is rapidly increasing each year. There are numerous examples of research around the world regarding this project, however, in this study we will be focusing on papers that are associated with terrestrial laser scanner.

Many researchers have tried to outline possible applications of terrestrial scanning in Geosciences and the integration of numerous other technologies in these methods. Fowler et al., 2011, give a few examples like the combination of LIDAR technology with close-range photogrammetry and relative reflectance, advanced detection of weathering and material classification via reflectance. Those methods proved very useful in 3D model interpretation and showed that this technology can be a great asset in industry and mining operations.

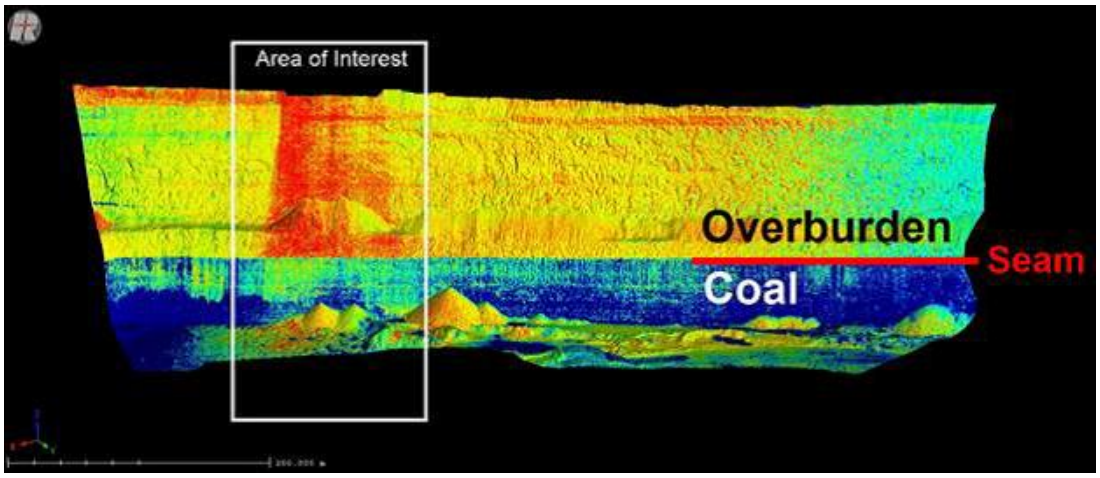

Figure 4. Coal mine high wall mesh colorized by relative reflectance. The material reflectance is exported by the laser as intensity values. (Fowler et al., 2011)

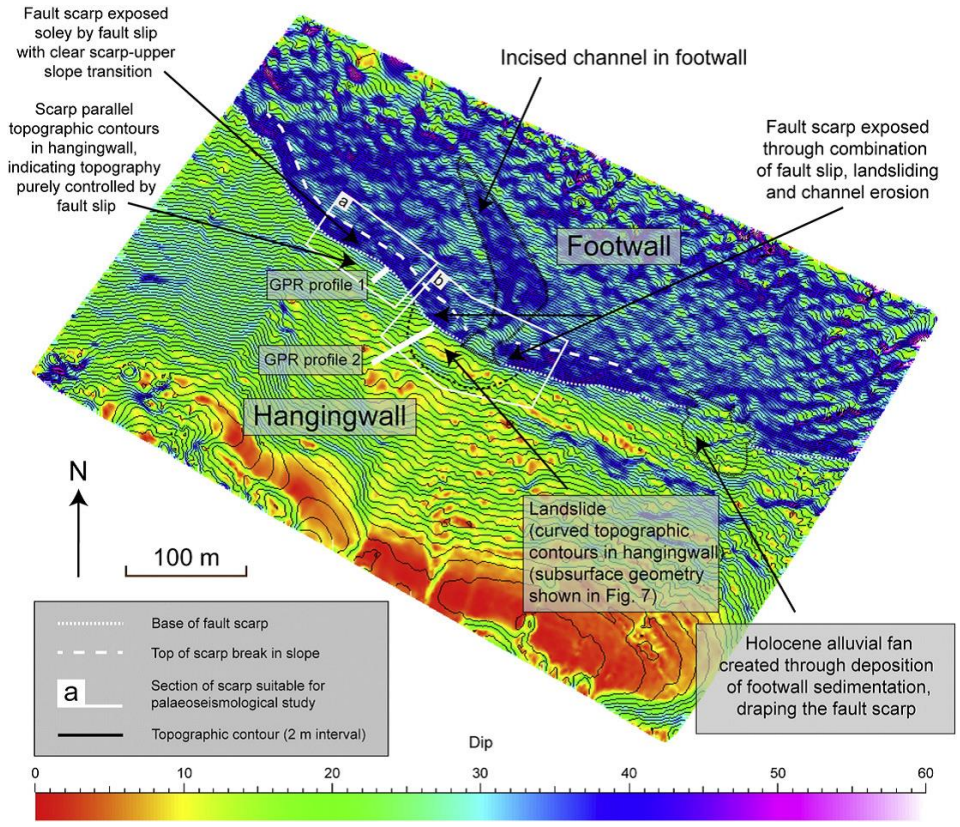

Figure 5. Fiamignano fault scarp surface raster coloured by slope angle, created by discrete smooth interpolation (DSI) of the points2grid(open source software) xy minimum z pseudo-vegetation filter with 4m map spacing between points output using the original TLS Fiamignano fault dataset. Dark shades are steeply dipping and lighter shades are shallow dipping. (Bubeck et al., 2015)

One great example of work with terrestrial laser scanning is in the Central Italian Apennine mountain range by Bubeck *et al*. (2015). The focus of the project was to map the tectono-geomorphic features (Fig. 5) that contribute to the morphology of bedrock scarps. This was done in association with the area's active extensional faulting using TLS and GPR (Ground Penetrating Radar). The goal was to estimate the way these processes can be differentiated to identify locations suitable for the estimation of fault slip-rates. This work also showed that LIDAR technology combined with GPR can give a much better understanding and has a lot of potential for geological analyses in fault zones.

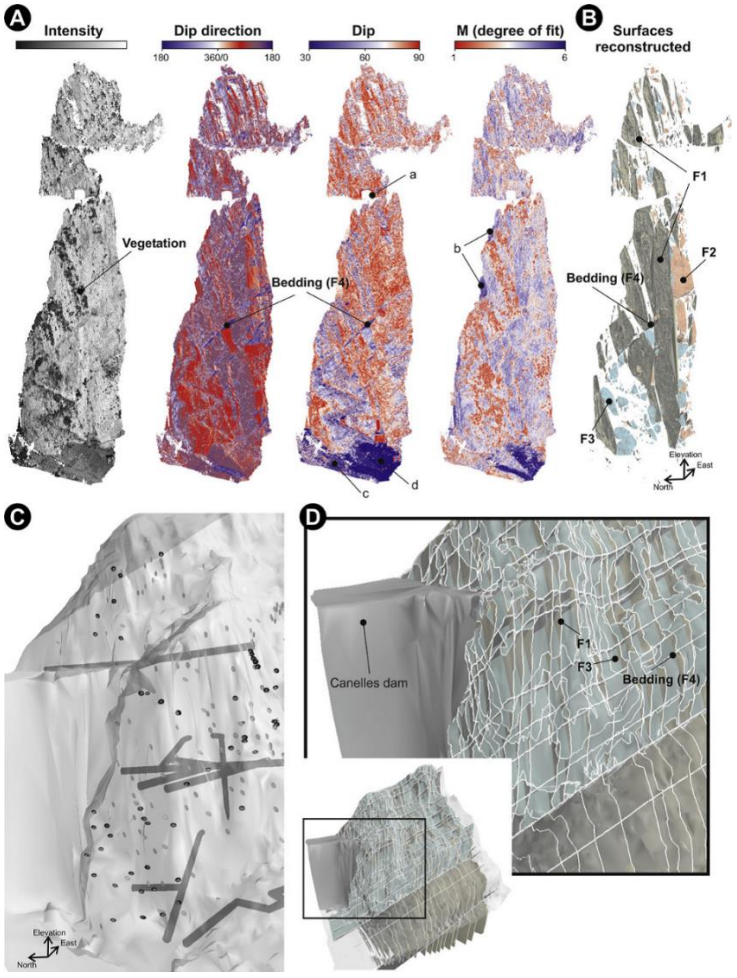

Figure 6. A) Point cloud colored by intensity and other attributes computed with the planar regression routine. (B) Surfaces reconstructed after the cluster filter bedding (F4) and three fracture orientations (F1,F2, and F3). (C) Location of attitude data (circular disks) collected from the field and artificial galleries related to the reservoir dam (grey cylinders); the light grey surface corresponds to the coarse digital elevation model shown with transparency. (D) Final model used for simulating flow after the extrapolation of the main discontinuity planes observed in the outcrop (F1,F3, and bedding) inside the terrain and clipped by the present-day topography(García-Sellés et al., 2011).

García-Sellés *et al*. (2011), tried to create a workflow for a both supervised or automated identification and reconstruction of near-planar geological surfaces that have a three-dimensional exposure in an outcrop (Fig. 6). The focus of the study was mostly on bedding, fractures, or faults enhanced by differential erosion. Planar regressions were carried out for each point in the point cloud, enabling subsequent filtering and classification to be based on orientation, quality of fit, and relative locations of points.

Another work was performed in the Serra Geral Formation in Brazil by Souza et al., 2013, aiming to build a workflow on how to survey geological planar structure geometries using terrestrial scanner. In this project they used the IRLS 3D scanner, the same we use in this institute. The processing of the point cloud was executed by using three different methodologies, a comparison between them was made afterwards. After the results were compared with field data in order to determine their precision it, was concluded that they can give realistic characterizations of the orientation of planar geological settings.

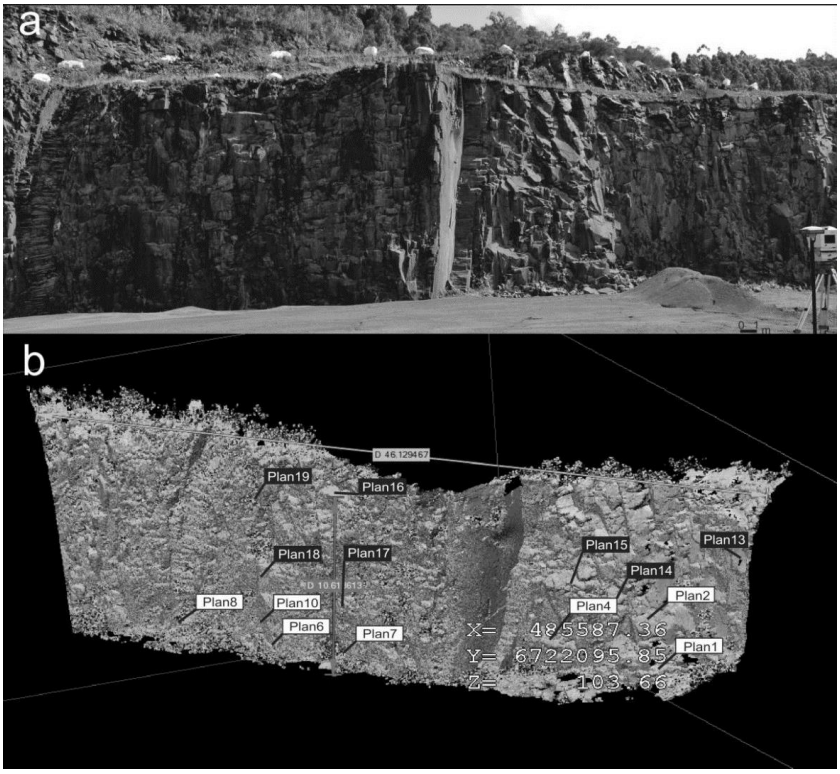

Figure 7. a) Picture of Study Area. b) Georeferenced Point Cloud. The IMInspect module of the Polyworks™ software was used to obtain measurements. The planes marked in white were measured by compass and clinometers, the orientations of which were computed with three techniques: 3P, MI, and PR. The planes marked in black were hard to access and were computed with three different techniques (Souza et al., 2013).

As far as Greece is concerned, Jones *et al*. (2009), performed a quantitative analysis in addition with visualization of the nonplanar surfaces of the Arkitsa fault, located on the southern side of the northern Gulf of Evia in central Greece. Quantitative analysis of the LIDAR data, combined with three- dimensional visualization software, allows the spatial variation in various geometrical properties across the fault surface to be clearly shown. Analysis using different curvature properties on fault surfaces, provided some the best plots for quantitative measurements of the corrugation and fault geometry. As the authors mention though, the results need further work to unravel the complexities found on the outcrop scale, and to relate the spatial variation in fault geometry to larger scale fault kinematics and dynamics.

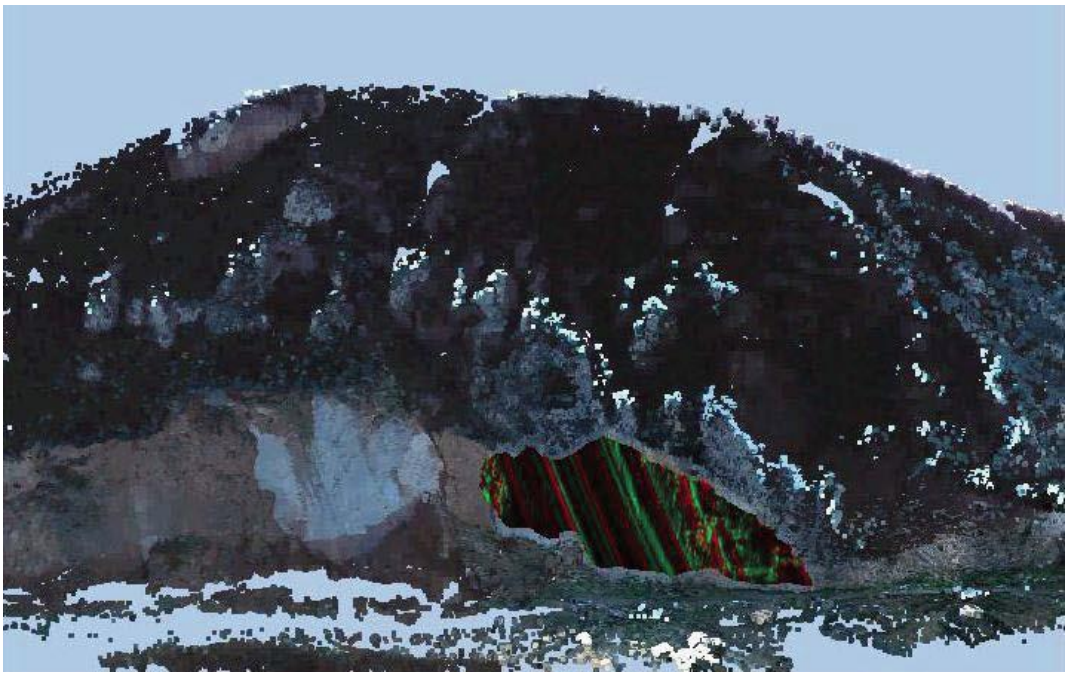

Figure 8. Enhanced virtual outcrop in which the results of curvature analysis for panel B are projected back onto the LIDAR (light detection and ranging) data. The colors highlight spatial variation in the magnitude of maximum normal curvature. (Jones et al., 2009).

2.3 Software used

In the framework of this master Thesis, in order to determine to which extend LIDAR data can be of use in geosciences, several software platforms were tested. Most notable for the results they produced, in our case, were Polyworks®, CloudCompare (open source), and

Global Mapper™. The data that was used was mainly high density point clouds of fault escarpments, fault surfaces, palaeoseismological trenches and fossilized tree trunks.

The first step was to format the raw data from IRLIS 3D with the ILRIS Parser software, version 5.0.3.1, in several different file formats, in order to be compatible with these software platforms. The Parser program processes raw scanner data in a variety of output formats recognized by Polyworks, various GIS software packages, and 3D modeling suites in general. It is designed to provide any information from the scan data loaded and helps the user to insert additional elements for the data along with corrections that he may need to do. Its applications consist, when possible, of geo-referencing, applying Pan/Tilt transform, color channel and intensity values, as well as atmospheric and slant range smoothing corrections.

To start with, Polyworks was the software with which the largest part of point cloud editing was made. Polyworks is a universal metrology software platform for laser scanning data by Innovmetric (www.innovmetric.com), aimed at processing high density point clouds coming from a wide variety digitizing and probing devices. Its prime functions are 3D metrology (3D measurement), data processing, reverse-engineering and inspection. Some of its most notable applications in 3D metrology are dimensional control of the data, statistical control and point cloud engineering. These functions render it extremely useful in 3D modeling in geology, as is not only able to create a virtual model of a geological structure but also gives the ability to perform various measurements and analyses that cannot be easily performed out in the field. In addition, it enables 3D models to be transferred into different formats and imported to different software platforms.

In this master Thesis, Polyworks 10.0 (32-bit) was used and, from the various modules it consists of, pifedit, IMAlign, IMMerge, IMEdit and IMInspect modules were tested. To begin with, pifedit is a module specialized for selecting and deleting points of a point cloud in order to remove the unnecessary parts. IMAlign is a 3D Image Alignment Software that is very effective in merging (or strapping) different image scans together, remove overlapping points and creating a single point cloud with the best data from each scan. This is where the user can interpolate, sample and bring the point clouds in the desired state, before they are aligned together using the semi-automatic “N Point Pair Alignment” tool. The next step is to

verify that the scans are properly aligned and to reduce the overlapping data. To mesh the aligned scans and create polygonal models the data has to be processed with IMMerge. This allows us to import them to IMMedit, where in turn model enhancement, editing, cross sections and curvature analysis are few of the functions available that can be apply into the polygonal models. Finally, IMInspect offers a number of metric measurements and comparison tools to the polygonal models and point clouds, its true use however is that it consumes less system resources, allowing to quickly inspect large sets of data. This is particularly useful when inspecting a data scan right after its acquisition in the field to check its integrity and if it is on target.

One major drawback of the version that we used for this Thesis, however, was that it is a 32-bit format version, meaning the functions of the program took a considerable amount of time as it can only use a maximum of 4GB RAM, a serious disadvantage when using high density point clouds. More recent versions of the same program are in 64-bit format and have no limitations on the amount of RAM they can use.

Cloud compare is an open source 3D point cloud and triangular mesh processing software (www.cloudcompare.org). The version used for this master Thesis is CloudCompare version 2.7.0 (64-bit). It provides a set of basic tools for aligning, merging, manual editing as well as rendering of 3D point clouds and triangular meshes. In addition, some examples of other features are advanced processing algorithms for projections, statistic computation, segmentation and estimation of geometric features. Although it has almost all the basic applications for point cloud editing and alignment, the most useful tools in our case were the statistical outlier filter that removes isolated points, the estimation of normals and curvature, planar facets detection and the qCanupo plug-in for point cloud classification.

After the scans were imported into the software, the first step was to remove the isolated points and compute the normals for the curvature and gradient analysis. The result of these two analyses can be selected in the scalar fields section, along with the intensity values (if they exist), greyscale and other analyses results. Afterwards, the planar facets detection and point cloud classification were tested giving promising results.

Finally, Global Mapper is a geographic information system (GIS) software platform capable of handling vector, raster, and elevation data. It emphasizes on terrain and 3D data

processing, watershed delineation, contour generation, volume measurement and raster calculation among many other tools. The LIDAR module allows it to process point cloud data, quite effectively in terms of terrain classification and generating high precision digital elevation models (DEM). For this Thesis Global Mapper version 16.1 (64-bit) (b021915) with the LIDAR add-on was used. After the point clouds were imported, the point classification was initiated, categorizing the points of the cloud into ground points, vegetation and buildings. This step is important as it allows the user, when creating a DEM from a data set, to ignore the non-ground points and create a better representation of the morphology of an area.

2.4 Methodology

2.4.1. Point Cloud Classification

Point clouds mostly intended for geomorphological analysis, such as coastal environments, cliffs, fault escarpments, often require data classification into elementary relevant classes. The basic idea is to classify surfaces according to their morphology, with a few examples being the separation of the vegetation or artificial structures from the ground and the distinction between fresh surfaces and rockfall in cliff environments. The goal of the classification procedure is to define the best combination of scales at which the dimensionality is measured and allows the data to be effectively separated in two or more categories. The biggest advantage of this method is that allows the researcher to identify and easily eliminate the unnecessary parts of a 3D model, keeping only the areas of interest and giving him a more accurate view of the target. Having an almost complete and precise documentation of natural surfaces has improved several new geologic applications, including the detailed analysis of the geometric properties of natural surfaces over scales ranging from a few centimeters to kilometers (Brodu and Lague, 2012) (Fig. 9). A great example of how point cloud classification can be a great asset is by Kondo et al. (2008). In this project, they created a DEM of an area in Matsumoto City where after the classification of the point data, they removed artificial structures and were able to study a fault escarpment that crossed the city (Fig.10).

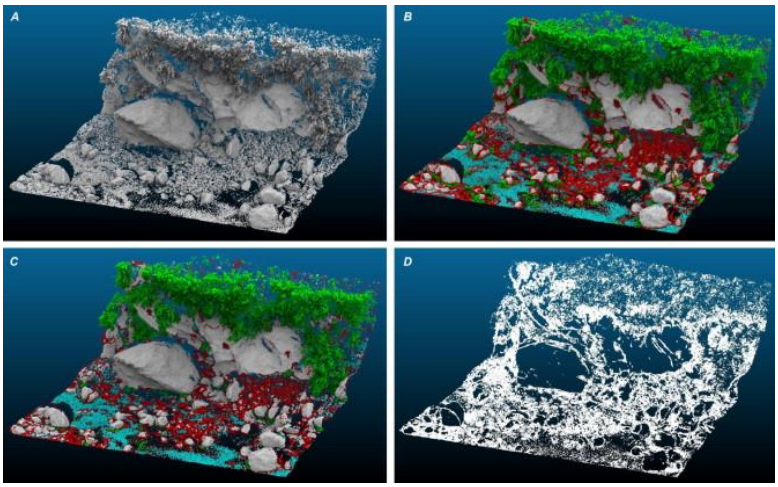

Figure 9. The four images show the result of the classification process that was done in the Otira river by *Brodu and Lague*, 2012. (A) Original Otira River scene. (B) Default classification (green: vegetation, grey: bedrock, red: gravel, blue: water). (C) User-improved classification. (D) Unlabeled points (28.2% of the total points).

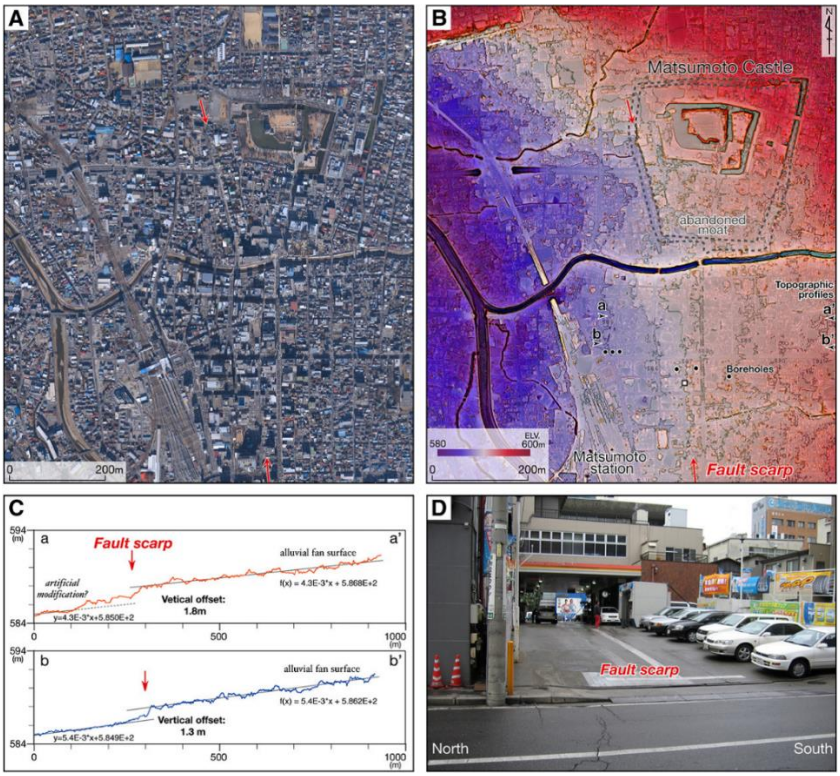

Figure 10. Results of the LIDAR survey done by Kondo et al.(2008) for the fault scarp in the urban district of Matsumoto City. (A) Orthophotograph of the urban district in Matsumoto City during the time of the LIDAR survey. (B) Red relief map with colored elevation layer derived from the 0.5-m DEM. Thin lines denote contour lines with interval of 1.0m. The northern and southern ends of the fault scarp is shown by the two red arrows. (C) Topographic profiles across the fault scarp. Vertical separation on the fan surface, represented by thin reference lines of linear segmented regression, is clearly expressed. The reference lines are determined by the least square method to minimize the sum of the squared residuals. (D) Photograph in the field from the heavily built-up survey area. The location is shown in (B) as a white rectangle.

2.4.2. Morphological Analysis and Morphotectonic Parameters

Morphotectonic analysis constitutes a powerful tool for detecting and understanding the processes that occur on the earth's surface. They are useful for acquiring quantitative information of the morphological features of an area and their calculation is based on geomorphologic measurements. They help us understand the effect a fault has in the geomorphology and are the key to associate the landscape with fault growth and the neotectonic evolution of the region under research (Chatzipetros *et al*., 2005; Sboras *et al*., 2010).

The type of rocks that a fault escarpment is consisted of, plays an important role in the way the process of erosion affects the morphology of the slope and thus must be considered first when computing morphotectonic parameters. Basement rock escarpments usually have higher slope angle than those of the basin sediments even though in most cases are older. Some additional factors that affect the process of erosion are the amount of sun that a slope is exposed during the day (as it can create higher differences in rock temperature during the day and night), the vegetation cover and the impact of human activity in the area (Chatzipetros, 1998).

For the best possible and accurate results, the estimation of morphometric parameters (geomorphic indices) requires a high-resolution digital elevation model (DEM) (Tsodoulos *et al*., 2008). Dense point clouds are ideal for creating these high-resolution DEMs, as they can have a grid resolution of centimeter scale, thus being the easiest and most effective way to generate them. Nevertheless, even though morphotectonic analysis is a good indicator, it is not a stand-alone proof and it is best used in combination with other types of geological analyses.

2.4.3. Normal Computation

In geometry, a normal is a line or vector that is perpendicular to a given plane. From the three-dimensional perspective, a surface normal to a surface at a specific point is a vector that is perpendicular to the tangent plane to that surface at that point. The normal vector is

often used in computer graphics to determine a surface's orientation toward a light source for flat shading, or the orientation of each of the corners (vertices).

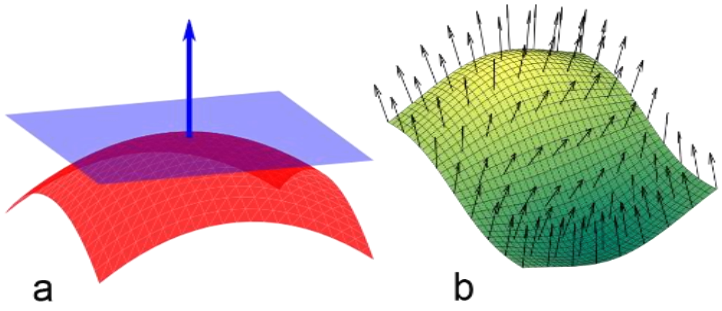

Figure 11. a) A normal to a surface point is the same as a normal to the surface's point tangent plane. b) A vector field of normals to a surface. (Modified from wiki commons Nicoguaro, 2016)

Polyworks generates them during the triangulation process of the point cloud to a polygonal model whereas CloudCompare uses a variety of methods and algorithms. In CloudCompare the most efficient normal computation methods were the Quadric and the Plane (with normal inversion). The name of the methods respond to the way the algorithm uses approximations to infer the surface normals from the point cloud dataset directly.

2.4.4. Curvature Analysis

The curvature of a surface is a measure of the divergence it has from planarity. Some examples that curvature can be expressed are normal, Gaussian, and mean. In mathematical terms, curvature is a second-order derivative of the surface, and for that reason curvature values are independent of the surface's orientation. Curvature analysis of geological surfaces can provide useful plots for quantitative measurements of folds and fault geometry, such as corrugations and has also been employed to describe the geometry of strata, to quantify the degree of deformation or strain in deformed strata, and to predict fracture orientation (Bergbauer and Pollard, 2003; Jones *et al.*, 2009).

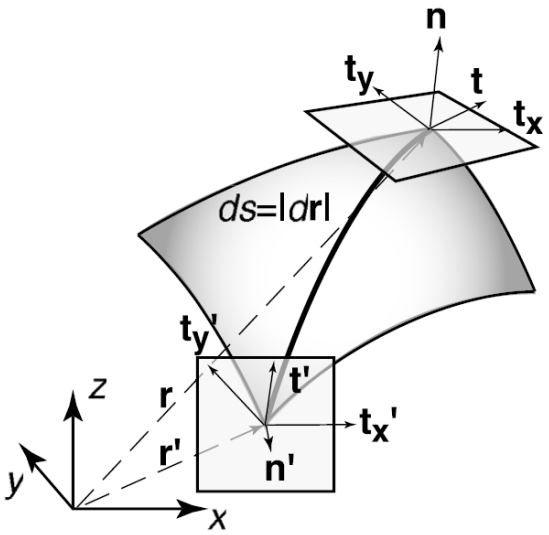

Figure 12. The curvature of an arbitrary surface is defined as the rate of change of tangent vector t as one moves along the arc of a curve ds on the surface (thick curved line). The normal vector n is defined by the position vector r. t_y and t_x are tangent vectors that define tangent plane at this point *(Bergbauer and Pollard, 2003)*.

Gaussian Curvature is the product of the two principal curvatures that exist in a point of a surface ($K = \kappa_1 \times \kappa_2$). The curve from the intersection of a plane containing a normal vector and the surface is called normal section. In most points on most surfaces, different normal sections will have different curvatures; the maximum and minimum values of these are called principal curvatures, named κ_1 and κ_2 respectively. (https://en.wikipedia.org/wiki/Gaussian_curvature). However, because curvature analysis is highly scale-dependent, it requires careful filtering and smoothing of the data to be able to analyze structures at different wavelengths *(*Jones *et al*., 2009).

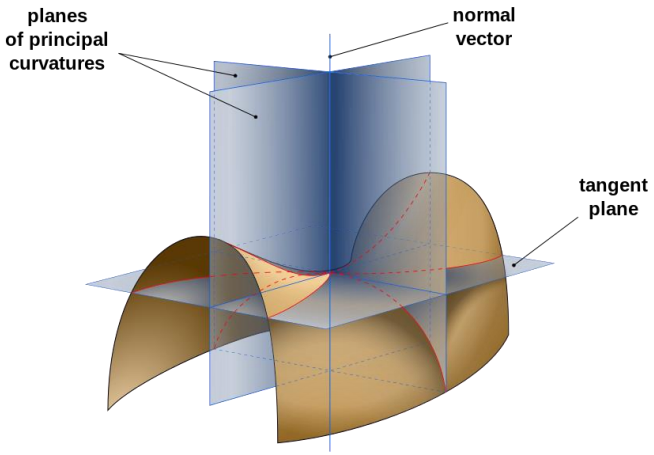

Figure 13. Saddle surface with normal planes in directions of principal curvatures. (Patrick87, Public Domain, https://commons.wikimedia.org/w/index.php?curid=22612216)

The computation of curvature is based on the surface normals, which depending on the program used, are either automatically generated by it, or generated by the user using a certain method. Because the process in Polyworks is based on the triangulation grid of the polygonal model, when the model is imported in IMEdit, it is easy and fast to generate the curvature of the plane. IMEdit offers a variety of curvature options that can be used for the fault surface, such as Mean, Gaussian, Maximum/Minimum Curvature and more. In CloudCompare there is the option to generate the Mean and Gaussian curvature of an object by best fitting a quadric around each point. Moreover, the user is allowed to choose certain elements of the computation process and thus giving the freedom to customize her depending on the situation (http://www.cloudcompare.org/doc/wiki/index.php5?title=Curvature).

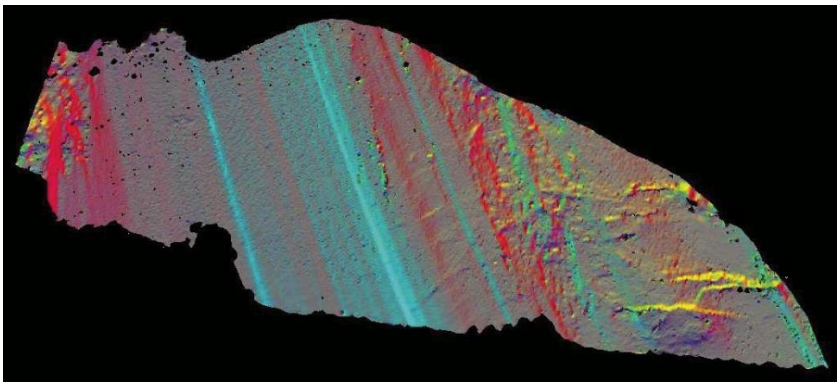

Figure 14. The Arkitsa fault plane mesh, with each triangle allocated with color according to the relative orientation of its normal vector compared with the orientation of the mean vector for the entire fault panel. This visualization method helps to highlight the curvature and corrugations at different wavelengths, as well as the effect of crosscutting fractures. (Jones et al., 2009)

2.4.5. Surface Roughness

The surface roughness estimation for each point represent the value of distance between this point and the best fitting plane computed on its nearest neighbors. The radius that CloudCompare uses to compute the roughness of the surface can be determined by the user. When there are not enough neighbors to compute a plane, it will appear in grey (http://www.cloudcompare.org/doc/wiki/index.php?title=Roughness). This analysis can provide useful information when trying to identify possible changes of the properties or irregularities of a geological surface.

2.4.6. Planar Facets Analysis

In CloudCompare there is also the FACETS plug-in capable of performing geological planar facets analysis which automatically extract planar facets from point clouds (e.g. fracture planes). The analysis is based on the normals of the surface it runs on, and creates domains of planar facets. The program first recursively divides the point cloud into sub-cells and then computes elementary planar patches and then regroups them progressively according to a planarity threshold into larger polygons (bigger 'facets') (Dewez *et al.*, 2016). During this process, it calculates their dip and dip direction (i.e. azimuth of steepest decent) and classifies them based on their orientation and their orthogonal distance. The data, after the conclusion of the process, can be reported in interactive stereograms and can be exported as a shape file (.shp) to a GIS software platform. This feature (or plugin) can be very helpful in defining the changes of dip and dip direction throughout a surface, a key feature to unravel the tectonic history of a rock outcrop as well as, in some cases, to help estimate the stability of a rock cliff. In the case of fault planes it can be an indicator of fault corrugations, and depending on the scale of its use, it can provide with information about the fault's dip and dip direction along its length.

The fault plane corrugation characteristics are an important factor when studying a particular fault or fault system. They are believed to form from overlapping faults by two main mechanisms, the lateral propagation of curved fault tips and linkage by connecting faults. Large-scale corrugations may have their origins in the progressive breakthrough of originally segmented fault systems *(*Jones *et al*., 2009).

3. Regional Setting and Methodology

3.1. Heraklion Basin – Stavrakia Fault

3.1.1. Regional Setting

Stavrakia fault is located in the wider area of 'The Heraklion basin', which is the largest of several multi-oriented tectonic basins on the island of Crete, southern Greece. Crete is

located at the fore-arc of the Hellenic Subduction Zone, which is the result of the subduction of the African under the Eurasian plate, close to the shallow portion of the seismically active region of convergence. Due to its position Crete is considered as one of the most seismically active areas in the eastern Mediterranean displaying the effects of intense Late Quaternary tectonic deformation mainly represented by significant regional uplift and normal faulting, defining it as an area of important and high seismic activity (Caputo et al., 2010; Ganas et al., 2010) Crete displays an extensional deformation system along both the arc-parallel, high-angle, E-W striking faults and the arc-normal, high-angle pure-normal and obliquenormal N-S striking faults (Fassoulas, 2001).There are also sets of normal faults striking NW-SE and NE-SW (Ganas *et al*., 2010).

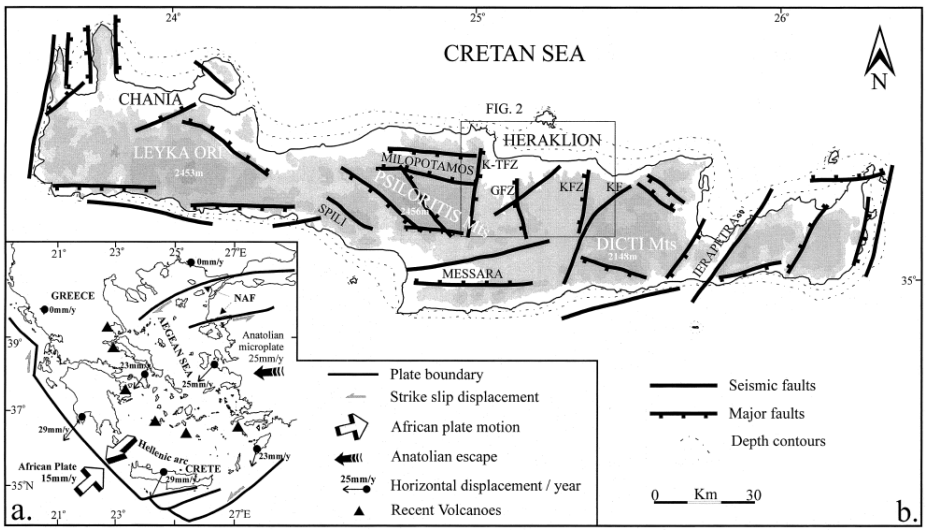

Figure 15. The present tectonic situation in the Aegean region. Displacement rates are presented in respect to stable Europe. NAF, the North Anatolian Fault. (b) The major fault zones and geomorphological features of Crete. K± TFZ, the Kroussonas±Tilissos fault zone; GFZ, the Giouchtas fault zone; KFZ, the Kasteli fault zone and KF the Kasteli fault. Altitude shading represents heights of 200, 600, 1000, and 2000 m, while the depth contour lines are of 100 and 200 m. The square shows the north part of the Heraklion Basin (Fassoulas, 2001).

Heraklion basin is located within the graben formed by the NNE–SSW Malevizi and Kasteli kilometer-scale fault zones between Ida and Dikti mountains respectively, in central Crete (Delibasis *et al*., 1999; Fassoulas, 2001). The basin comprises an almost flat area with the exception of some hilly areas, with steep slopes (>30°) related to the N-S, NNE-SSW and NNW-SSE oriented faulting, and a maximum elevation at 296m (Kokinou *et al.*, 2013).

The Heraklion basin is mainly filled by fluvial - marine Neogene - Quaternary sedimentary deposits, uncomformably overlying basement rocks comprised mostly of Gabrovo - Tripolis and Olonos – Pindos geotectonic zones. The basement formations contain mostly dolomites and limestones of Upper Triassic-Upper Jurassic and Cretaceous – Middle Eocene age (Fassoulas, 2001; Kokinou *et al*., 2013, IGME 1993/1994).

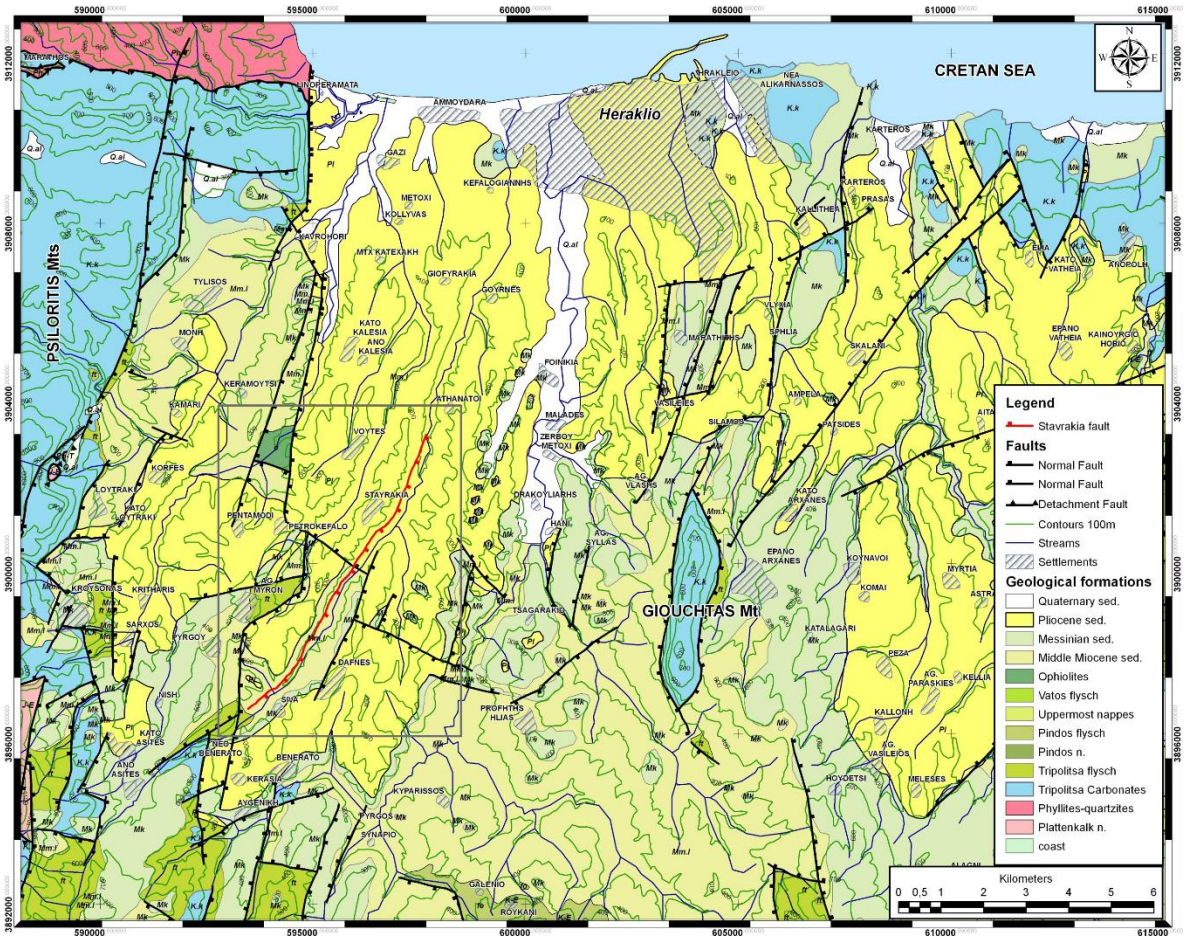

Figure 16. Geological map of the broader Siva-Stavrakia region with known faults based on geological IGME maps (scale 1:50000) and EMERIC II. The square shows the study area and within the Stavrakia fault, studied in this Thesis (Fassoulas et al., 2010)

The oldest formation is the Triassic–Upper Jurassic limestones, dolomitic limestones and dolomites. They constitute the base of the external zones tectonic nappe, resulting in a local mylonitization at their base due to tectonism (Kokinou *et al*., 2013). Mesozoic to Eocene limestones are detected in the margins of the basin and as isolated bodies within the basin (e.g. Giouchtas horst), whereas, Eocene flysch sediments are present at its northeastern

margins (Fassoulas, 2001). The Cretaceous–Middle Eocene limestones are grey to black, medium-thick bedded to massive bituminous locally microbrecciated and dolomitic in the upper members (Kokinou et al., 2013).

The Neogene is represented by Pleistocene marine bioclastic limestones, sandstones with cross-bedded conglomerates and marls, white marls or marly limestones, greyish clays with brown, often thin bedded intercalations, white-beige fossiliferous marls, laminated marls or diatomites and bioclastic limestones. The base of this formation consists in general of an unsorted "marly breccia". It overlies unconformably the Upper Miocene formation, consisting of bioclastic, reef limestones, marls or marly limestones and gypsum *(*Kokinou *et al*., 2013). The Quaternary sediments mainly comprise fluvial and closed basin deposits and undivided marine terraces and coastal sands (Kokinou *et al*., 2013). The Neogene and Quaternary sediments have a varying thickness, around 400 m at the western margin, 200 m west of Giouchtas mountains and 800 m south of Heraklion town (Fassoulas, 2001). The Neogene sediments are intensely fragmented having a general dip to the north, while the Pliocene sediments do not present a uniform dip direction.

The Heraklion basin is fragmented by numerous normal faults that can be separated in three distinctive fault groups. The first one comprises the E-W trending faults that expose a normal, dip slip component and mainly cut the basement rocks. Some of these faults are kilometer-scale, running over the northern and southern flanks of Psiloritis Mountains. The second group consists of large -to moderate- scale N-S trending faults that clearly postdate the earlier E-W trending structures. In most cases these faults indicate a pure dip slip or a slight lateral component of shear. Three major fault zones are included in this group, the Kroussonas-Tilissos, the Giouchtas and the Kasteli zones. The third group appear to be the youngest faults occurring in the Heraklion basin. These are normal faults trending NE-SW and NW-SE with a small component of lateral displacement.

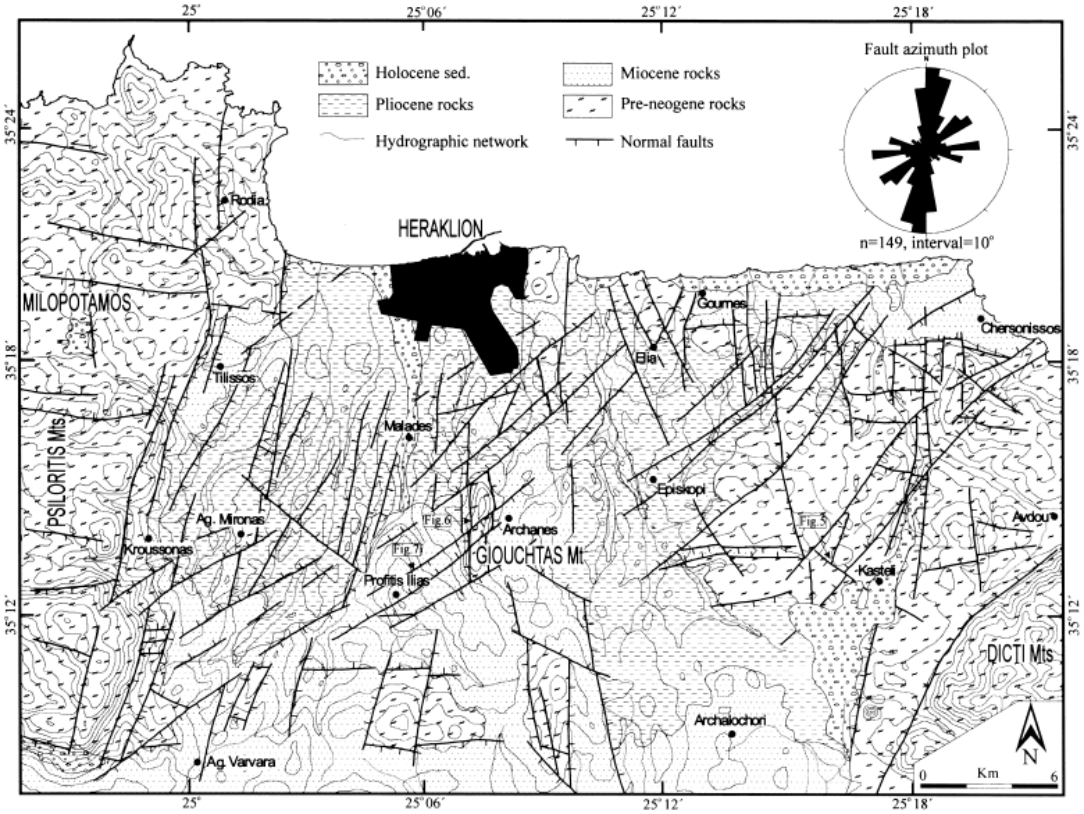

Figure 17. Geological map of the Heraklion basin. Rose-diagram depicts the fault azimuths. Altitude contour lines every 100 m (Fassoulas, 2001).

The fault scarp studied in this Thesis is located along the Heraklion – Mires road adjacent to Stavrakia (in the South) and Siva villages (in the North), forming the western slope of an elongated valley. The fault has a NNE – SSW trend and dips to the SE at 70° *(*Fassoulas *et al*., 2010). Its apparent length is about 7.5 km fading out northwards in the river valley, whereas it is geologically unclear if it continues further to the south. In few places flat surfaces can be found with microstructures which indicate a normal sense of movement under an E – W extensional regime, whereas a minimum vertical slip of about 30m can be determined. The fault scarp is developed mainly in Tortonian marly, conglomerate and sand intercalations of the Ampelouzos Formation to the South and in Pliocene white and light grey marls of the Finikia Formation to the North. Apart from the Ampelouzos Formation to the South, there are outcrops of two other Formations, the Agia Varvara and Viannos ones, consisting of Tortonian conglomerates, brecciated limestones, marls and middle Miocene clays.

3.1.2. Methodology

3.1.2.1. Data Acquisition

A detailed survey of the fault scarp was carried out in late May 2015 using terrestrial laser scanning (TLS). The equipment used at the Stavrakia Fault site was ILRIS-(3D-HD) laser scanner which is a long range scanner with an effective range of more than 1000m under favorable conditions. The range of the scanner was essential in order to capture the morphology of the entire slope. The fault zone was scanned using the standard acquisition strategy of taking multiple overlapping scans from a number of different tripod positions (scan stations) along the length of the fault.

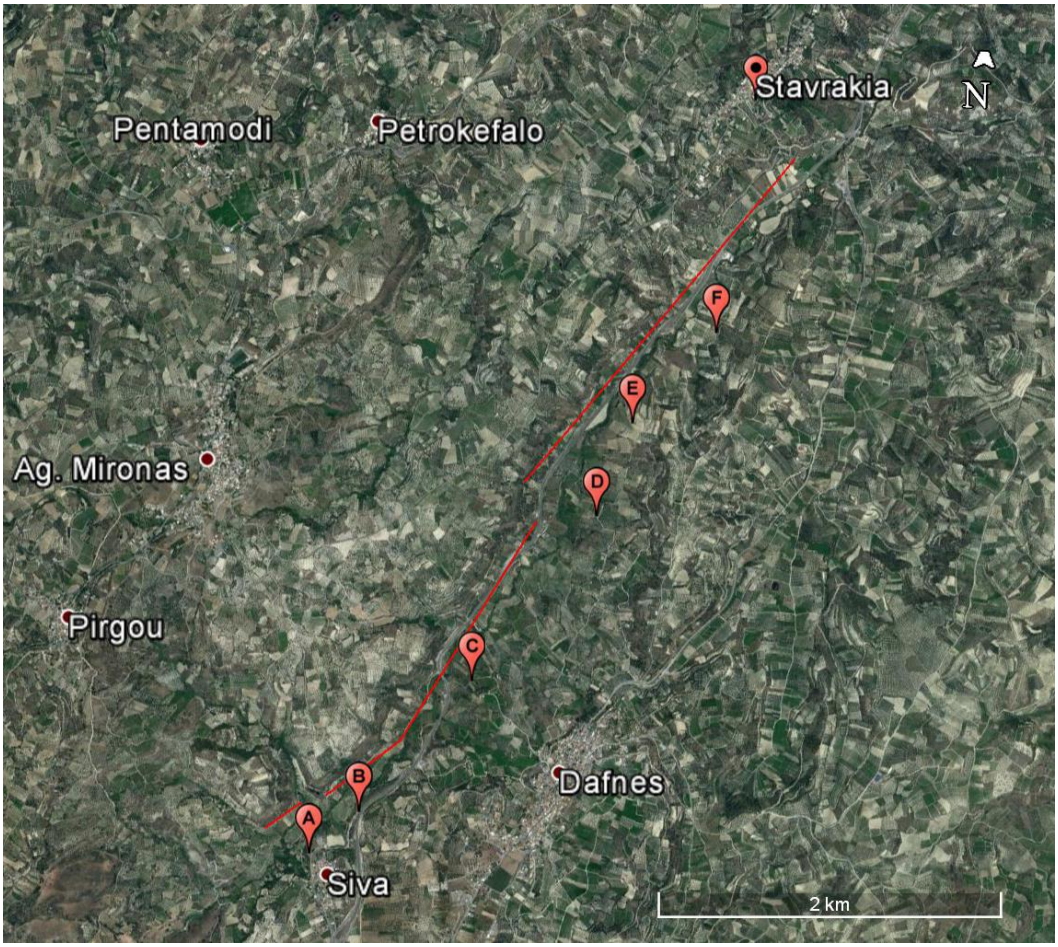

Figure 18. The scanning stations for the Stavrakia fault escarpment. The red lines represent the face of the fault that was surveyed. From A-F are the areas used for scanning stations in their respective order.

This aims to minimize any large gaps in the data (data shadows) caused by the irregular topography of the slope surface. In practice, there will always be some data shadows, but careful planning of the data acquisition can help keeping them to a minimum when possible. In this study 6 scan stations were established along the fault scarp from an average perpendicular distance of 351m. Over a period of 2 days, 37 scans with a total of 102,459,115 (one hundred million) points were acquired from these stations.

Figure 19. The three segments of the fault scarp close to Siva vilage in panoramic view. The pictures were taken by IRLS 3D from the scanning stations, with the upper picture being the southermost part of the scarp and the bottom one the northenmost.

Figure 20. The three segments of the fault scarp close to Stavrakia vilage in panoramic view. The pictures were taken by IRLS 3D from the scanning stations, with the upper picture being the southernmost part of the scarp and the bottom one the northenmost.

3.1.2.2. Data Processing

The main purpose of this study is to acquire quantitative information about the slope geometry of the fault scarp and create an accurate virtual representation of the slope. The virtual copy of the slope will then be used for morphotectonic analysis in order to draw some conclusions about the characteristics of the fault scarp.

The creation of the virtual representation of the fault scarp was made possible with the use of Polyworks, and more specifically with the pifedit and IMAlign modules. Each scan had its unnecessary parts removed and then was filtered down to a manageable amount of data points, ready for computational processing. The next step was to stich the scans together in IMAlign with the use of manual and semi-automatic processes to minimize the error

involved in matching scan stations to each other. This was done with the “N point pair alignment” tool, where the user manually selects 3 common points or small areas in two overlapping scans and then with the use of an algorithm, the program stitches them together. For this project the mean average error in the overlap of the scans was 3 mm +/-0.045mm which is acceptable in the current situation. This process resulted in the data to be rendered as a virtual fault scarp that can either cover the entire area or be presented as more localized parts of the slope. The slope was divided in three individual sections as to avoid software lagging and slow processing due to the huge amount of data. The three scans, Siva 1-2, Siva 3 and Stavrakia were subsampled at 14 million points in total. At this stage the data is still in the form of point cloud, as this is usually adequate to give a good impression of the nature of the outcrop prior to further processing if necessary.

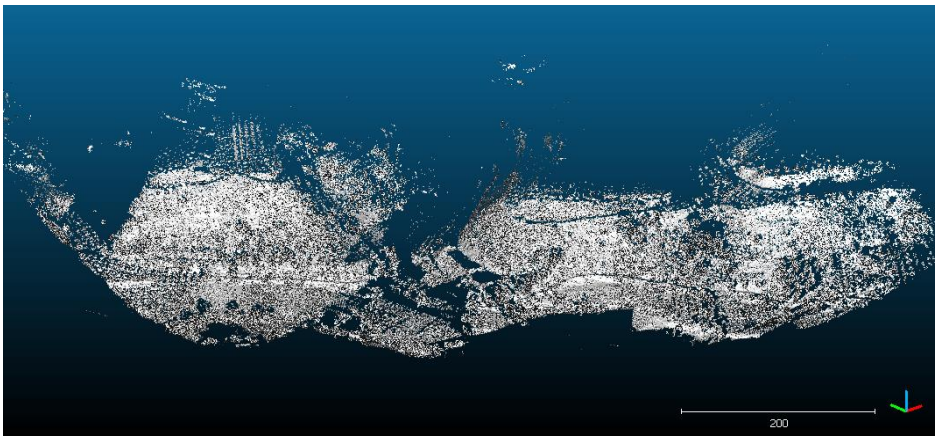

Figure 21. Siva 1-2 point cloud, result of the first two scan stations of the Stavrakia fault escarpment near Siva village.

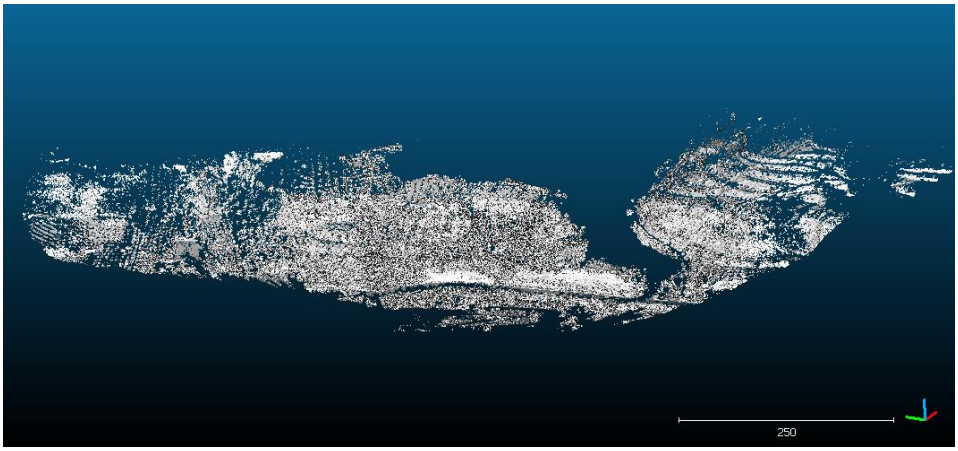

Figure 22. Siva 3 point cloud, result of the third scan station of the Stavrakia fault escarpment close to Siva village.

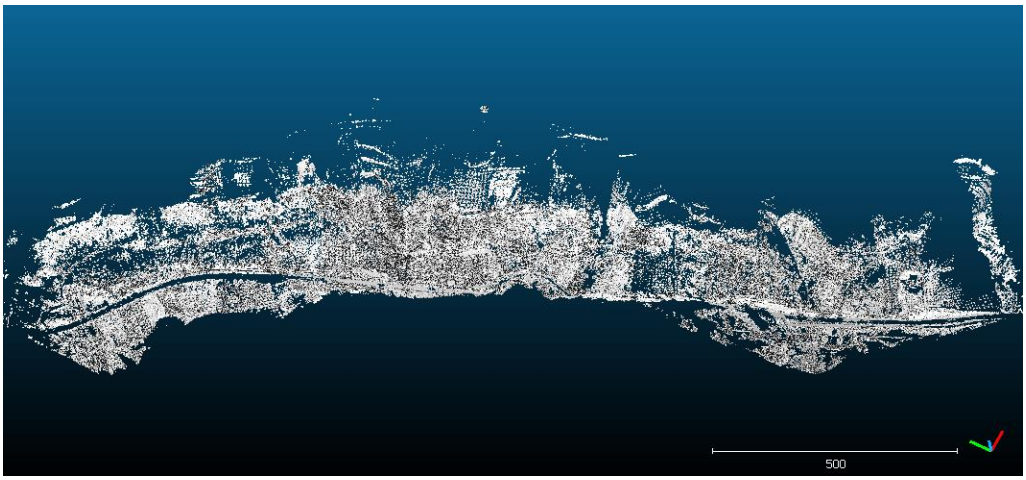

Figure 23. Stavrakia point cloud, result of the last three scans of the Stavrakia fault escarpment near Stavrakia village

To calculate the geometry of the slope, first a D.E.M. (Digital Elevation Model) had to be created from each part of the slope that was stitched together. This is important for the application of morphotectonic indices as it can provide information about variations in height and general morphology of the scarp along its extent. Each of the four sections was imported in Global Mapper as a separate scan, and was processed individually in order to create three precise DEMs using all the available points. ArcGIS was also considered, but it was unable to cope with the large amount of the point cloud data (14.million points), making it impossible to process them.

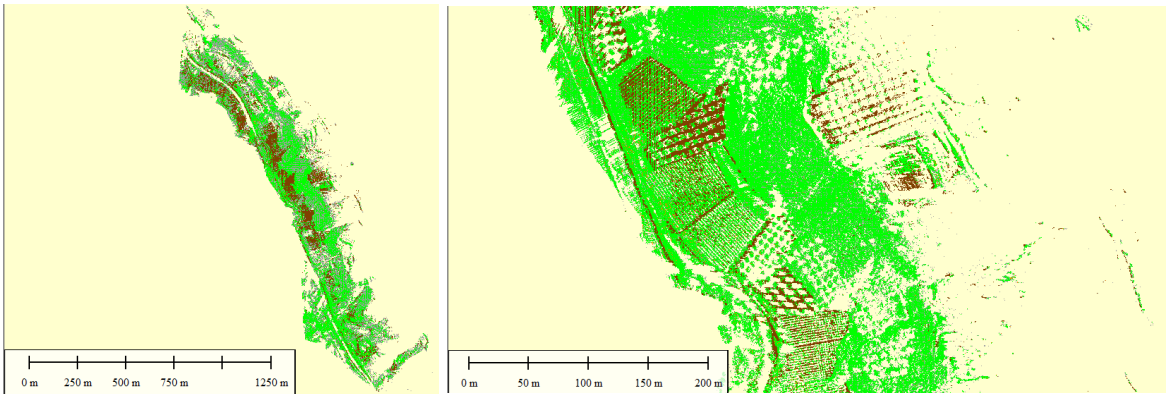

Figure 24. The Stavrakia point cloud as resulted from the ground and vegetation points' classification in Global Mapper. Even though it's not yet 100% accurate, it can still give a good impression of how the vegetation is distributed across the scarp and if it is beneficial for these points to be removed for any future analysis.

Before generating the D.E.M. the points of the cloud were classified either as ground or vegetation points using the "Auto-classify Ground and Non-Ground points" tools. Only

the ones classified as ground points were used for the D.E.M. in order to create a more precise representation of the slope morphology, ignoring the other points representing vegetation or artificial structures.

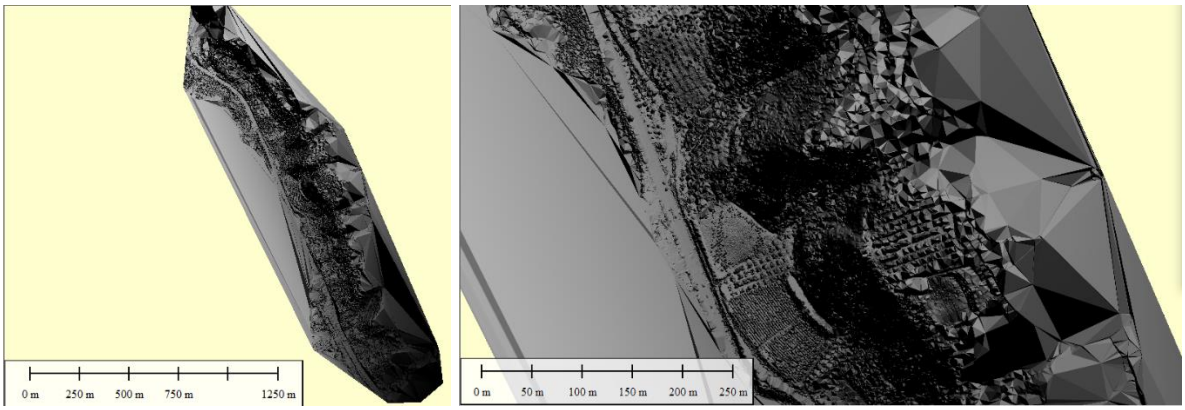

Figure 25. The Digital Elevation Model generated from the Stavrakia point cloud.

After the D.E.M. was created, in order to apply the morphotectonic indices, 93 cross-sections (for position see Fig. 29-31) were created along the slope, perpendicular to the fault scarp, with a fixed distance between them. The cross-sections were then imported from Global Mapper to Microsoft Excel as a XZ file and each cross-section was analyzed and subdivided in accordance to the angle along different parts of the slope. This way for different heights of each part (dy), a corresponding slope angle (φ) was calculated based on the horizontal distance between the lower and the upper part of each measured segment. The next step was to plot the heights (of the cross-sections that were taken perpendicular to the fault escarpment facets) versus the corresponding angle together in a semi-logarithmic scatter diagram in order for the correlation between the height and the angle to become visible. This method is based both on Bucknam and Anderson (1979) and Chatzipetros (1998), as they showed that there is a quantitative logarithmic correlation between the fault escarpment's total height (H) with its slope angle (θ). The equation that is used in this Thesis is in the form of:

$$\theta = m * \log(dy) + b \quad (1)$$

with m and c being constants. The trendline of the equation in a logH- θ scatter diagram is a straight line. The equation has been used in many areas around the world for geological

models based on the erosion of fault escarpments in different environmental conditions. The m value represents the gradient of the equation and b the intercept.

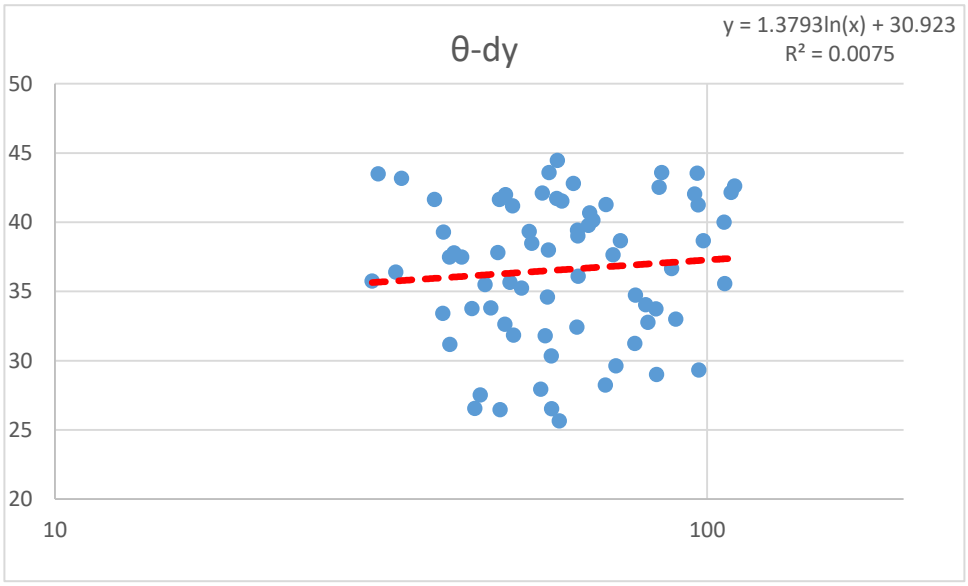

Figure 26. Scatter diagram of the total escarpment height (dy in X axis) with the slope angle (θ in Y axis). The equation as generated from Microsoft excel needs editing in order to be interpreted. The coefficient of determination (R^2) was also calculated.

The equation of the trendline generated from Fig. 26 needs to be adjusted to the format that was mentioned above. First the "ln" needs to be converted to "log" variable by:

$$\ln(x) = \ln(10) * \log(x) = 2.3 * \log(x) \quad (2)$$

This way the equation becomes:

$$\theta = 7.387 * \log(dy) + 22.757 \quad (3)$$

The coefficient of determination (R^2) is the percentage of the response variable variation that is explained by a linear model. It is well established in classical regression analysis and its values range from 0 to 1. In Fig. 26 is shown that the escarpment is quite uniform in its height variation, but displays a large range of mean slope angles even though indicating a small increase in slope angles with scarp height. The R^2 value displays a small confidence in the current situation as the fault's mean slope angle is quite uniform across the escarpment regardless its height most of the times.

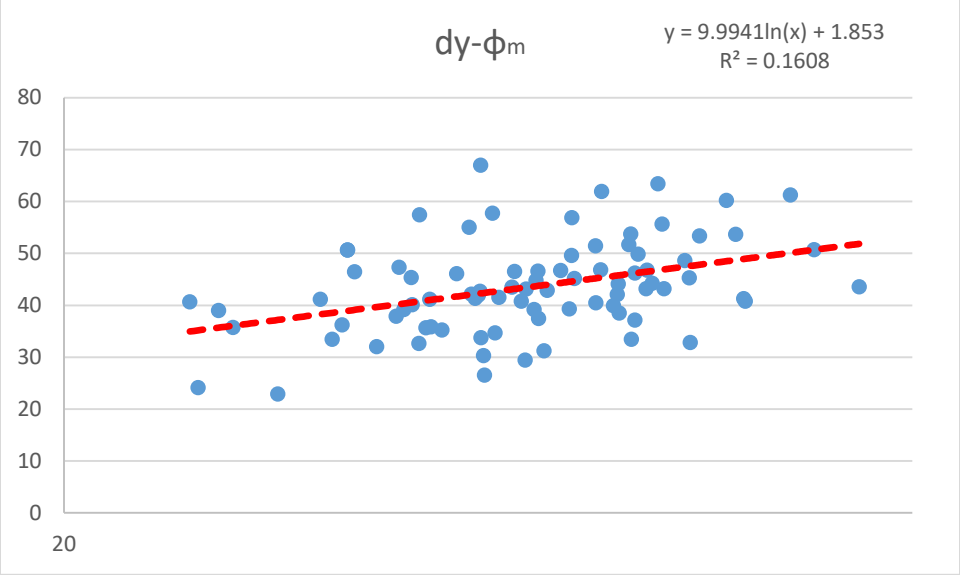

Figure 27. Scatter diagram of the total escarpment height (dy in X axis) with the slope max angle (φ_m in Y axis). R^2 shows a better confidence than in Fig. 26 and the result shows a more linear correlation between escarpment height and slope angle.

In Fig.27 the maximum slope angle was plotted with the total escarpment height, in order to find out the connection between those two in this area. The trendline equation becomes:

$$\varphi = 22.986 * \log(dy) + 1.853 \quad (4)$$

The R^2 in Fig. 27 shows a great improvement in confidence than in Fig.26, and the results indicate a stronger connection of the total escarpment with the maximum slope angle than with the average. A possible reason is the fact that because the escarpment is used for agricultural activities, many parts of the slope have been shaped from the constant human activity, leaving only the steeper edges mostly unaffected.

In addition the slope was divided in different parts depending on the slope angle and the total height of the particular part was calculated. A semi-logarithmic diagram was created (log(dy)-θ) in order to define the relationship of the height of each slope part with its composite angle degrees.

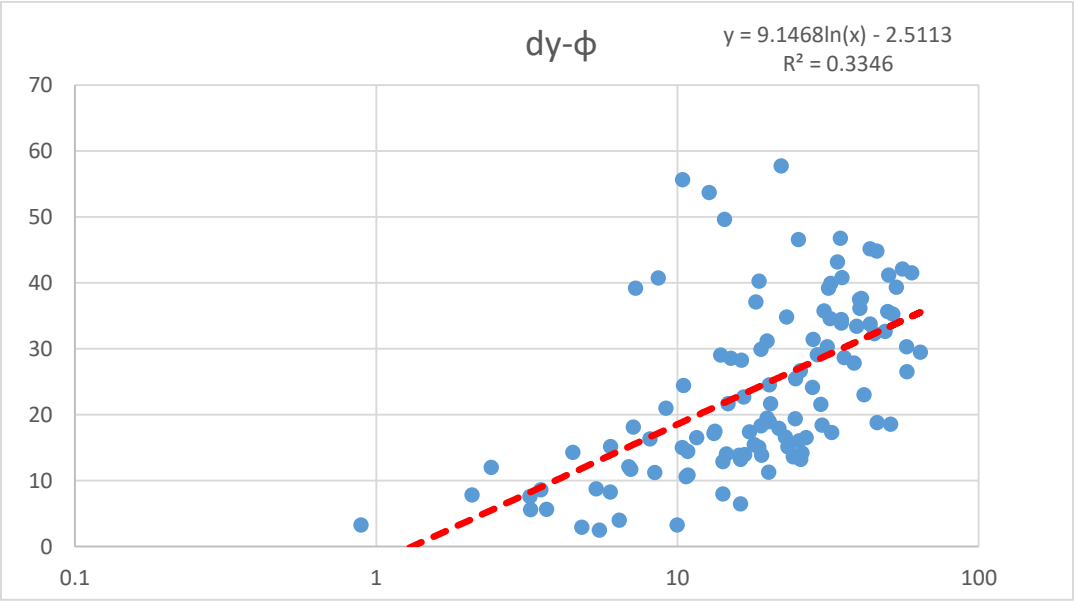

Figure 28. Scatter diagram of different heights of each part (dy) of the slope (in the X axis) with their composite angle (φ) (in the Y axis). The diagram shows that there is an almost linear correlation between the changes of the slope's angle with the corresponding total height.

Same as the previous diagram, the Fig. 27 equation changes to:

$$\varphi = 21.06 * \log(dy) + 2.5113 \quad (5)$$

In this case, the relation of slope angle and the composite height displays a clear linear relation with higher angles representing the most part of the escarpment's slope. This can be very useful in determining the age of the escarpment as well as the fault's activity. In fault escarpments, slope angles greater than 55° represent the free face and angles between 34° and 37° represent the stable-debris slope. The angles between these two sets represent the usually unstable transitional slopes (Wallace, 1977). As it is shown in all diagrams (Fig. 26-27-28), the largest part of the slope across the escarpment has angles greater than 30°, meaning the stable-debris slope. However, a large number of areas with angles higher than 40° is also present indicating unstable transitional slopes all across the escarpment.

In conclusion, from the scatter diagrams, it can be deducted that the fault escarpment displays a predominant slope angle of 35°- 40° (average at 36.8° and maximum angle average at 43.5°) for a height that ranges from 50m-100m (average 63.33m). The escarpment is comprised of Neogene carbonate sediments and thus easily affected by erosion, fact that explains the stable-debris slope categorization for most of its part.

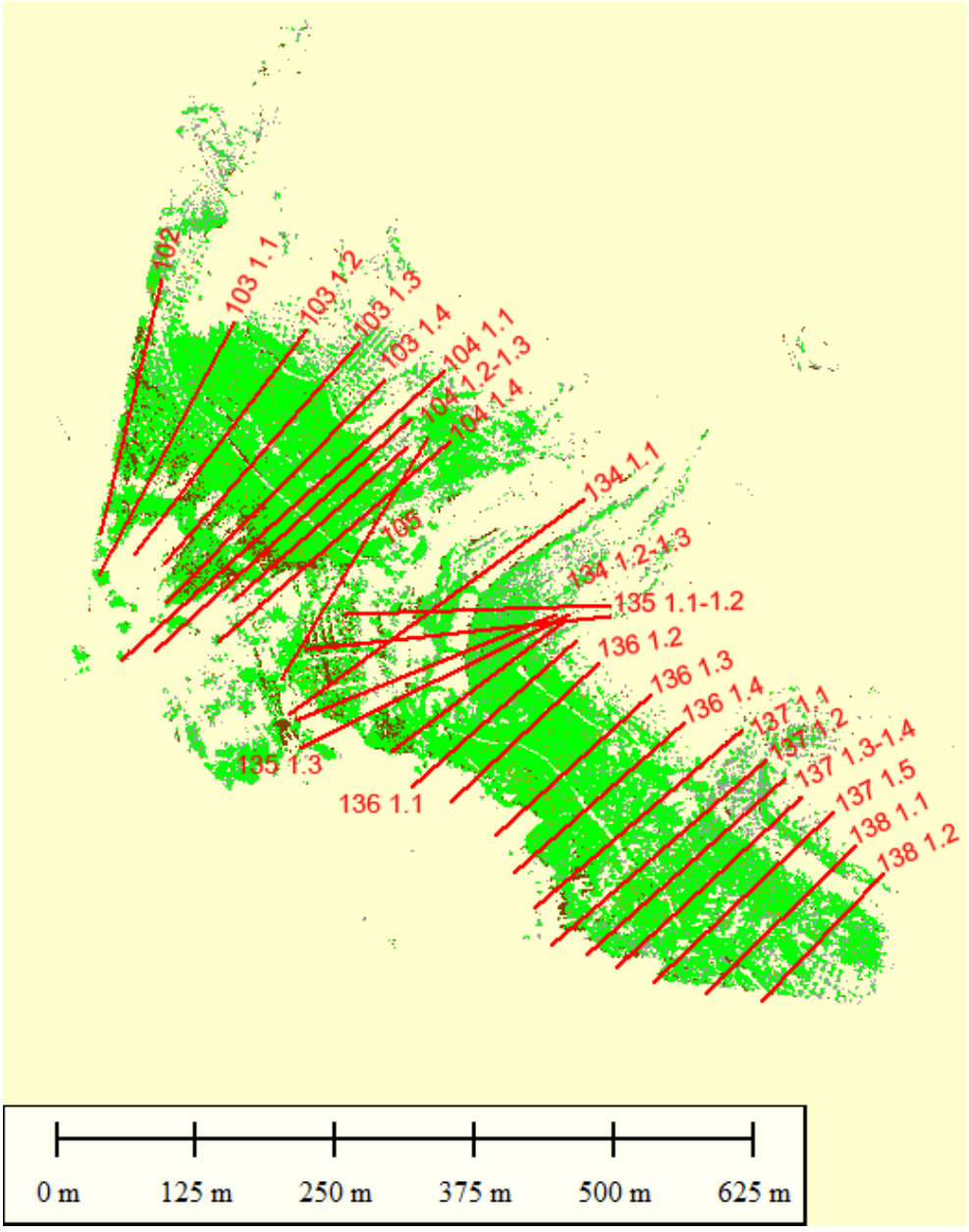

Figure 29. The position of the cross sections on the Siva 1b-2 fault escarpment point cloud in Global Mapper.

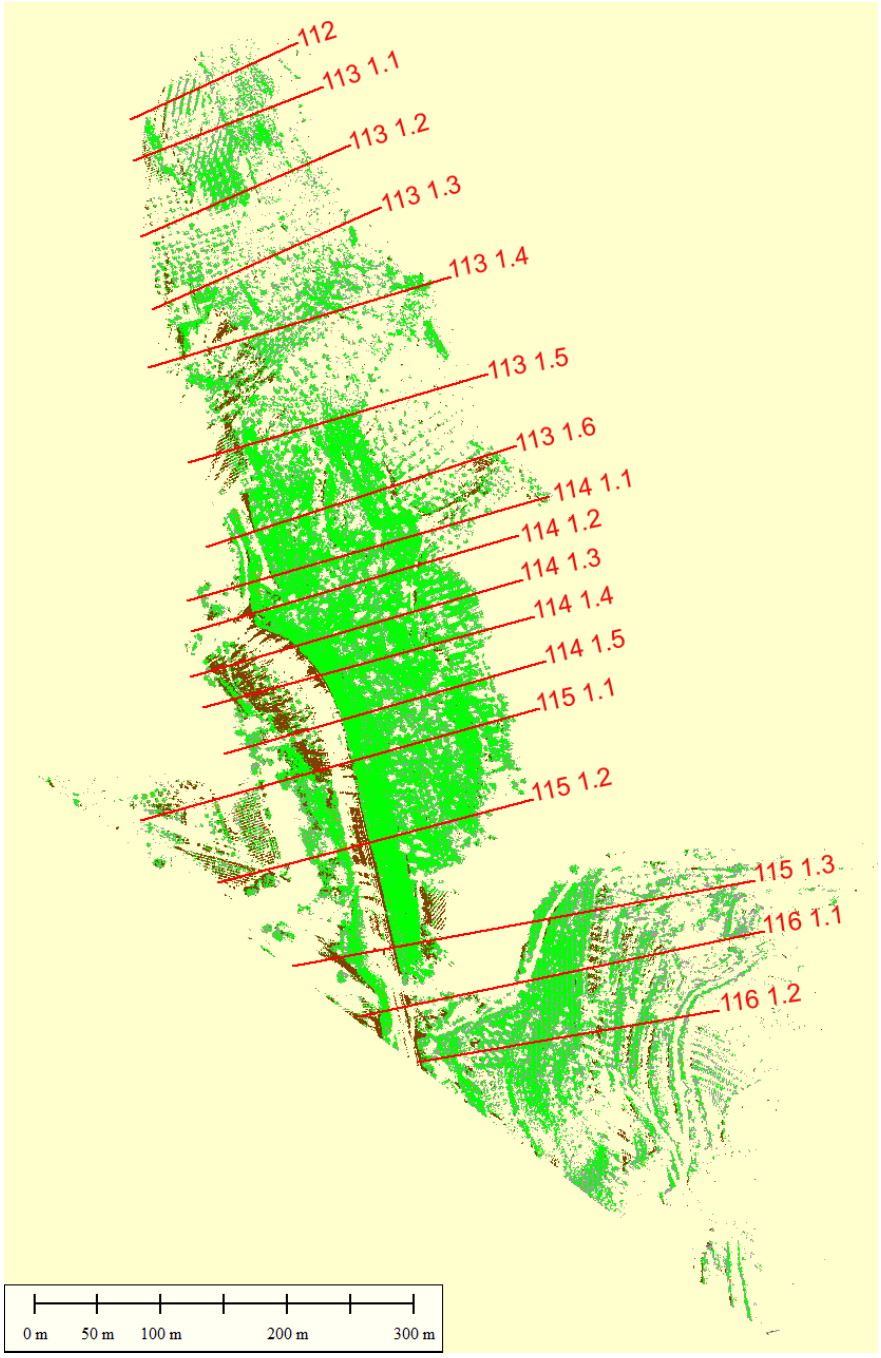

Figure 30. The position of the cross sections on the Siva 3 fault escarpment point cloud in Global Mapper.

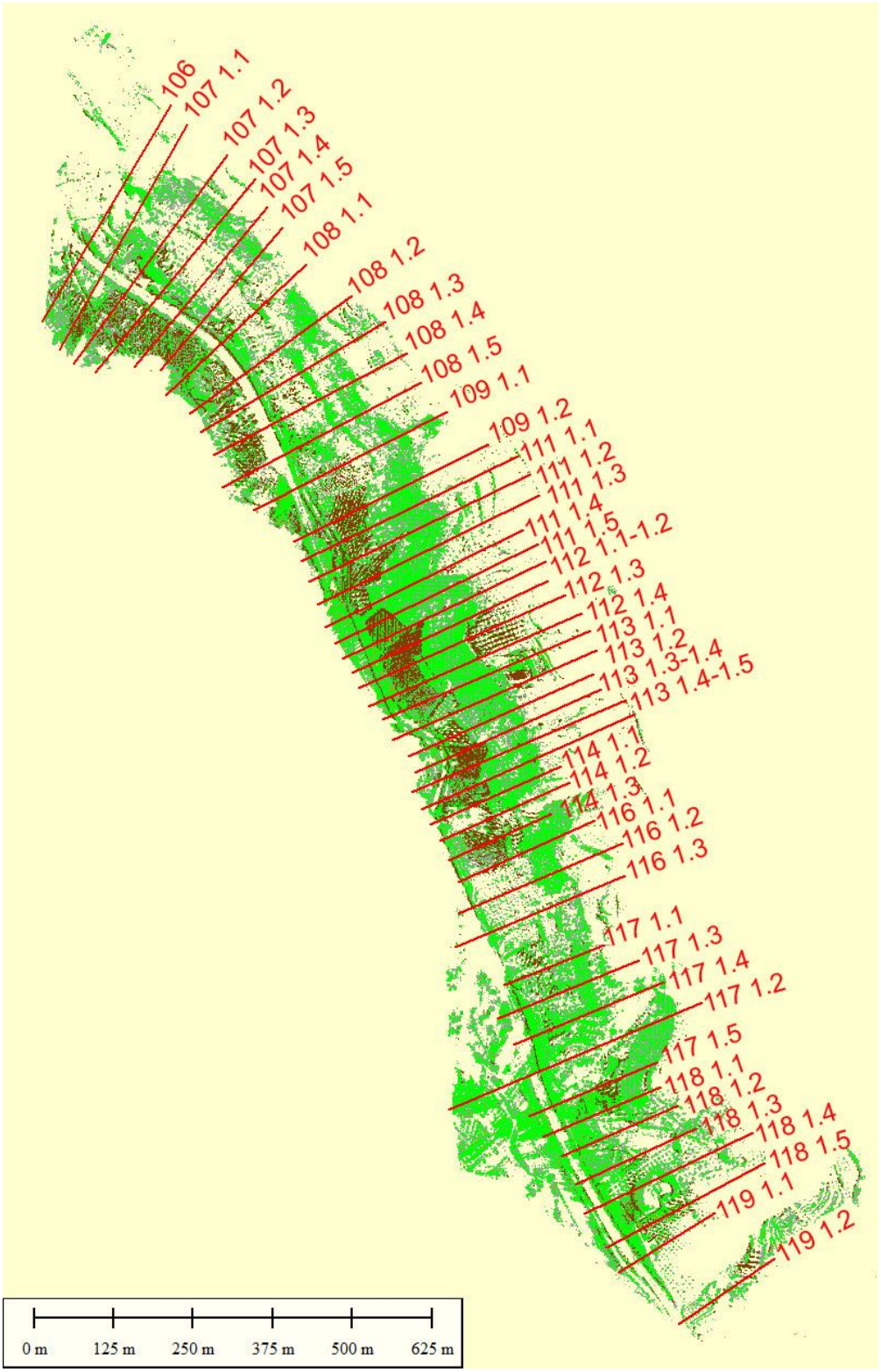

Figure 31. The position of the cross sections on the Stavrakia fault escarpment point cloud in Global Mapper.

3.2. Tyrnavos and Gyrtoni Faults

3.2.1. Regional Setting

3.2.1.1 Geology of the broader area

Tyrnavos and Gyrtoni faults are located at the borders of Tyrnavos basin NE Thessaly, Greece. During the last decades, Tyrnavos Basin has been thoroughly investigated using geological and geophysical methods especially along the major bordering faults.

Thessaly is located in central Greece and occupies the east side of the Pindus mountain range, extending from the Pagasetic Gulf and the Aegean Sea to the Macedonia region and Mount Olympus in the north. The Trikala and Larissa lowlands form a central plain which is surrounded by ranges of mountains. Thessaly is characterised by a great number of tectonic structures with varying orientations in a mainly extensional tectonic regime (Caputo and Pavlides, 1993) and a relatively shallow Moho (Caputo et al., 2004). These crustal and geodynamic conditions have a strong influence in the maximum dimensions of the seismogenic tectonic structures that are in the most cases no longer than 15–25 km and have a maximum seismic magnitude of about 6.6–6.7 (Aegean type faults) (Pavlides and Caputo, 2004). The maximum possible displacement that can occur as co-seismic surficial rupture directly caused by the seismogenic fault is of some tens of centimetres (Pavlides and Caputo, 2004).

The Aegean Region represents the area with the most important seismicity of the Mediterranean Sea and surrounding areas with a historical earthquake record of more than 2500 years. The term “Aegean fault” was first introduced by Hancock and Barka (1987), concerning their geometry and surface morphology, but later their kinematics and seismotectonic characteristics were also considered (Pavlides *et al*., 2006). The most common features of the Aegean faults are that they are dip-slip normal faults, 10–40 km long and are usually active since Middle – Late Pleistocene, exhibiting moderate to strong earthquakes (Ms≈6-7). The maximum vertical displacement ranges from some tens to a few hundred centimeters and have return periods of hundreds to thousands of years (Pavlides *et al*., 2006).

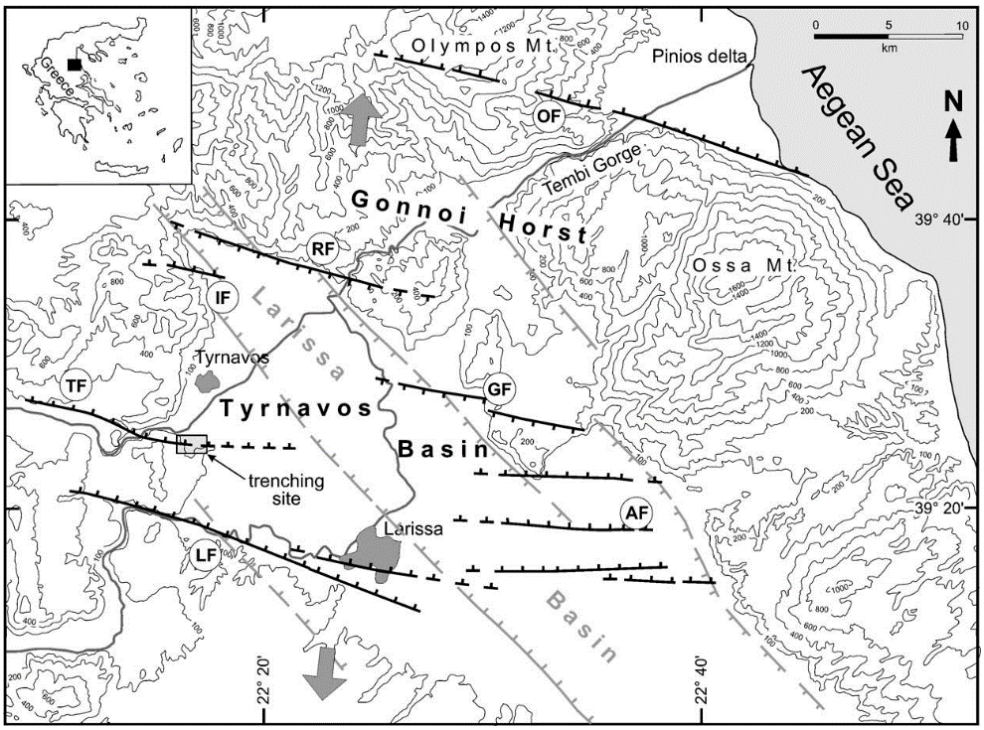

Figure 32. Simplified tectonic map of eastern Thessaly. Black lines: active structures affecting the area since Middle Pleistocene associated to the E–W trending Tyrnavos Basin and Gonnoi Horst. Grey lines: major Pliocene–Early Pleistocene faults bordering the Larissa Basin. Barbs on the downthrown side of the faults. TF=Tyrnavos Fault; RF=Rodia` Fault; IF=Ligaria` Fault; GF=Gyrtoni Fault; LF=Larissa Fault; AF=Asmaki Fault; OF=Omolio Fault. Large grey arrows represent the active stress field affecting the area *(Caputo et al., 2004).*

The structural architecture of Thessaly, result of several deformational phases, has a dominant horst and graben topography. This is due to the ENE-WSW Oligocene - Miocene compressional phase producing the orogenesis of the External Hellenides in association with the Pliocene-Early Pleistocene tectonic inversion associated to post-orogenic collapse (Caputo and Pavlides, 1993). The major morphological and tectonic imprint caused by this crustal extension was the formation of the 60-km-long Larissa Basin. During this extensional phase, the Larissa basin was characterized by fluvial and mainly lacustrine conditions that persisted till Villafranchian. After a period of quiescence, during the Middle - Late Pleistocene a new roughly N–S extension affected the Aegean Region. This tectonic event is characterized by pure extension, with a N10°E average direction of the least principal stress axis, σ3. As a consequence, the new geodynamic conditions generated a new system of normal faults trending E–W to ESE–WNW, leading to the development of Tyrnavos basin. In particular, this younger tectonic structure has been superimposed onto the inherited NW -

SE trending one, i.e. the Larissa Basin, thus forming the complex blocky pattern we observe nowadays (Caputo *et al*., 2004).

Tyrnavos Basin is an E-W trending graben bordered by two major antithetic sets of rightstepping dip-slip normal faults that began forming during Middle Pleistocene as a consequence of the N-S extension which affected the whole Aegean Region. Some of the inherent extensional structures were locally or partially reactivated with oblique slip kinematics, with most of the new faults cutting-across the pre-existing ones. The major faults that delimit the basin, are mostly the Rodia and Gyrtoni south-dipping faults and the Tyrnavos and Larissa north-dipping faults, , to the north and south respectively (Caputo *et al.*, 2004). Both of these two sets show a partial overlapping right-stepping geometry and consist of complex shear zones and are commonly segmented (Caputo *et al*., 2003).

3.2.1.2. Fault Characteristics

Tyrnavos fault is located just a few kilometers south of the city of Tyrnavos and is characterized as a typical "Aegean type" active fault according to geological, structural, morphotectonic and geophysical studies. The general trend of the Tyrnavos fault is E – W, though it shows a slightly right-bending geometry. The well-defined fault trace has been mapped in detail for more than 12 km. Based on remote sensing techniques, it can be followed eastwards across the northern Larissa Plain with a possible maximum length of about 20 km (Caputo *et al*., 2004).

The area that is affected by Tyrnavos Fault mainly comprises of basement rocks of Middle Triassic – Jurassic crystalline limestone, part of the Pelagonian geotectonic zone and Pliocene and Quaternary deposits. The thickness of the crystalline limestone and Pliocene deposits is estimated to be 300 m and 100 m respectively. The Pliocene deposits consist of fluvio – terrestrial formations overlying lacustrine and fluvio – lacustrine formations (Caputo *et al*., 2004).

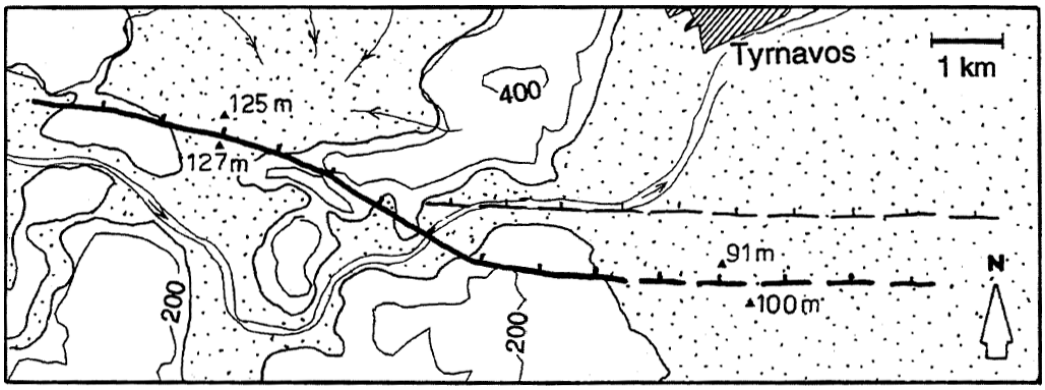

Figure 33. Sketch map of Tyrnavos Fault with the surrounding Middle Pleistocene-Holocene deposits (Caputo, 1995)

The Tyrnavos Fault according to sedimentological, structural and chronological data shows a Late Pleistocene to Holocene activity, characterised by vertical co-seismic displacements of 20–40 cm with a possible recurrence interval of about 2–2.5 ka. Based on the 'magnitude versus surface rupture length' empirical relationship specifically proposed for the normal faults of the Aegean Region (Pavlides and Caputo, 2004) and assuming that the Tyrnavos Fault is reactivated all along its length. Conversely, by using the vertical displacement versus magnitude relationship, the maximum displacement associated to such an earthquake is 50–60 cm (Caputo *et al*., 2004).

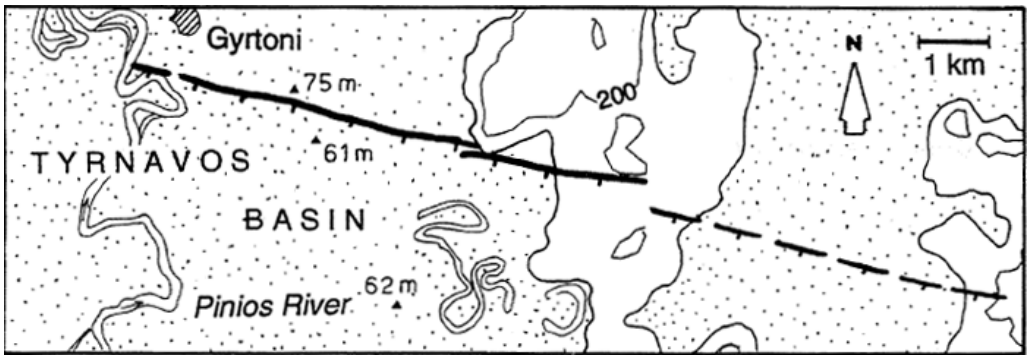

Figure 34.Sketch map of the Gyrtoni Fault with the surrounding Pleistocene-Holocene deposits. (Caputo, 1995)

Gyrtoni fault is located near the Gyrtoni village, 13 km north from Larissa city, with a population of about 163,000 (HSA, 2011), making the research of this fault of is of great importance (Tsodoulos *et al*., 2016). It is 12-13km long, south-dipping, dip-slip normal fault with an ESE-WNW strike. It is parallel and synthetic to the Rodia Fault and has an

approximately 10–11 m high degraded composite morphological escarpment distributed across a 200 m wide zone parallel to the fault

Due to fact that the fault scarp is developed in poorly cemented lacustrine deposits, of probably late Villafranchian age, it is heavily and irregularly eroded, thus, the precise location of its trace is not easily identifiable in the field (Oliveto *et al*., 2004). The electrical resistivity topographies combined with the palaeoseismological trench investigation confirmed the occurrence of an emergent fault plane close to the lower part of the escarpment (Koukouvelas *et al*., 2013). From a geomorphological and palaeoseismological point of view, the fault can be classified as of moderate activity rate with an abundance of, even though discontinuous, geomorphic evidence of its activity. The two paleoseismological trenches that were made in the area provide evidence of possibly four faulting events with an average recurrence interval (1.39 ± 0.14 ka) and a slip rate of (0.41 ± 0.01 mm/a) (Tsodoulos *et al*., 2016).

The hanging-wall is characterized by continuous alluvial deposition of sands and silts, at least from Late Pleistocene (Caputo *et al*., 1994). In the footwall block horizontal well layered lacustrine and marsh deposits of Villafranchian age crop out, showing features related to syn- and post-sedimentary seismic activity (i.e. seismites).

3.2.1.3. Tyrnavos Trench Characteristics

The trench, as described by Caputo *et al*. (2006, 2004) is the westernmost one and intersects the fault zone and it is oriented N–S, perpendicular to the local trend of the fault trace, that is locally represented by a more than 1 m. high morphotectonic scarp. The trench is nearly 3 m wide and about 10 m long, though the detailed log has been performed only for the 8 m closer to the contact zone. The trench cuts through the fault zone and it has been excavated 2–3 m into the bedrock of the footwall block, locally softened and parted by intense vertical fracturing. Close to the main fault plane, fractures are well developed, well connected and extending much deeper. It must be noted that at about 3 m depth from the top surface, fractures are open up to several centimeters.

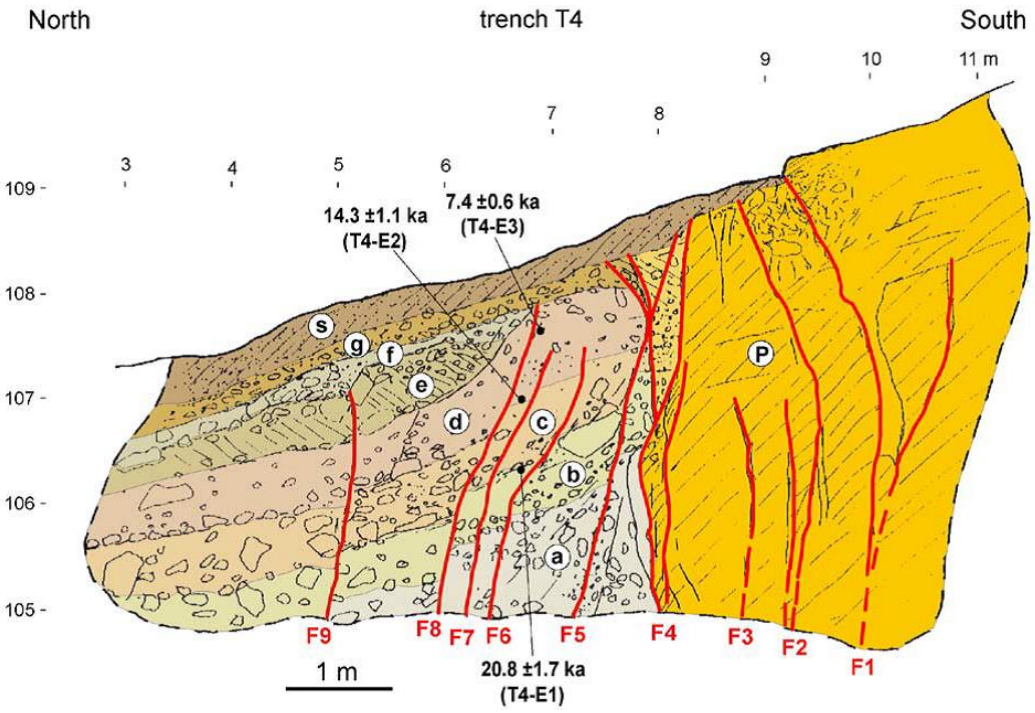

Figure 35. The log of T4 trench (eastern wall) as was excavated across the tectonic contact between Pliocene–Lower Pleistocene carbonate and the latest Pleistocene–Holocene aluvial and colluvial deposits. Letters within white circles refer to sedimentary units while faults are numbered. Black spots represent the dated samples. (Caputo et al., 2004)

The footwall block consists of Pliocene – Early Pleistocene oolitic calcarenite, with subhorizontal layers, ranging from medium to thick, that are locally welded together. These sediments were probably formed in a seashore environment along the coastline of the Villafranchian Thessalian lake and belong to the fluvio – lacustrine formations of the Larissa basin. These carbonate deposits partly overlap, with a strong angular unconformity, the Triassic crystalline limestone. The hanging-wall block, on the other hand, is covered by a sequence of Late Pleistocene – Holocene alluvial–colluvial sediments forming at least six sedimentary units (Caputo et al., 2004).

The composition of the detrital clasts in the alluvial – colluvial sequence is fairly uniform, mostly carbonate. This is due to the composition of the surrounding source rocks and the footwall block. Clasts are from millimeters to decimeters in size and generally subangular to angular in shape. Matrix is commonly abundant and only locally the texture is clast-supported. Slight variations of the matrix color, the size and distribution of clasts, some incipient pedogenesis on top of the strata and a locally observed fining-upwards gradation allow the layering to be distinguished and at least seven separate sedimentary units to be

recognized. The layers dip northwards and their thickness range from 25 to 80 cm, locally showing a wedge-shaped geometry. The sequence is covered by an incipient brown soil consisting of fine grained material rich in organic matter with scattered subangular carbonate clasts, which represents the present-day pedogenic layer and is around 30 cm thick. It also seems to be affected by faulting, being reduced to 10–15 cm, and it further thins out till disappearing on top of the footwall block. The entire sequence, with the exception of the soil layer, is cut by several fracture planes that show variable displacements, from a few up to 50 cm each (Caputo et al., 2004).

3.2.2. Methodology

3.2.2.1 Data Acquisition

The fault plane from the palaeoseismic section of Tyrnavos and the Gyrtoni escarpment was surveyed during early April 2014, in a period of two days. The goal of the scanning operation was to identify possible applications of LIDAR technology on fault planes from palaeoseismological trenches and heavily eroded fault scarps.

Figure 36. The area of Tyrnavos town with palaeoseismological trench cite, where the fault plane was surveyed, pinpointed.

A close range survey was required for the purpose of the palaeoseismological trench analysis, 10m perpendicular to the fault plane, for a high density point cloud to be created. The point cloud consisted from 28,650,740 (28.6 million) points and was comprised of the fault surface. The walls of the palaeoseismological trench were ignored during the data processing because there wasn't any information to extract from them via non colorized 3D model.

Figure 37. The Tyrnavos palaeoseismological trench during the scanning process. Picture taken by the ILRIS-(3D-HD) laser scanner.

The Gyrtoni fault escarpment was scanned from a mean distance of 103m perpendicular to it and was consisted of 2,603,978 points. The area was covered by low vegetation due to agricultural activities and so, only the morphology of the escarpment was visible in the area. The area of the scan station was chosen mainly for its accessibility and the fact that a large part of the escarpment was visible. The escarpment had a maximum height from its base of 12m and thus was difficult to analyze with traditional geological methods.

Figure 38. The area of Gyrtoni town with the scan station for the fault escarpment, pinpointed.

Figure 39. The Gyrtoni fault escarpment during the scanning process. Picture taken by the ILRIS-(3D-HD) laser scanner.

3.2.2.2 Data Processing

3.2.2.2.1 Tyrnavos Palaeoseismological Trench Fault Plane

The scan data was first processed with the pifedit and IMAlign modules of Polyworks to remove the unnecessary part, remove scan noise and filter the data. The scans were then aligned together and merged in a single scan in order to create a detailed polygonal model. In IMEdit different types of the fault plane curvature were generated but only the maximum curvature showed clear results. Unfortunately due to the small size of the fault plane and the

fact that it was buried underground, there wasn't any useful information to be extracted from the virtual model.

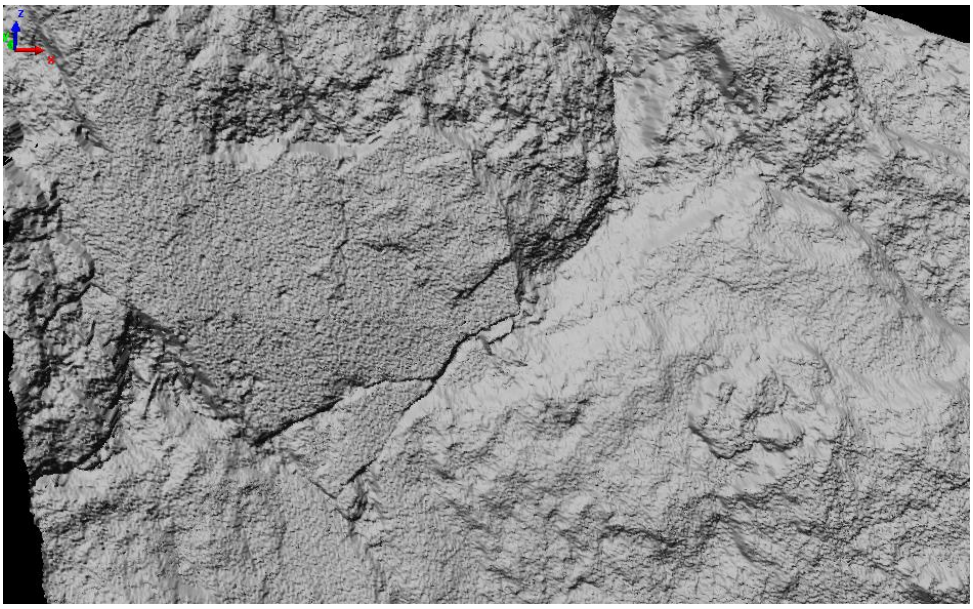

Figure 40. The fault plane surface detail from a close view. The high density of the point cloud allows for a detailed representation of the target object, and thus for a more accurate observation and study of that object.

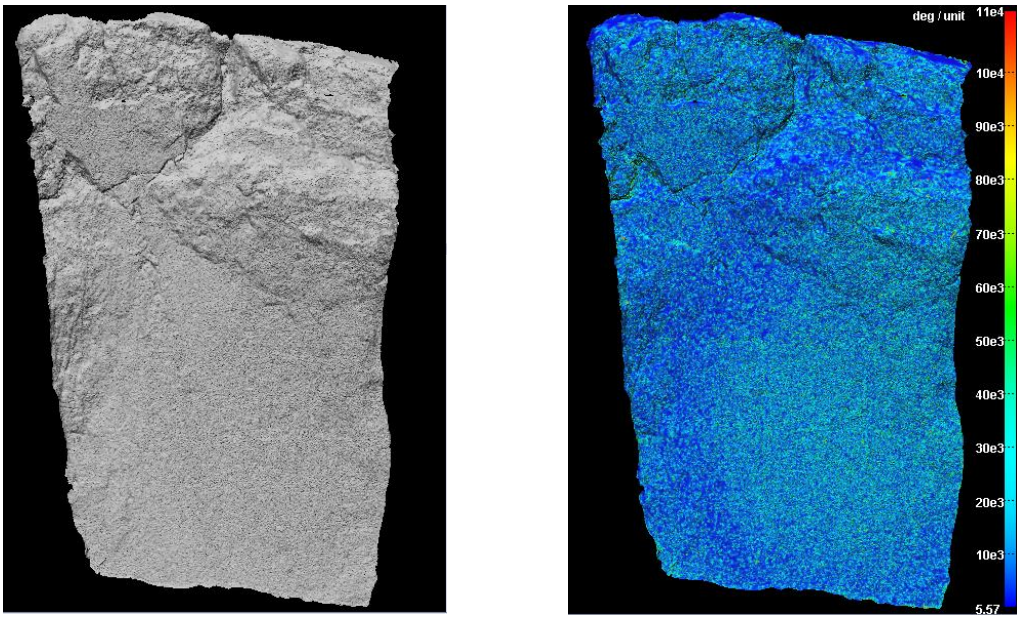

Figure 41. In the left the virtual model and in the right what the maximum curvature analysis showed. The units are in millimeters.

In Fig. 41 the left picture shows the polygonal model of the Tyrnavos fault plane without any of its surroundings before any analysis was made on it. The right picture shows

the polygonal model with the resulted Maximum Curvature Analysis with the scale on the right side of the picture. The results of the curvature analysis shows a rather smooth plane without a notable deviation from the mean plane of the fault surface. Due to the fact that the curvature analysis of Polyworks, operates in a small scale, it emphasizes more on the roughness of the surface. In the resulting plane in Fig. 41, a half circle of smoother values is visible in a darker blue color, which is the area with the smallest values of maximum curvature. The nature of this plane and the spatial dimentions of the plane does not allow for a conclusive interpretation of the results, and further investigation is required.

3.2.2.2.2. Gyrtoni Fault Enscarpment

All of the scanning data of the area was directly imported to CloudCompare as the alignment tools of Polyworks were inadequate for aligning the specific scans. That was due to the fact that there were almost no identifiable common points between the scans and for that reason a different alignment approach was tested. The scans were manually positioned, according to their geometry, close to the position they should be, all of them locked in the same y-z plane. Then using the automatic alignment of the program they were accurately aligned and merged together.

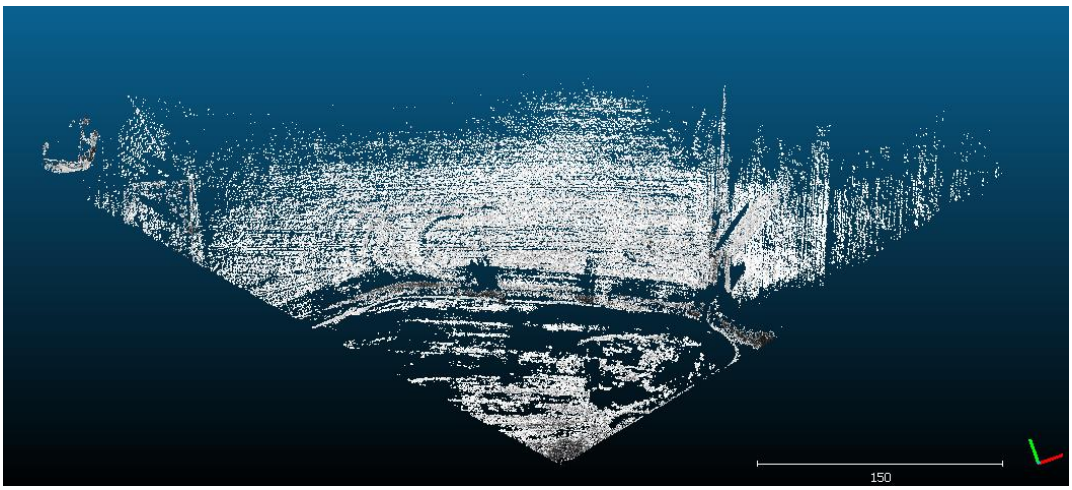

Figure 42. Point Cloud with computed normals of the Gyrtoni escarpment.

Due to the nature of the fault scarp, which is highly eroded and covered by vegetation, eventually, there were not methods we could use with 3D modeling that could produce any

significant information with the current data. However, a detailed representation of the area was created and the maximum escarpment height was calculated at 12m (with an average of 10.3m) and its maximum slope at 8° (average 6.47).

3.3. Messinia Basin – Pidima Fault

3.3.1. Regional Setting

Pidima fault is located in the Messinian basin, part of Peloponnesus region in Southern Greece. It belongs to the Eastern Messinia Fault Zone (EMFZ); its trace can be found in the western side of the Taygetus mountain range, close to Arfara and Pidima villages.

Messinia is located in SW Peloponnesus and is delimited by the Taygetus mountain range in the east and the Ionian Sea to the west with the Gulf of Messinia to the south. The most important mountain ranges are Taygetus in the east, Kyparissia in the northwest and mount Lykodimo in the southwest. The area is one of the most tectonically and seismically active in the Hellenic Arc, mostly because it is located about 60 km from the Hellenic trench, where the African plate subducts below the Eurasian one (Mariolakos and Spyridonos, 2010).

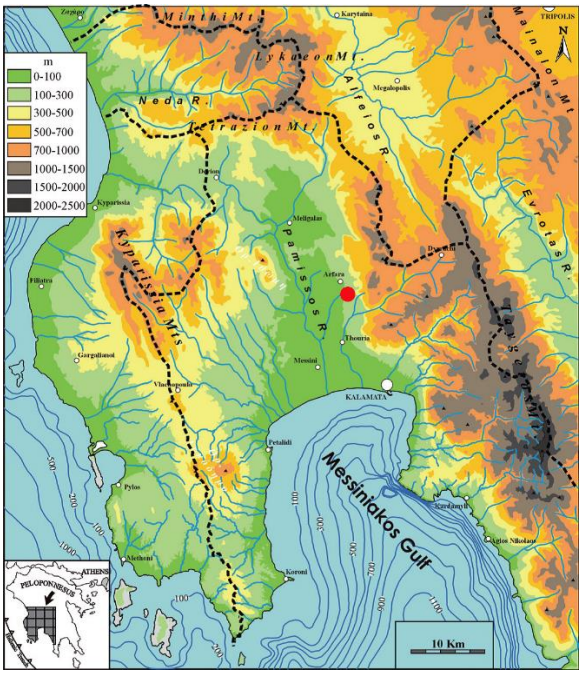

Figure 43. The area of SW Peloponnesus with the Messinian basin deliminated. The red dot indicates the area around Pidima village where the Fault Plane is located (modified from Fountoulis et al., 2014).

According to Fountoulis et al. (2014), the SW Peloponnese, is comprised by four Alpine geotectonic units from base to top: a) Mani Unit consisting of crystalline carbonates and a metaflysch, occurring mainly in Taygetos Mt.; b) the Arna Unit consisting of metamorphic rocks (schists, phyllites and quartzites) also in Taygetos Mt.; c) the Gavrovo-Tripolis Unit consisting of Mesozoic to upper Eocene neritic carbonates, and Upper Eocene – Oligocene flysch; and d) the Pindos Unit consisting of Mesozoic pelagic sediments and Paleogene flysch (see Fig.42).

The Messinian basin in particular, consists of two major alpidic geotectonic units, the tectonic zones of Gabrovo - Tripolis and Olonos – Pindos (Mountrakis, 2010). The central part of the basin is covered by post alpine sediments of Pliocene to Quaternary age, unconformably overlying the basement. The thickness of these sediments is large in relation to the basin extend and in the central part it exceeds 280 m. On the western boundary of the basin the sediments are deposited unconformably on the Olonos – Pindos unit rocks, mainly on radiolarites, Upper Cretaceous limestones and flysch. On the northern and the eastern part, the sediments are tectonically in contact with the alpine formations, as a result of the activity of the boundary fault zone of the Kalamata – Kyparissia Graben. To the south and southeast, the post alpic sediments cover the Tripolis unit flysch and limestones respectively. To the southwest the basin is connected by a narrow plain zone, covered by post-alpine sediments of small thickness, to the Dorion - Kopanaki basin (Mariolakos and Spyridonos, 2010).

These sediments extend over 81 km^2 and can be divided in two geomorphologic regions. To the northern and eastern boundary of the basin, due to higher topographical slope alluvial cones prevail consisting of coarse grained material. The central part of the basin is flat and covered by fine grained sand and clay material of small thickness. The deeper sediment horizons consist of coarser grained material. At a depth of 25 – to 40 m, a clay horizon exists with thickness of about 5 to 20 m (Mariolakos and Spyridonos, 2010).

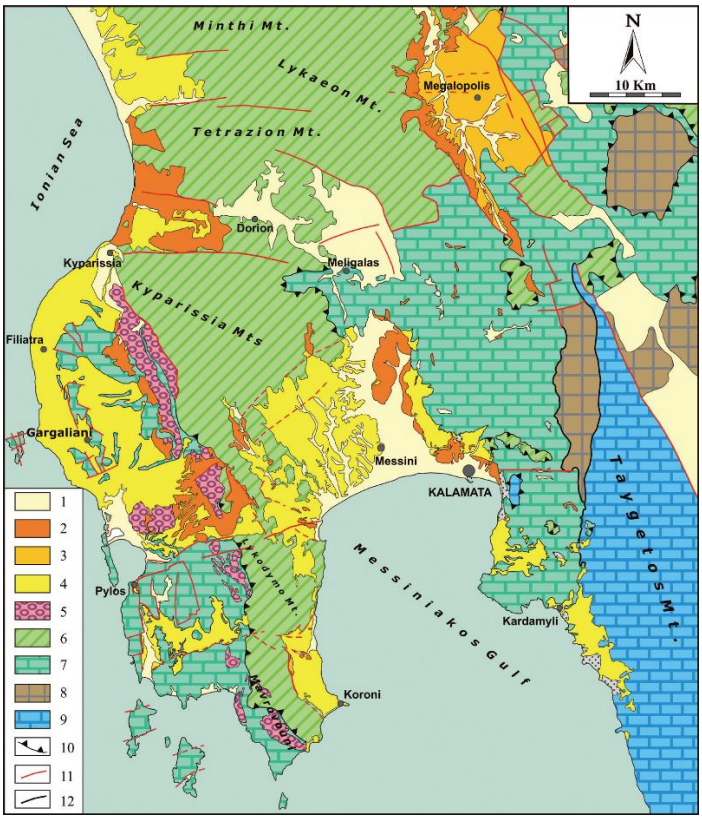

Figure 44. Map depicting the geotectonic units and the post Alpine deposits of the study area. 1: Holocene deposits; 2: continental deposits; 3: lacustrine deposits; 4: marine deposits; 5: conglomerates of Messinia (molasse); 6: Pindos Unit; 7: Gavrovo-Tripolis Unit; 8: Arna Unit (Phyllites-Quartzites); 9: Mani Unit; 10: thrust; 11: fault zone; 12: detachment fault zone. (Fountoulis et al., 2014)

The Neotectonic structure of SW Peloponnesus is characterized by the presence of tectonic grabens and horsts striking NNW-SSE and E-W. The morphology in the broader fault area presents high angle slopes with an elevation ranging from 16m in the Pidima area to 1272m in the Vromovrisseika Mts. The deformation in this area is mostly caused by the EMFZ, which delimits the western side of Taygetos mountain range and coast of Mani peninsula (Valkaniotis *et al*., 2015). It consists of a primarily normal fault system, dipping NNW-SSE to N-S and attaining a total length of more than 100 km from the northern Messinia plain in the north to the southern part of Mani peninsula (Valkaniotis *et al*., 2015). EMFZ has its continuity disrupted by overlapping faults, which in turn form many relay ramp structures across its length (Valkaniotis *et al*., 2015). Measurements of the fault striae along fault planes of the fault zone indicate a WSW-ENE extension, which is in accordance with the focal mechanisms of modern seismicity.

In the northern part of the Pidima fault segment, which is one of the most prominent active segments of the central part of the EMFZ, a palaeoseismological trench was excavated in order to examine the palaeoearthquake record of the fault system (Valkaniotis et al., 2015). The palaeoseismological trench and the accompanied research were funded by the Aspida project.

3.3.2. Methodology

3.3.2.1. Data Acquisition

The survey of the palaeoseismological trench and fault plane of the Pidima fault segment was carried out in late May 2015 using the ILRIS-(3D-HD) laser scanner. The detail that is required for depicting and analyzing both the palaeoseismological trench and the fault plane demands a close-range scanning, which is essential in order to have millimeter accuracy. The scanning process took place in one station 13m from the palaeoseismological trench and 10m away from the fault plane from which it could cover each one of them entirely and with no blind spots.

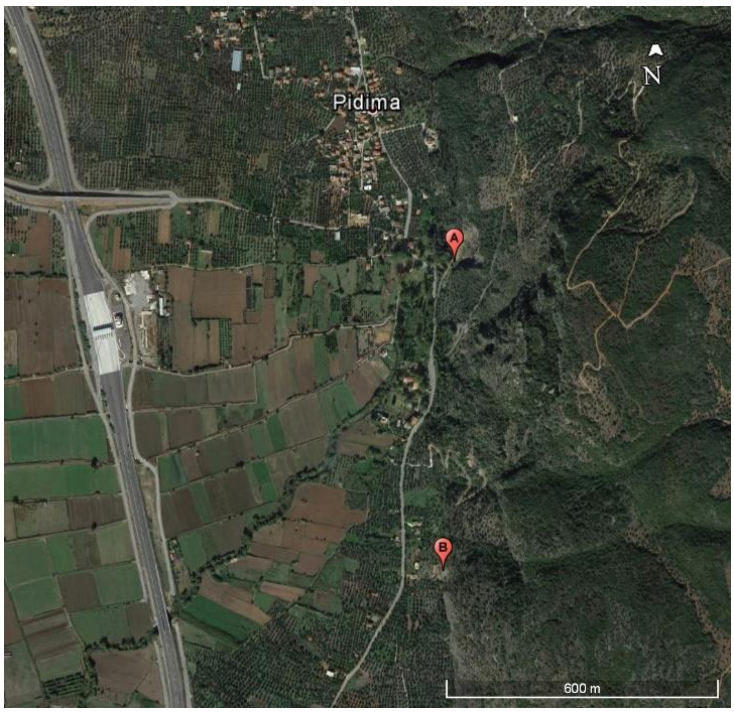

Figure 45. The area of Pidima village. A) The palaeoseismological trench cite, B) The fault plane cite

The data acquired for the palaeoseismological trench consists of three overlapping scans with a total of 9,436,368. The fault plane data is in the form of four overlapping scans along the length of the plane, consisting of 10,582,758 (ten and a half million) points in total. Due to heavy rain, the last scan was not possible to be completed, so the upper part of the southernmost part of the fault plane is not included. In addition, the weather conditions did not allow any field data to be collected for comparison with the 3D model analyses.

Figure 46. Picture of the Pidima palaeoseismological trench, during the scaning process, taken by the IRLIS 3D laser scaner.

Figure 47. Picture of the Pidima fault plane, during the scaning process, taken by the IRLIS 3D laser scaner.

3.3.2.2. Data Processing

As a first step, the scanning data was inserted in Polyworks, and with the pifedit and IMAlign modules, the point clouds were cleaned of the unnecessary parts and then aligned together as one point cloud. The average mean error of the overlap of the scans was 0.000041mm for both, with a standard deviation of +/-0.037 and +/-0.024 for the palaeoseismological trench and the fault plane respectively. Then the overlapping segments

between the scans were cleaned of the excess points, keeping the best data, in order to avoid increased point density in these areas (Fig 48-49).

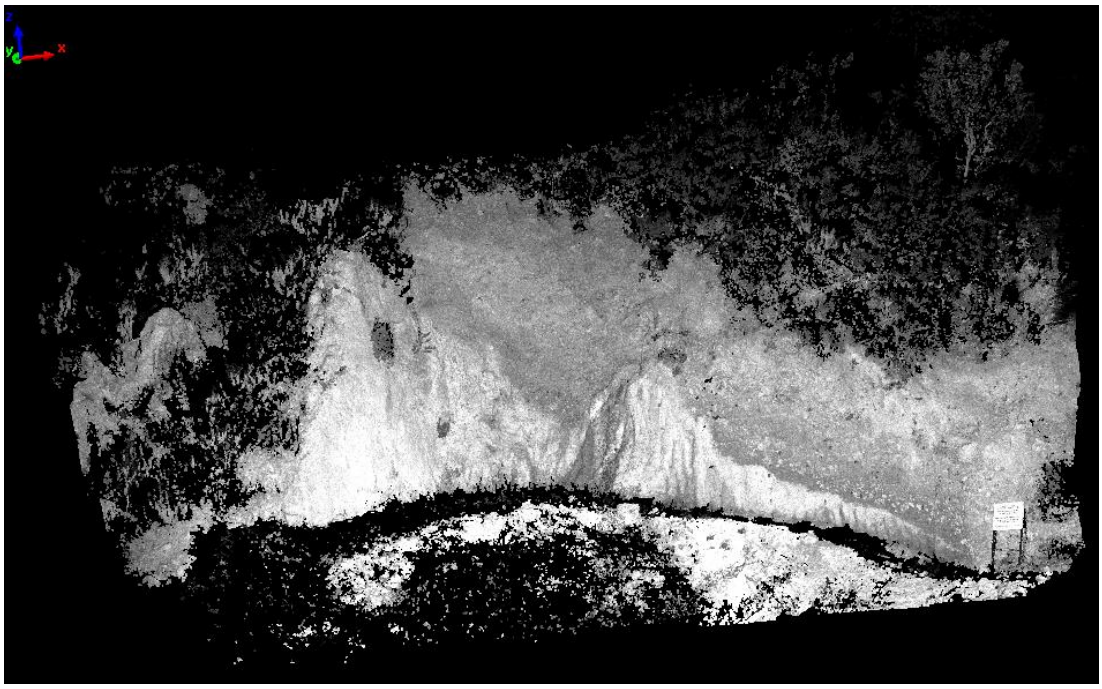

Figure 48. The original shape of the palaeoseismological trench at Pidima after the alignment and prior to any other editing in the Polyworks software platform

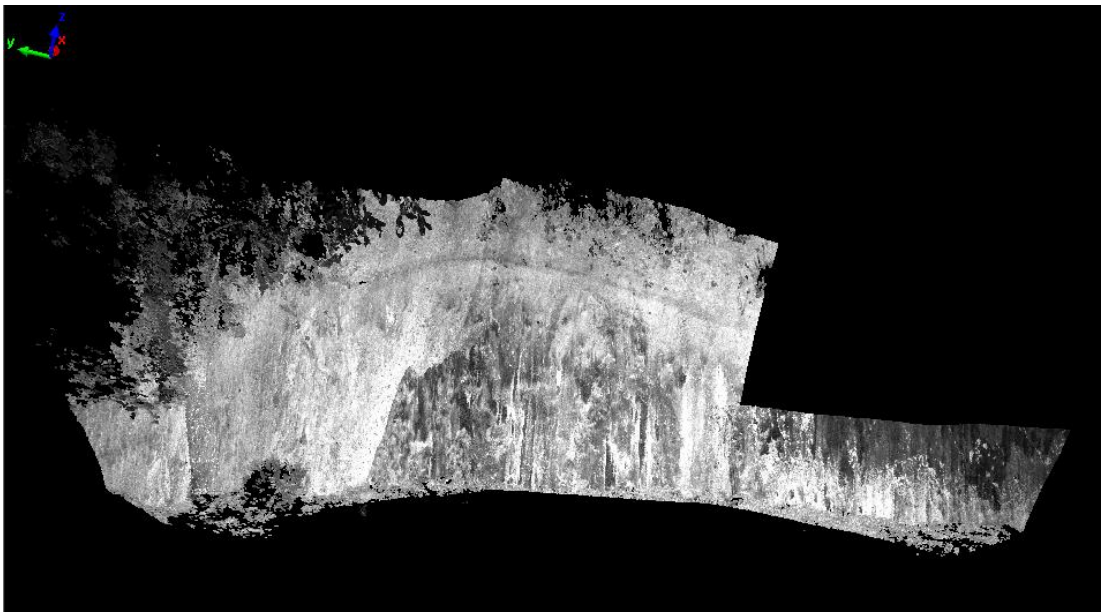

Figure 49. The original shape of the fault plane at Pidima after the alignment and prior to the unnecessary points removal in the Polyworks software platform.

With the IMMerge module, the point cloud of the fault plane was meshed and exported to IMEdit as a polygonal model. In IMEdit the mesh of the polygonal model was optimized in order to eliminate the triangulation noise of the surface and to generate the different curvature types of the fault plane. The point clouds of the Palaeoseismic Section and the Fault Plane, after the alignment, were also imported in CloudCompare for further testing.

3.3.2.2.1. Pidima palaeoseismological trench

Even though no significant geologic examination was able to be done in the Pidima palaeoseismological trench, the 3D point cloud model was very useful in presenting the results of the Automatic Point Cloud Classification method. The method is available in both Global Mapper and CloudCompare, the results of this method in Global Mapper were shown in the Stavrakia fault escarpment section of this Master Thesis. CloudCompare has a very different method to classify the points of a 3D model, which is via a plug-in called Capunno Point Classification.

The point cloud is imported in CloudCompare along with its intensity values, and a greyscale field generated as a first step (Fig.50). The surface normals are then computed, a perquisite for the point cloud classification (Fig 51).

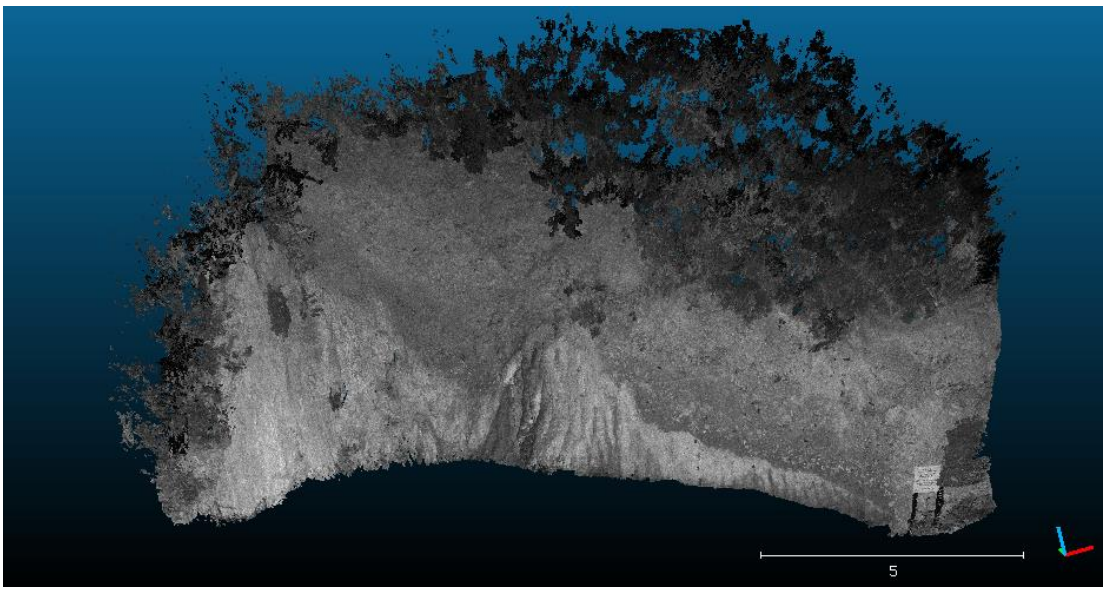

Figure 50. The palaeoseismological trench with the intensity values displayed through the Greyscale field, as imported in CloudCompare.

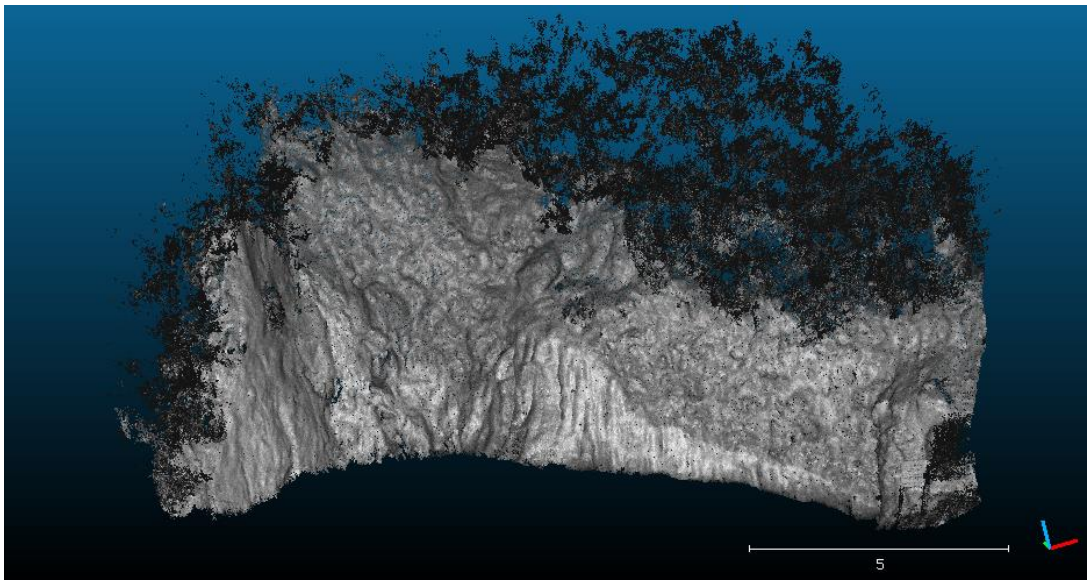

Figure 51. The palaeoseismological trench in greyscale after the surface normals were computed.

In order to classify the vegetation, a Vegetation Classifier is required to be loaded, or created by the user, through the plug-in, which allows it to start the analysis. The specific Classifier gave good results in this particular point cloud, classifying with little error the vegetation points (Fig. 52).

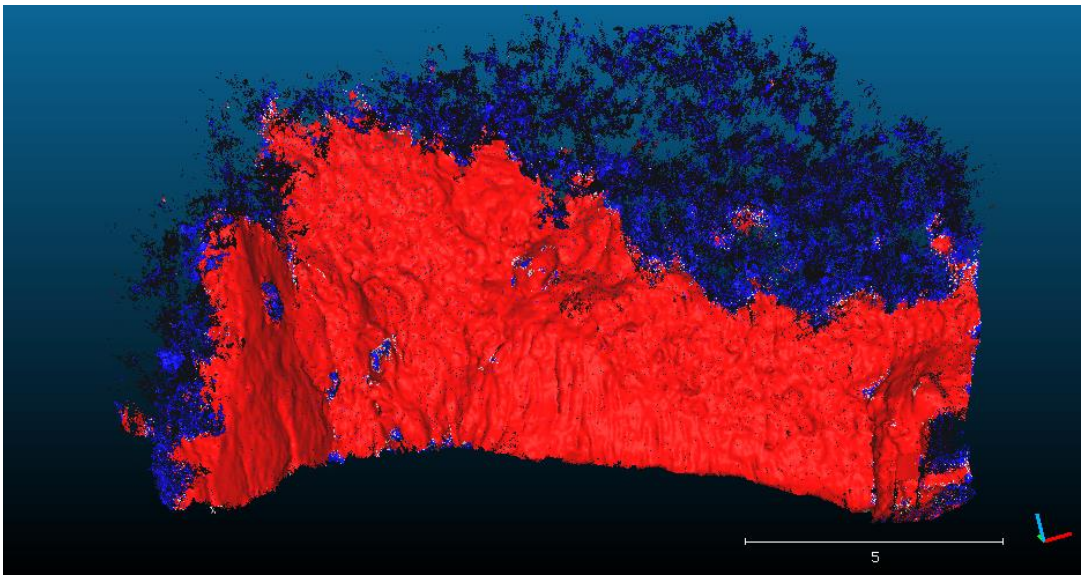

Figure 52. The palaeoseismological trench after the point cloud classification. The vegetation points are shown in blue, while the ground points in red.

After the Classification, most of the vegetation points were automatically removed, and with a little manual help, almost all of them were separated from the palaeoseismological trench (Fig 53).

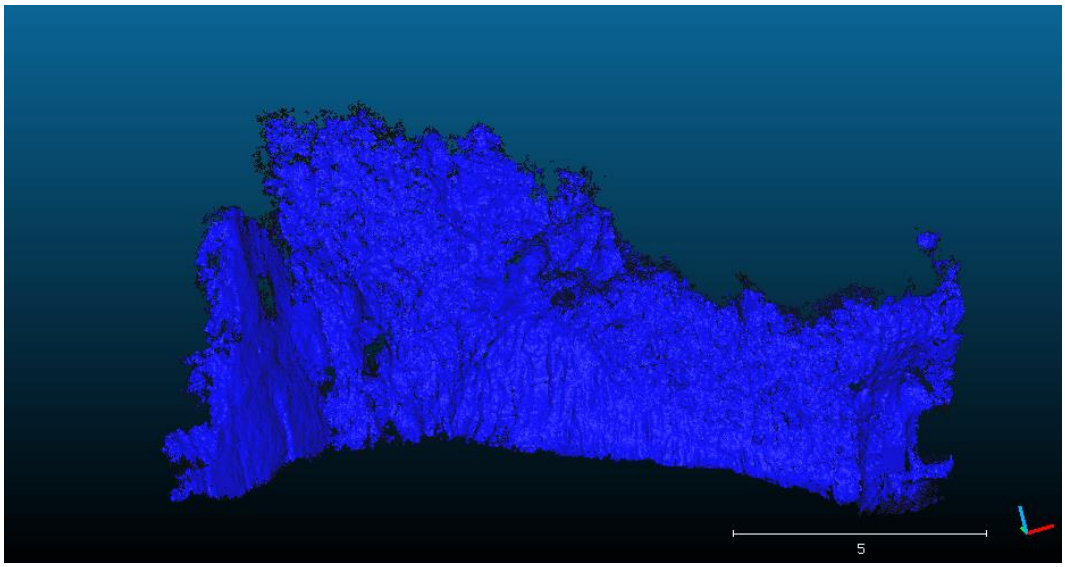

Figure 53. The palaeoseismological trench with only the ground points, after the removal of the vegetation points through the automatic removal.

This method is applicable and can give good results in most point cloud models, resulting in faster cleaning of the unnecessary points and therefore less time needed to prepare a 3D model for the analyses required. For the palaeoseismological trench was able to effectively clean the vast majority of vegetation points, leaving only the actual parts of the excavation than interest the researcher. At its current state, the 3D model is ready for accurate analyses to be conducted as most of the vegetation noise has been remove. For the current project, though, there was no available method for the continuation of the trench investigation and therefore future research is necessary for and valuable information to be extracted from the 3D model.

3.3.2.2.2. Pidima Fault Plane

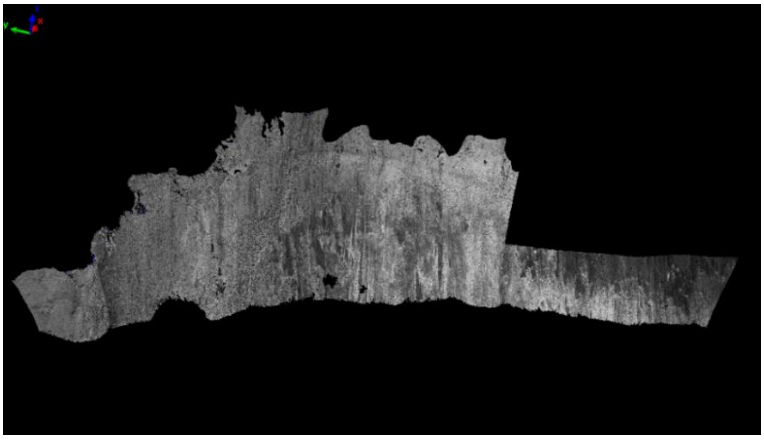

Figure 54. The fault plane clear of the vegetation and ground points, meshed, prior to any curvature analysis.

The scans were analyzed in order to identify the fault plane's curvature, roughness and its surface deviation from the average plane surface. First the Fault Plane's curvature was generated in Polyworks in the form of Maximum Curvature (Fig. 55). The way Polyworks estimates a surface curvature gave similar results on all the different curvature types it allows the user to generate, some of them being Gaussian, Minimum, Maximum, Mean, Total and a few others. Because the computation of the curvature is based on the triangulation of the polygonal model, it is highly dependent on the parameters that were chosen at the generation of the polygonal model and the smoothing operation done on it afterwards.

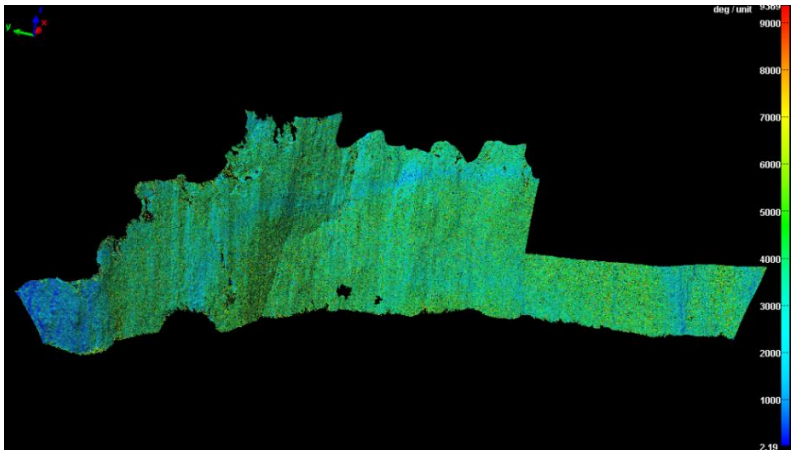

Figure 55. The results of Maximum Curvature Analysis in Polyworks. The units are in millimeters, the blue areas are the areas with the minimum values of the Curvature Analysis, meaning the areas with the lowest divergence between the points.

CloudCompare allows the user to check the available Scalar Fields of the data, which in our case is the Intensity Values. Also from the available Scalar Fields is easy to generate a greyscale field, giving the user more information about the intensity values.

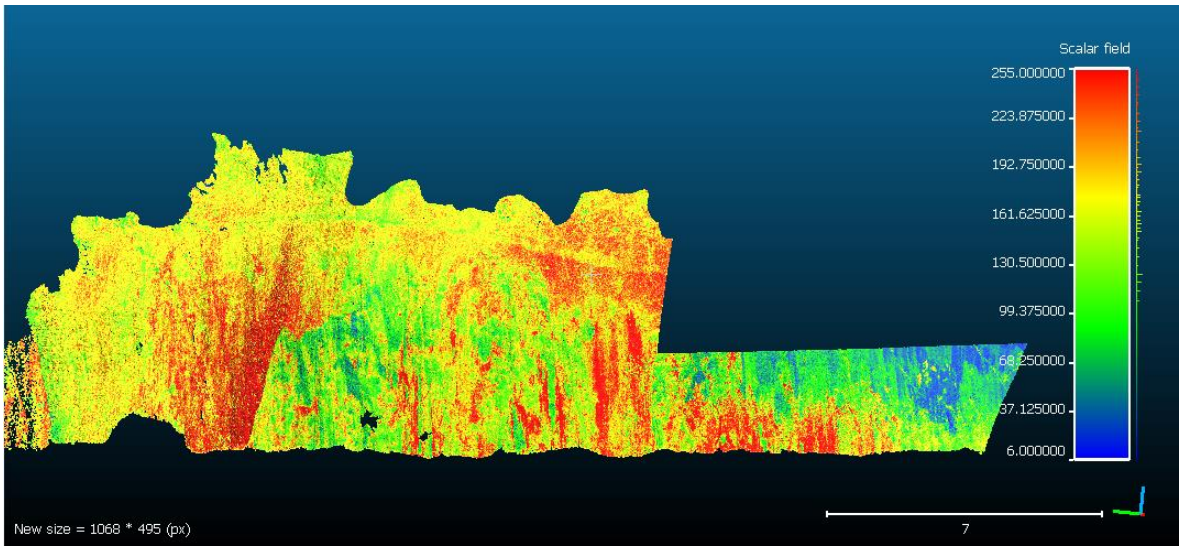

Figure 56. The Pidima imported in CloudCompare with the scalar field on. The scalar field is generated from the reflectance intensity of the materials, giving different values depending on the material.

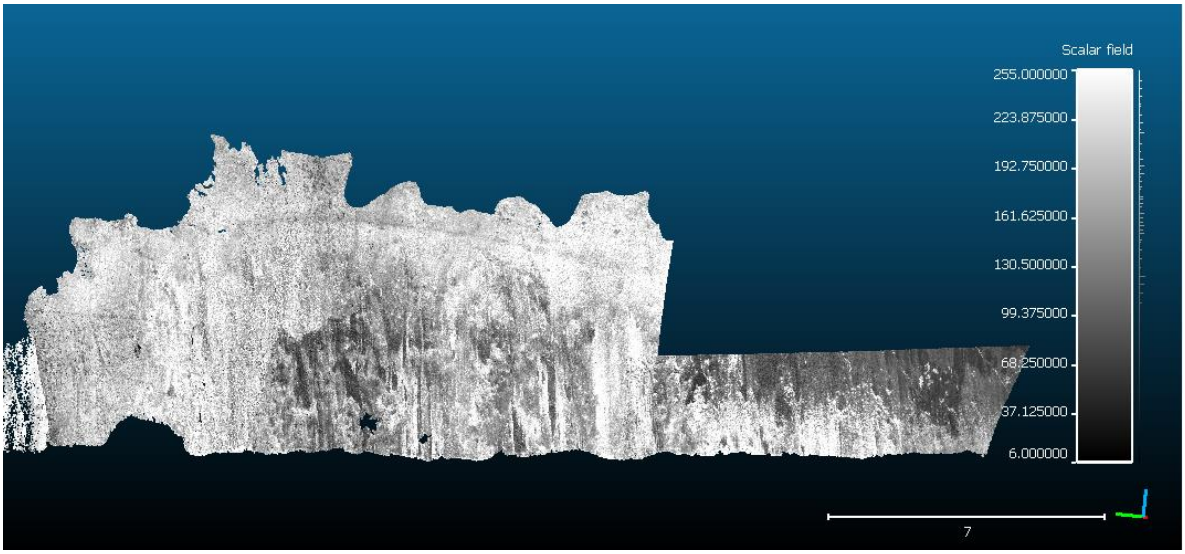

Figure 57. The Pidima fault plane with greyscale field on. The greyscale field is a variation of the regular Scalar Field giving a visual comparison of the intensity value of the materials instead of giving them different colors.

Because the PointClouds were missing normals, they had to be computed before any analysis was made. First the Gaussian and Mean Curvature were computed, using 3 different kernel sizes, the program's default recommendation at 0.02, as well as 0.1 and 1. Kernel is

defined as the radius of a sphere centered on each point in which the nearest neighbor points will be extracted around it to compute the mean value of the current analysis.

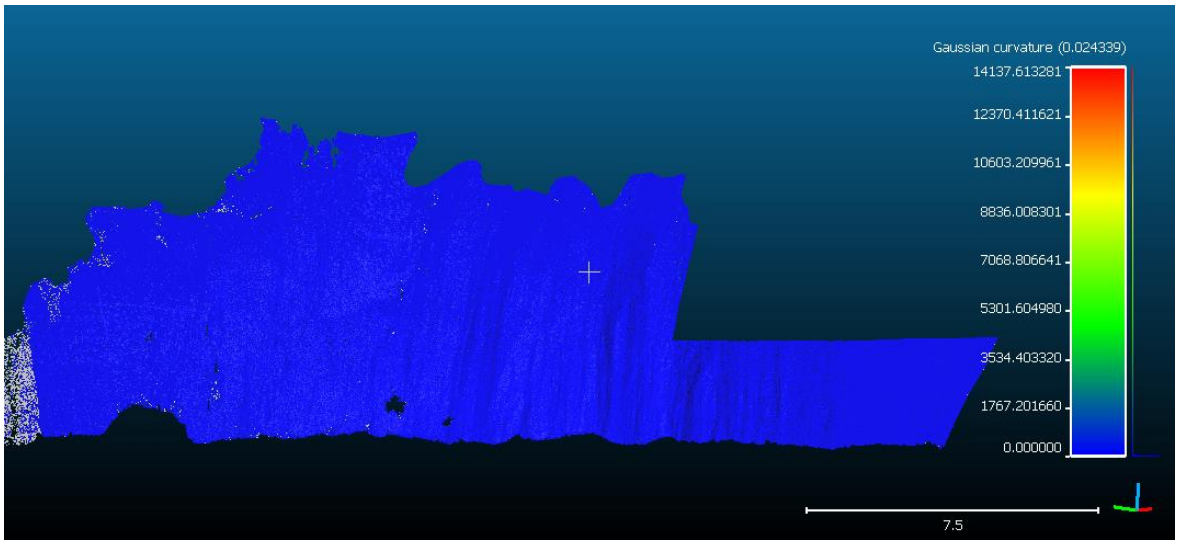

Figure 58. The result of Gaussian Curvature at kernel size 0.024. There are almost no differences between the curvature of the surface at this scale, giving a blue color in all the Plane Surface, except some grey areas where there was not possible for the curvature to be computed.

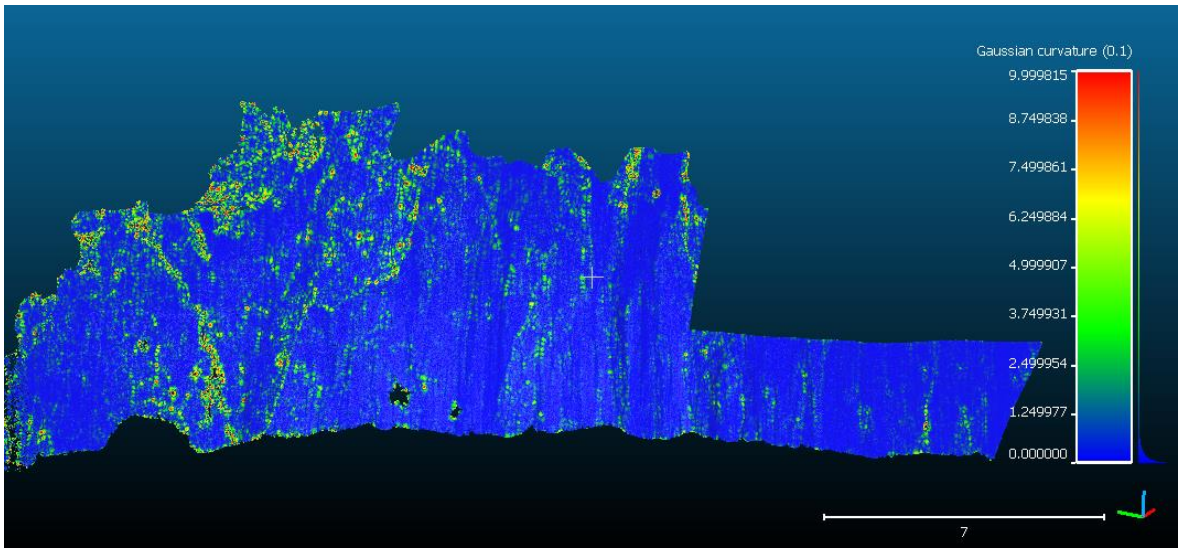

Figure 59. The result of Gaussian Curvature at kernel size 0.1. There are some areas of notable change in the curvature values, showing mostly areas of surface irregularities such as cracks, eroded areas etc.

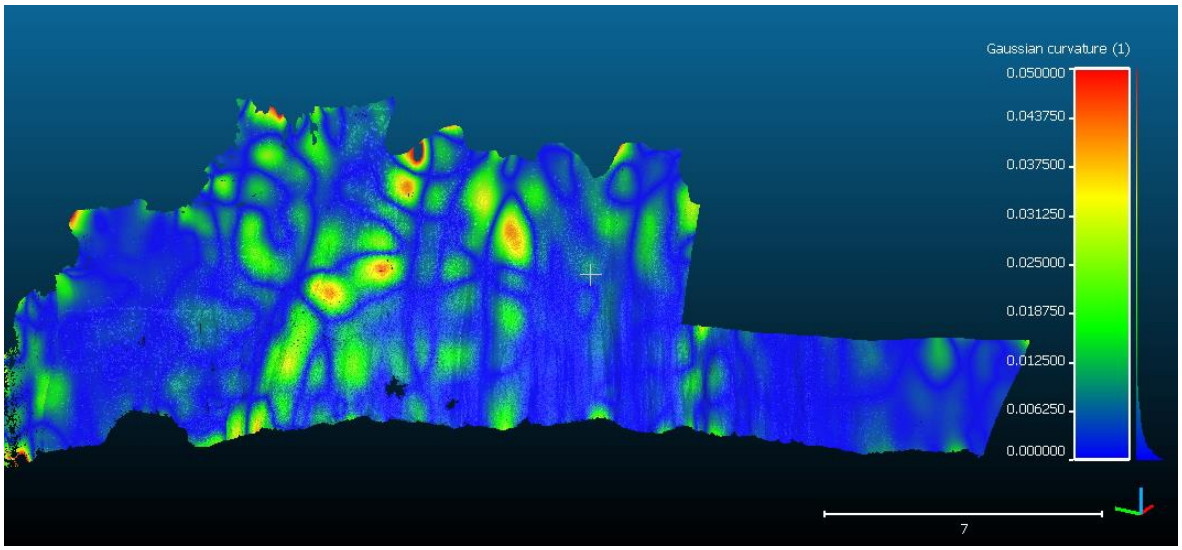

Figure 60. The result of Gaussian Curvature at kernel size 1. The Plane Surface exhibits some areas with significant curvature anomalies, possibly areas with a greater extend of surface anomalies and erosion damage.

In Fig. 58 to 60 are the results of Gauss Curvature analysis from CloudCompare which is better suited for identifying surface irregularities. The results are still hard to interpret and more knowledge on the subject is needed in order to extract any useful information from this method. The next step was to compute the Mean Curvature and the Roughness of the fault plane.

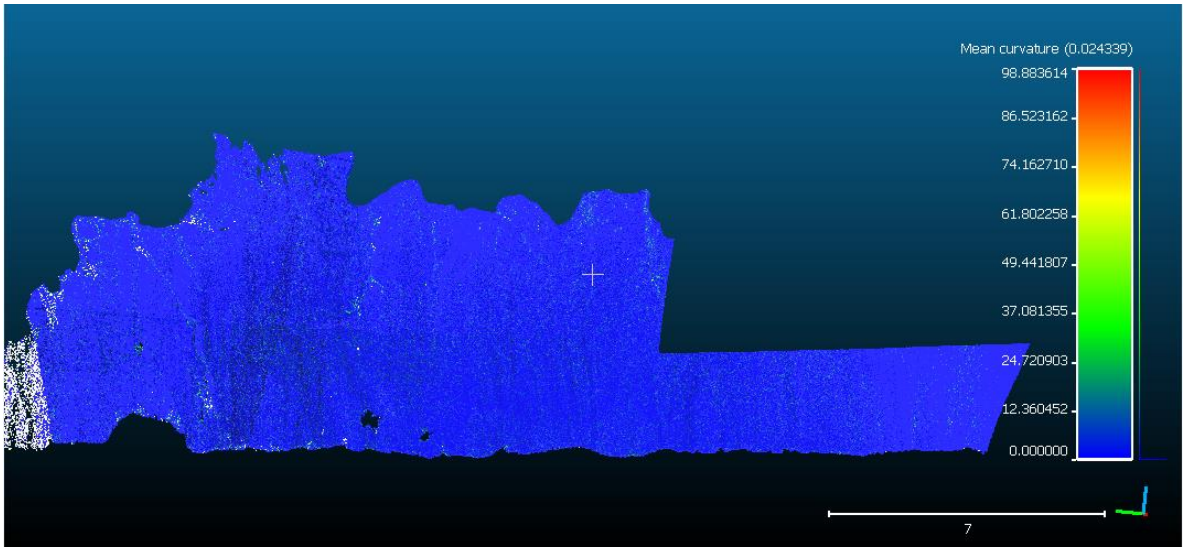

Figure 61. The result of Mean Curvature at kernel size 0.024. Again no notable difference in the surface curvature at this scale with some grey areas of high deviation between points.

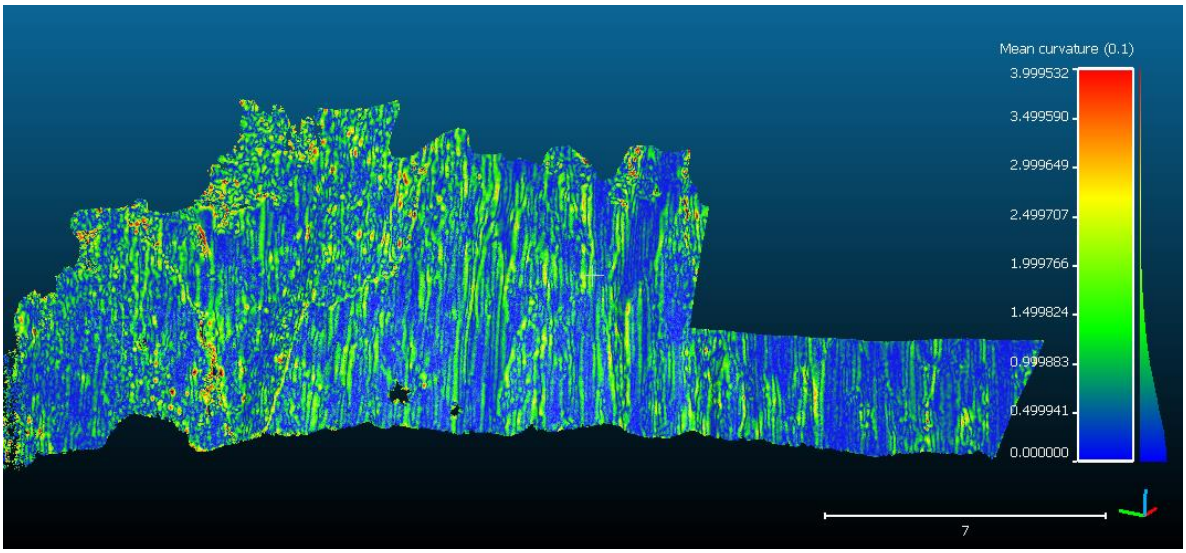

Figure 62. The result of Mean Curvature at kernel size 0.1. At this scale, the Mean Curvature is capable to show the fault plane's centimeter width lineaments, giving a good impression about their density, orientation and distribution.

The Mean Curvature of the fault plane gave the best results so far, about the geometry of the surface. From this analysis we are able to extract information about the fault plane's surface lineation and small scale corrugations, as far as 0.1 and 1 kernel sizes are concerned. The 0.02 kernel size in both Mean and Gaussian Curvature was not able to give any useful result in the fault plane, as they need a highly irregular surface in order to be able to display different values between points.

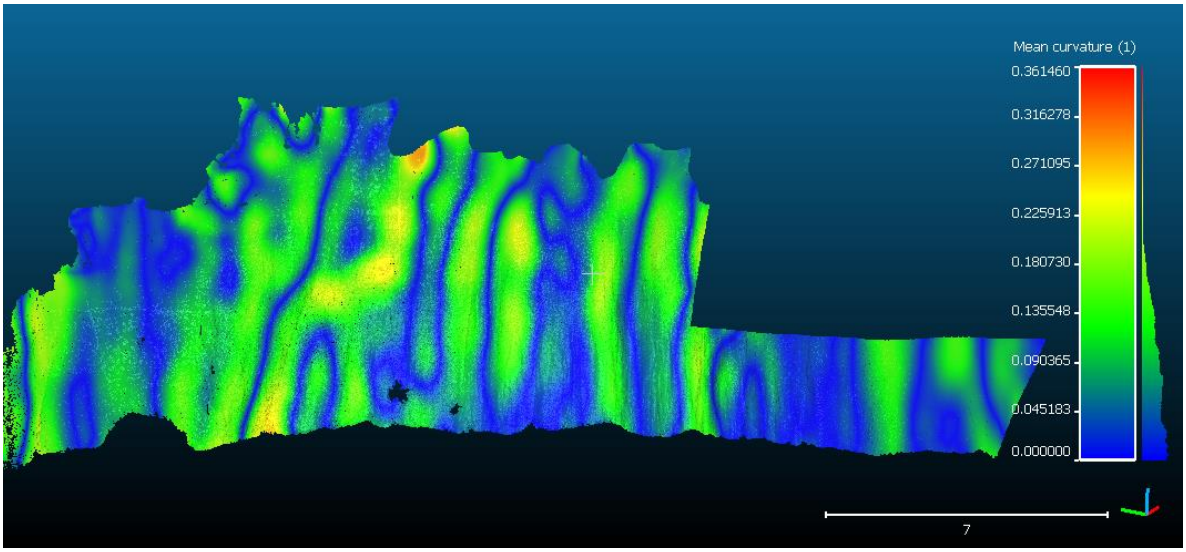

Figure 63. The result of Mean Curvature at kernel size 1. The Mean Curvature of the exposed surface of the fault plane was nicely shown with this process. The fault plane's corrugations are clearly visible here, as well as their density and orientation on the surface with an average width of 0.75 meters.

The surface roughness had by far the most varying results between different scales, displaying in each scale different types of geometrical structures. This method is far simpler than both the types of curvature analysis that CloudCompare offers.

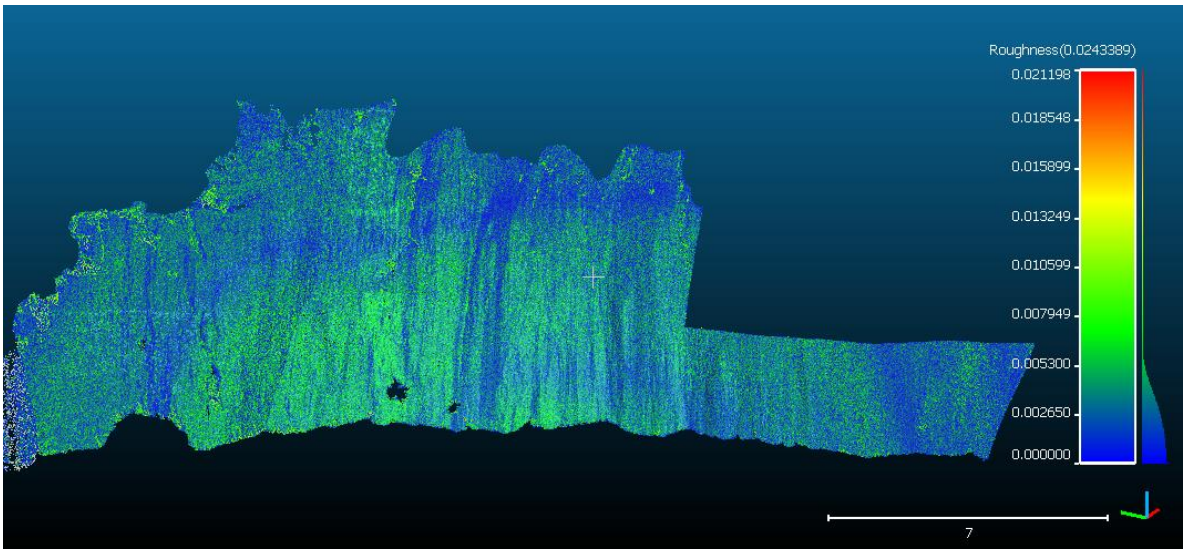

Figure 64. The result of the surface Roughness at kernel size 0.024. This analysis revealed an inner and outer half circle geometric structure, comprised of the points with the lowest values of Surface Roughness, and the indication of another circle at the fringes of the Plane exposure. The origin of these half circle structures may also be artificial in nature, even though this cannot be confirmed.

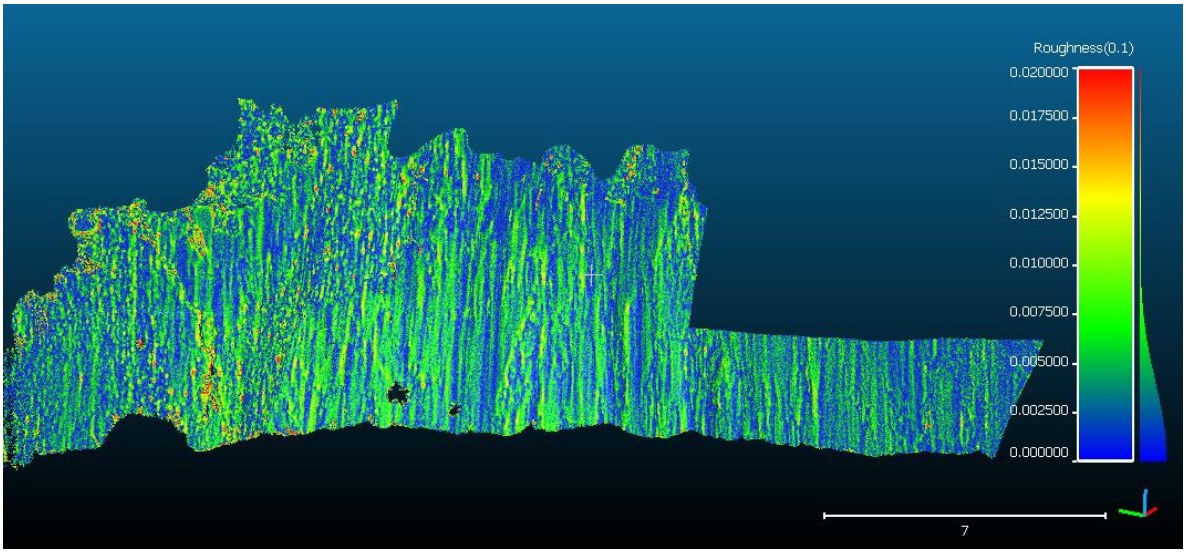

Figure 65. The result of Mean Curvature at kernel size 0.1. The centimeter scale lineaments are made visible, same as the Mean Curvature analysis of the same scale, with some differences in the way they are projected.

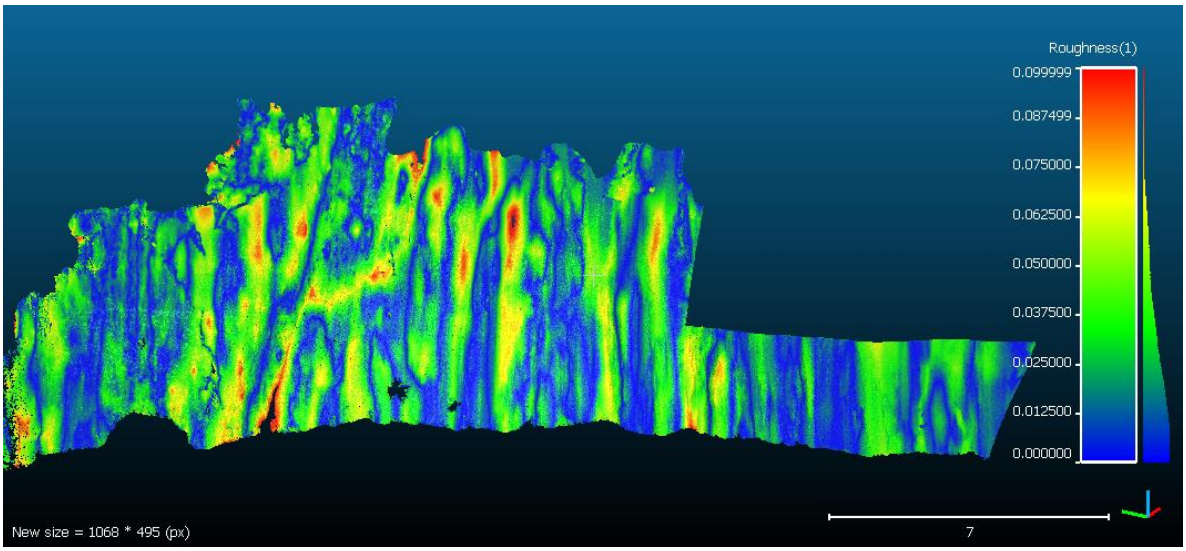

Figure 66. The result of Mean Curvature at kernel size 1. The small scale corrugations of the fault plane are shown here in more detail than with the previous method of Mean Curvature, even though at the same kernel size. The width (0.7m), the density and the orientation of the corrugations are displayed clearly with this method.

Looking at Figure 55 we see a similarity between the results of Polyworks curvature and CloudComapre roughness analysis. This is because they both use a method on the same principles as the triangulation process (when creating a surface), whereas the CloudCompare's curvature analysis at each point is estimated by best fitting a quadric around it (http://www.cloudcompare.org/doc/wiki/index.php5?title=Curvature). However at larger kernel radius the situation in the Roughness Analysis changes and different geometrical structures are becoming visible. Larger kernel radius means that more neighboring points are taken into the equation and larger structures predominate the smaller ones. The resulting image helps us define the corrugation's wavelength and orientation on the Plane surface.

As a last step for the Pidima fault plane, the geological planar facets of the fault surface were computed in order to reveal the Dip and Dip Direction changes across the exposed surface. This method, if used correctly, can give some solid numbers concerning the fault corrugations of the surface and help the researcher better understand the faults overall geometry in both large and small scales. The results of the Dip Direction computation can be displayed in interactive stereograms that allow the user to identify on the model which specific areas have the particular value that interests him.

The method can be used to display a fault plane's Dip and Dip Direction changes in both large and small scale, depending the type of research. This can be done by choosing the

resulting facets size and angular step, dividing the chosen surface in groups of either large or small facets. The fault plane, in our case, was divided in groups of small facets in order to more accurately illustrate the way dip direction changes along its surface.

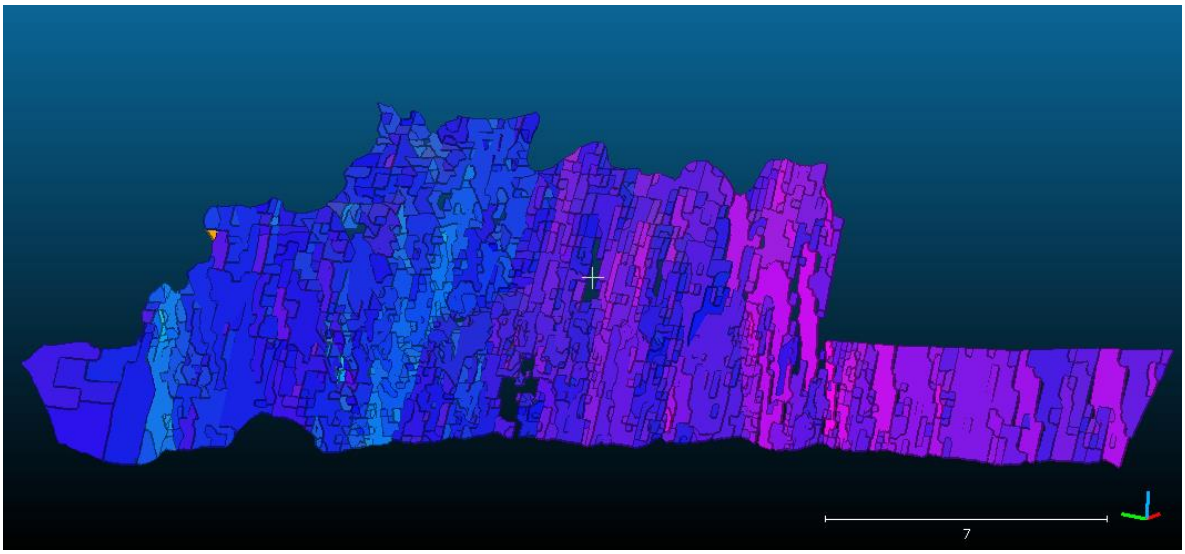

Figure 67. The result of the Geological Planar Facets analysis with an angular step at 5° degrees. The changes in Dip Direction are clearly shown with the change in color of the facets along the fault plane.

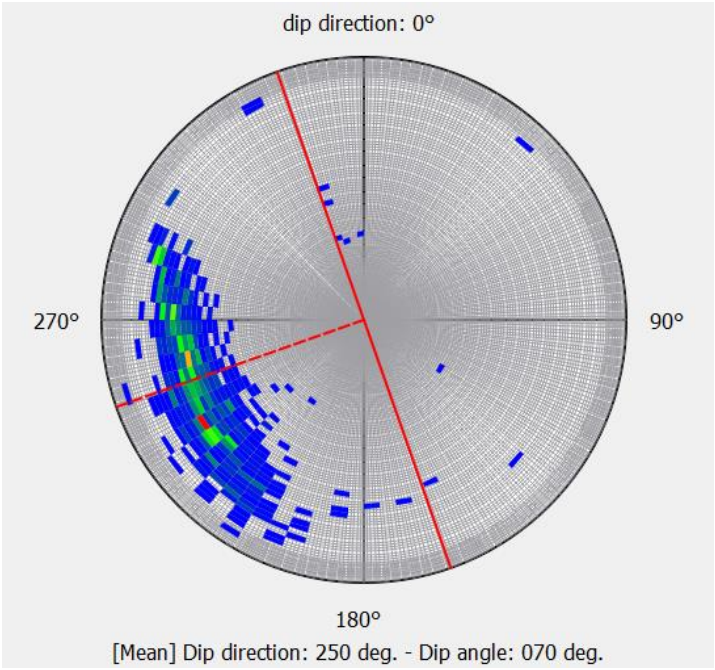

Figure 68. Lower hemisphere sterographic projection of the results of the Facet Analysis demostrated on fig.64. The vast majority of Planar Facets have a Dip Direction between 197° – 294°, giving a mean Dip Direction at 250° and Dip angle at 70°. There are a few facets that differenciate a lot in terms of Dip Direction, possibly produced from varius irregularities from the surface such as plant remains and local erosion or damage. The fault orientation was at 160°.

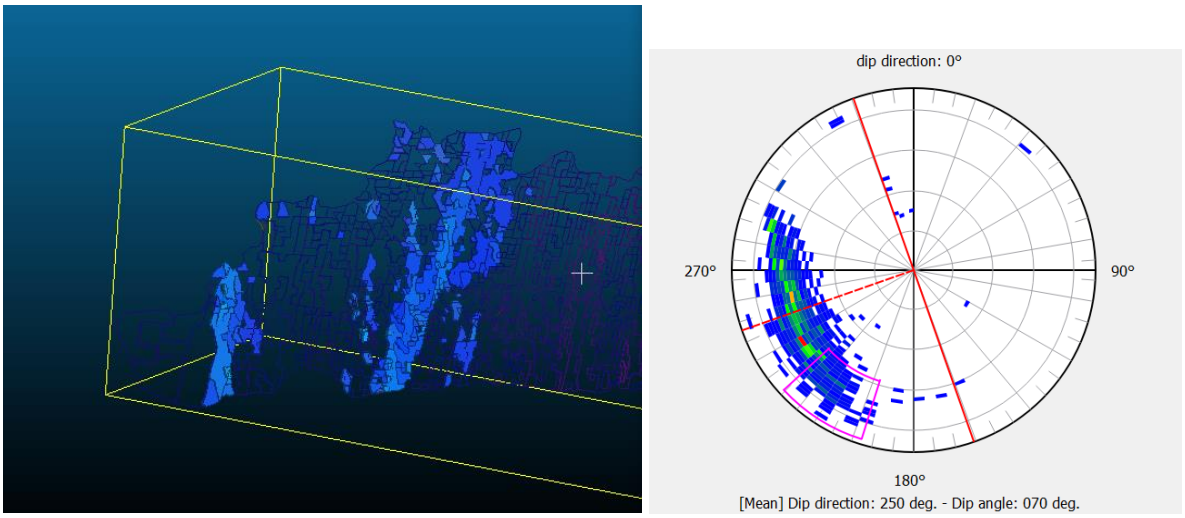

Figure 69. Using the stereogram, the user is able to choose the Facets with values of interest, select them and then isolate them from the others on the fault plane Surface. This can help to easily and quicly identify them and study them seperately if desired.

The results of facet analysis can be exported as a shapefile and imported in any GIS platform, in our case ArcMap version 10.2.2. There, the both Dip angle and Dip Direction can be displayed using different color palettes and categorization along with each facet value shown on the surface. In addition, certain characteristics of the facets that can be useful, are available for the user such as their surface volume and extend.

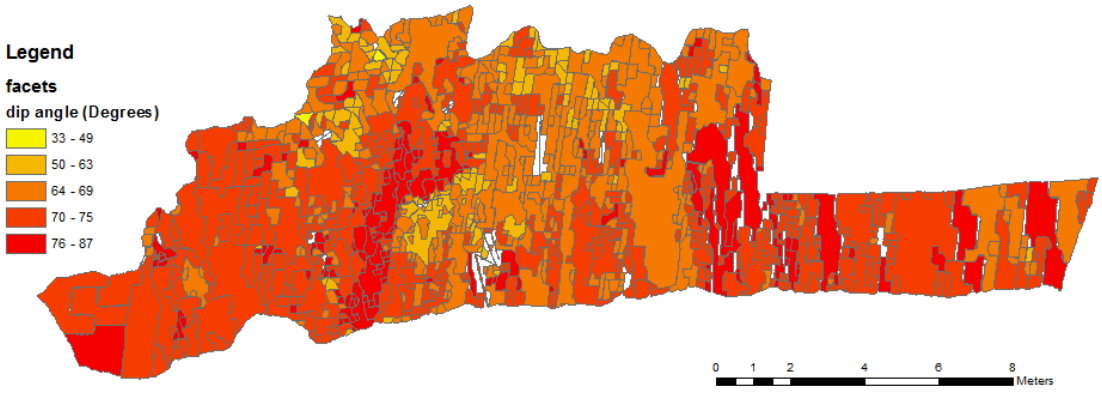

Figure 70. Facet analysis imported in ArcMap displaying Dip angle throughout the fault plane surface. There isnt any value that dominates the exposed surface, but shows that the Dip angle constantly changes throughout the fault plane surface.

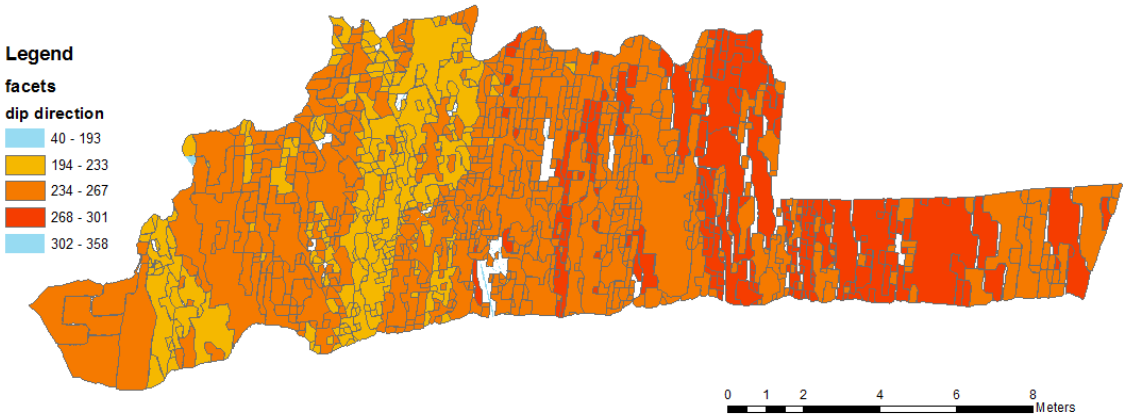

Figure 71. Facet analysis imported in ArcMap displaying Dip Direction throughout the fault plane surface. The values are divided into 3 major categories, the 194°-233°, 234°-267° and 268°-301° The 40°-193° and 302°-358° categories are consisted by sparce facet values, very few in number and with geat deviation from the rest, possible errors from remaining vegetation.

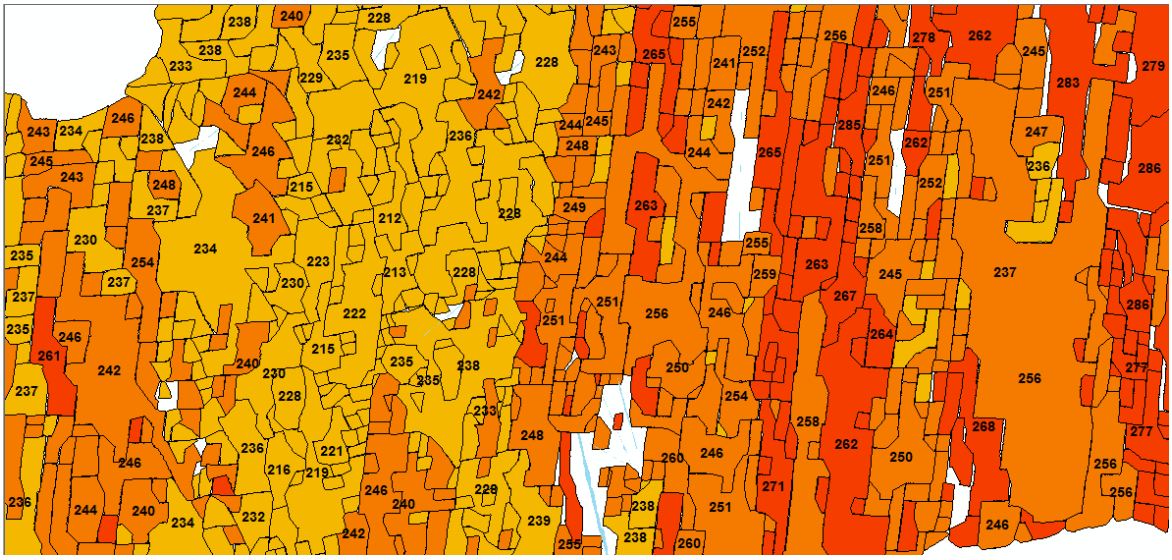

Figure 72. A part of the fault plane illustrating the Dip Direction Change from Fig. 68. The value of each facet is demonstrated for close examination of the surface.

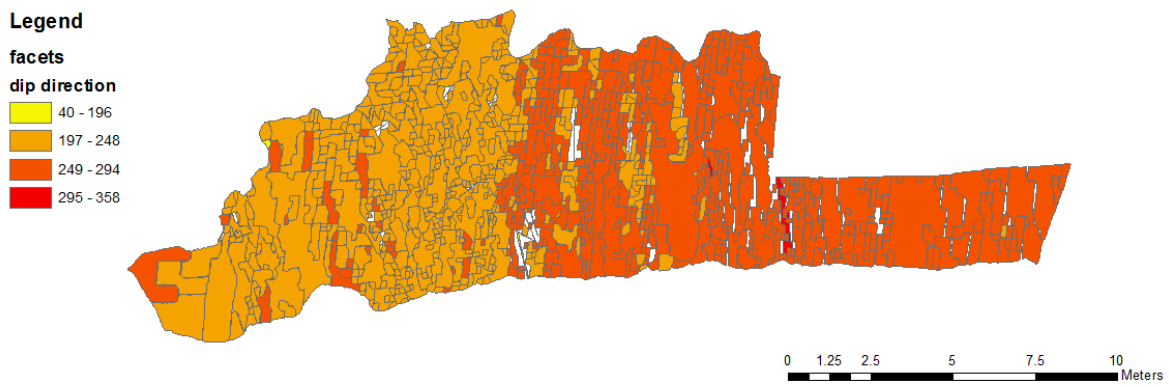

Figure 73. Facet analysis imported in ArcMap displaying Dip Direction throughout the fault plane Surface, with 2 major groups this time, 197°-248° and 249°-294°.

Depending on the categorization made on the facet values, the distribution of areas with similar Dip Direction range can be mapped across the fault plane surface and visualize them along with facet individual values for a complete examination of the results. This method is useful to identify both large and small scale fault plane corrugations, their orientation and Dip Direction, along with their surface volume. The results showed that the huge majority of the Dip Direction distribution on the Pidima fault surface is between values of 197° to 294° degrees. These values were then categorized in 3 classes, to test a small scale distribution (Fig. 71-72), and 2 classes for a larger scale distribution (Fig. 73). In the first case, the plane showed a successive change throughout its surface with the larger values tending to show at the northern part of the fault surface. This is clearly shown with the two classes' characterization where the classes divide the fault surface in two parts, one northern and one southern.

3.4. Petrified Forest of Lesvos Island

3.4.1. Regional Setting

Lesvos is a Greek island situated in the northeastern Aegean Sea with an area of 1,632 square kilometers, making it the third larger island in Greece. The Lesvos Petrified Forest Geopark is located in the western part of the island and is comprised of large accumulations of fossilized tree trunks. Lesvos Petrified Forest consists of four major terrestrial and marine

fossil sites lying on an area of 15,000 hectares with a buffer zone of 20,000 hectares (*Zouros*, 2010). The formation of the Petrified Forest is directly related to the intense volcanic activity in Lesvos during Late Oligocene to Lower-Middle Miocene. The largest concentration of petrified trees is within the park at "Bali Alonia". The fossilized trees are silicified remnants of a sub-tropical forest that used to cover the area that is the N-W part of the island today, 20-15 million years ago (Velitzelos and Zouros, 1998).

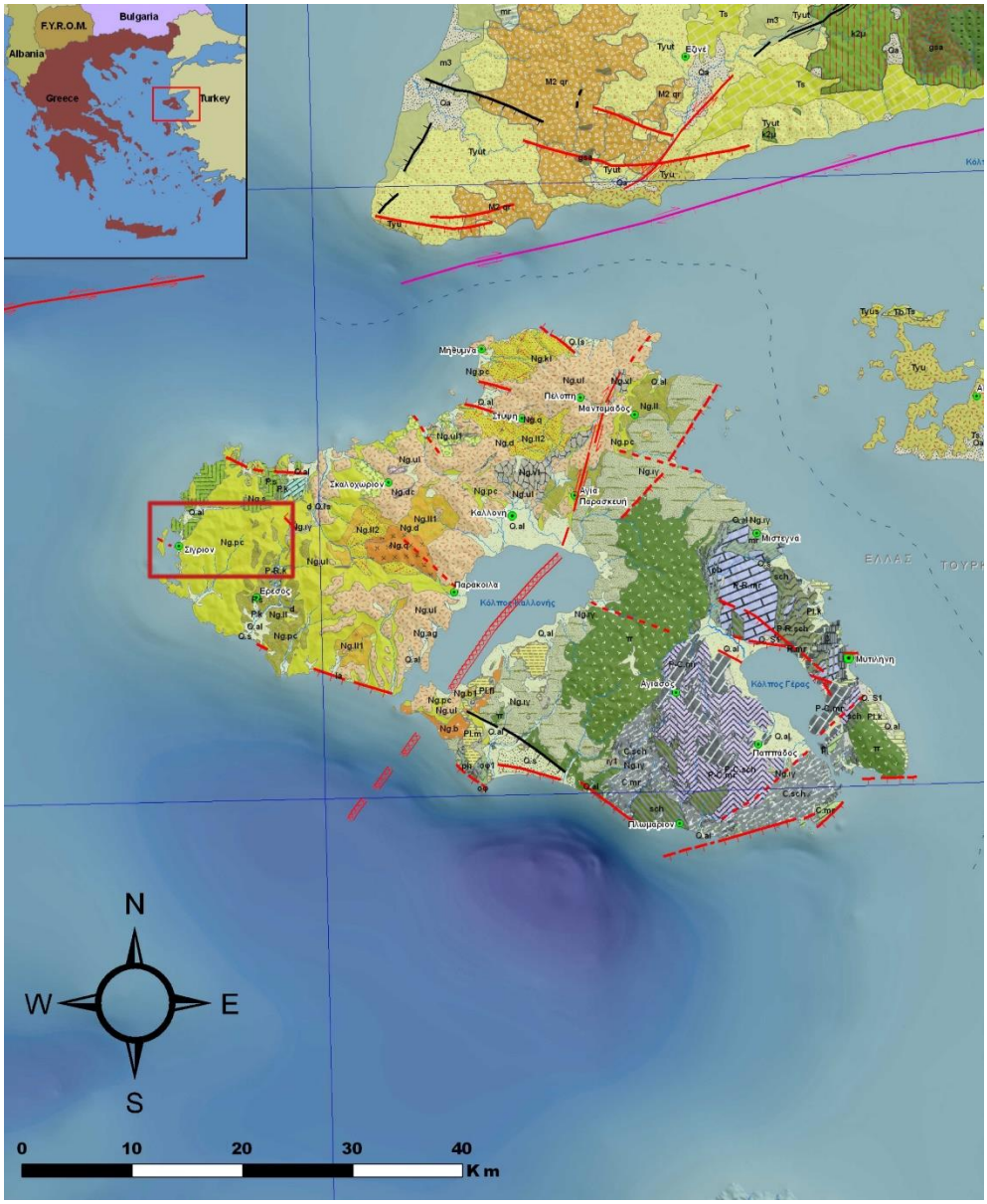

Figure 74. Geological Map of Lesvos with the study area in Petrified Forest Geopark delimited by the red rectangle. (Modified from (Delogkos, 2009)

Lesvos Island bedrock is most probably part of the pelagonian geotectonic zone (Mountrakis, 2010) and mainly consists of an autochthonous Permo-Triassic unit and ophiolithic nappes. The Permo-Triassic unit is comprised of schists, quartzites, metasandstones, phyllites and intercalations of marbles and crystalline carbonates. These rocks are primarily spread on the south-east part of the island with a few appearances in the north-west (Velitzelos and Zouros, 1998). The ophiolithic nappes consist of basic and ultrabasic rocks along with associated deep-sea fine-grained sediments. The nappes also include metamorphic rocks such as amphibolites, amphibole schists, metabasites and metasediments, parts of the tectonic sole that are overthrusted the metamorphic basement (Velitzelos and Zouros, 1998).

Lesvos is part of a late Oligocene -middle Miocene calc-alcaline to shoshonitic volcanic belt, placed in the northern and central Aegean Sea as well as western Anatolia. The central part of the island is home to a series of stratovolcanoes, situated along a SW-NE direction, i.e. Lepetymnos, Vatoussa and Agra calderas. Due to that fact, the area along with the western part of the island is dominated by volcanic rocks, comprised of andesites, dacites, rhyolites, ingnimbrites, pyroclastics, tuffs and volcanic ash. The fossilized tree trunks of the Petrified Forest occur within the thick pyloclastic sequence of Sigri. This formation consists of several horizons of pyroclastic flows, mainly comprised of pumice flows, mud flows, debris flows and stream conglomerates intercalated with air fall pyroclastic deposits. Identified among them are several siliceous paleosol horizons (Zouros *et al*., 2007).

The Geopark's tree trunks, branches, and leaves were covered rapidly from volcanic materials that were enriched afterwards with silica rich solutions, which led to their isolation from atmospheric conditions. These favorable fossilization conditions made the fossilization process was near perfect, which is very helpful as the study of the fossil tree trunks, leaves and seeds provides useful data about the palaeoflora, climate and relative age of the Lesvos Petrified Forest (Zouros *et al*., 2007).

3.4.2. Methodology

3.4.2.1. Data Acquisition

The scanning process took place during the October of 2014 at the surrounding area of the Lesvos island Petrified Forest Geopark. The target of the expedition was to obtain 3D representations of fossilized tree trunks and fault outcrops in order to create accurate 3D models of them for further studies. For this Thesis one well preserved tree trunk and a few others in a bit worse condition, as well as two slopes containing tree trunks and fault indications were illustrated as 3D models. In total 97,739,365 (97.7 million) points were collected of this particular site, divided in nine different scans consisting different angles of the same target. The actual number of the scanning targets is much bigger, but the rest of them were not used in the framework of this study.

Figure 75. Tree trunk in the Sigri area, with its roots preserved.

Figure 76. Tree trunk in the Sigri area. Its location didn't allow closer scanning from a better angle.

Figure 77. Road cut in Vrisaki area containing several faults.

3.4.2.2. Data Processing

The scans were first imported in Polyworks for the necessary editing and the alignment of the scans together in a single point cloud. The 3D models were then subsampled and exported to CloudCompare.

The most well preserved tree trunk, from the available data, was consisted of 21,101,500 (21 million) points but subsampled to 1,856,436 points and was named Lesvos_fy. The merged 3D model, as seen on Fig. 75, consisted from 3 point clouds of different point densities, different scanning angles and light shading, resulting in a heterogeneous model. For that reason, the merged point cloud was considered necessary to be meshed. Because Polyworks was unable to create a polygonal model out of the merged point cloud, the 3D model was imported in CloudCompare for a Poisson surface

reconstruction. The process was made via the plug-in qPoissonRecon which is based on triangular mesh generation algorithm proposed by Misha Kazhdan of Johns Hopkins University (Kazdam, 2005).

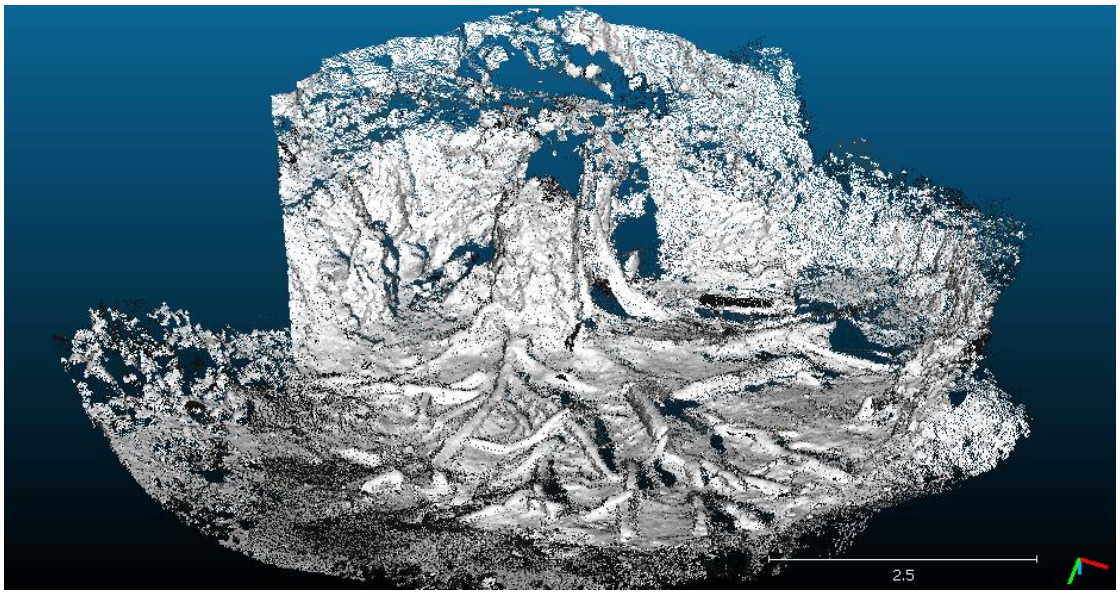

Figure 78. The Sigri Fossilized tree trunk, Lesvos_fy, as a single point cloud with the surface normals computed. The scans had many differences in the way they were taken which resulted in different point cloud densities, creating visual differences between them.

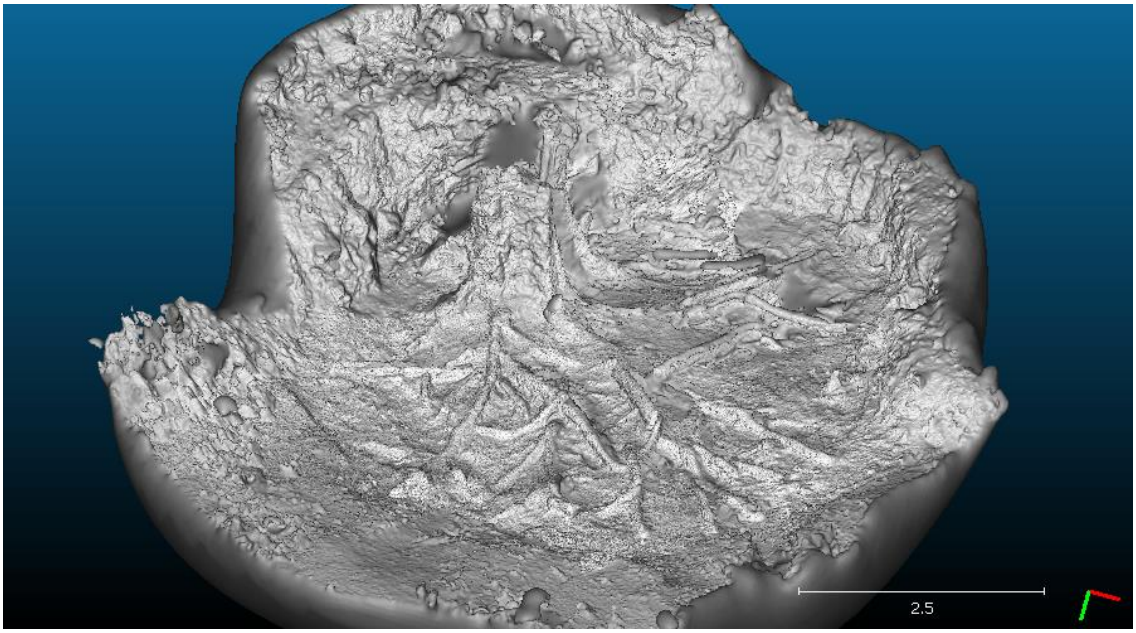

Figure 79. The Sigri Fossilized tree trunk, Lesvos_fy, meshed with Poisson surface reconstruction in order to eliminate the point density variations.

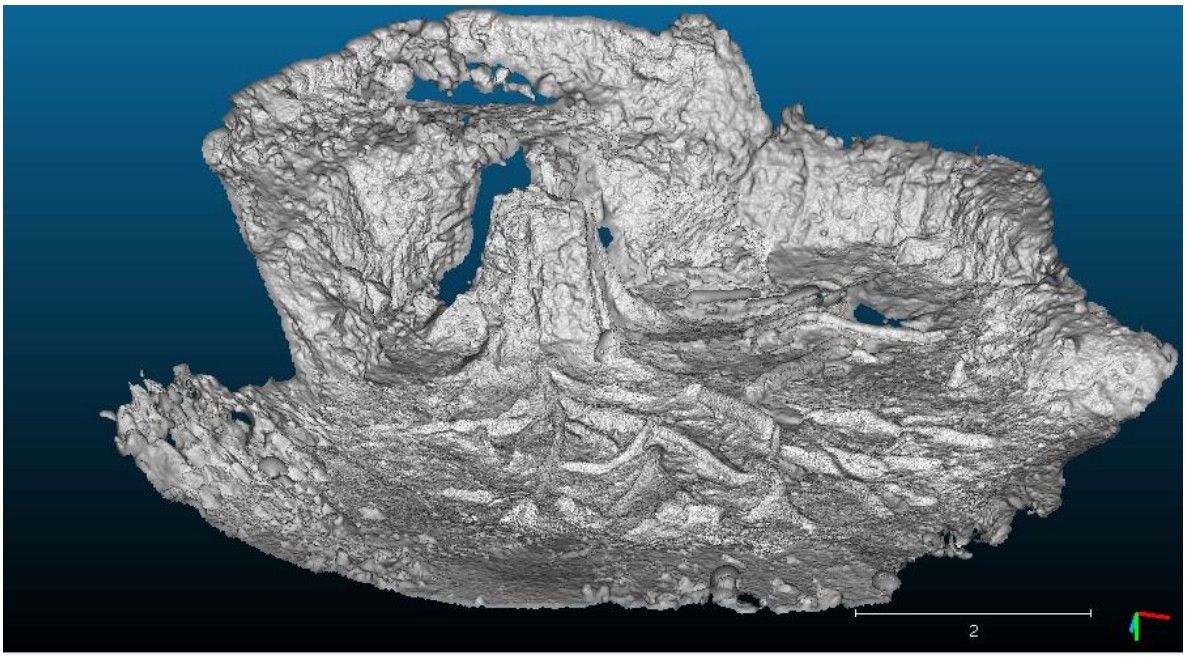

Figure 80. The Sigri Fossilized tree trunk, Lesvos_fy, meshed with Poisson surface reconstruction.

Another two tree trunks were also individually scanned, but were not very well preserved, named Lesvos_tx and Lesvos_MPY. Lesvos_tx was consisted by two scans of total 73,637,578 and was subsampled to 368,373 points, whereas Lesvos_MPY consisted of one scan containing 579,469 points.

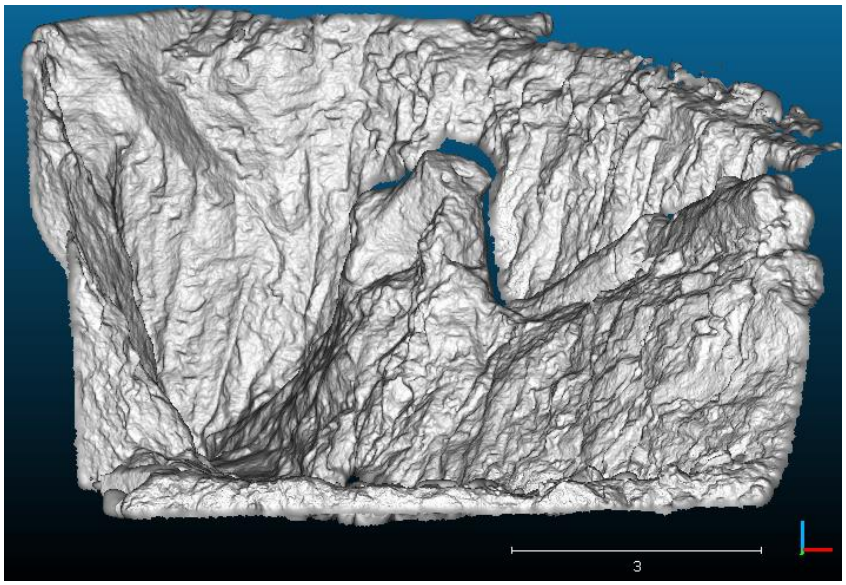

Figure 81. The Sigri Fossilized tree trunk, Lesvos_tx, meshed with Poisson surface reconstruction.

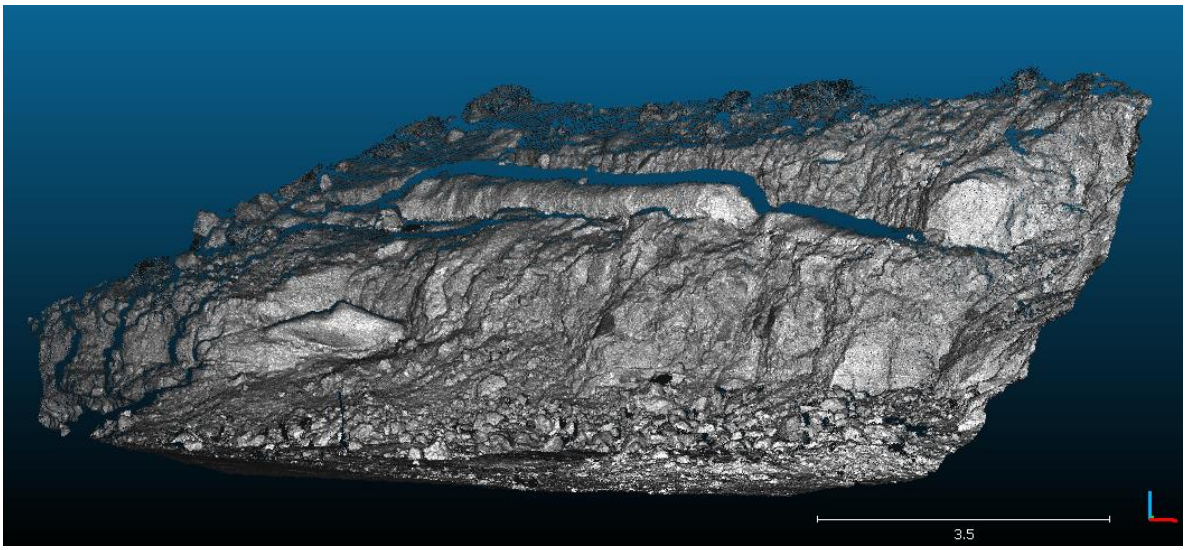

Figure 82. Point cloud of Lesvos_MPY with its surface normals computed.

Apart from the tree trunks, in the same area, two road cuts were also scanned in the Vrisaki area containing fault indications that were not visible at the 3D models due to both the area conditions and the scanner settings at that time. The two slopes named Lesvos_Vrisaki and Lesvos_BRY, consisted of 1,005,995, subsampled to 13,666,434, and 1,041,416, subsampled to 9,835,353, points respectively.

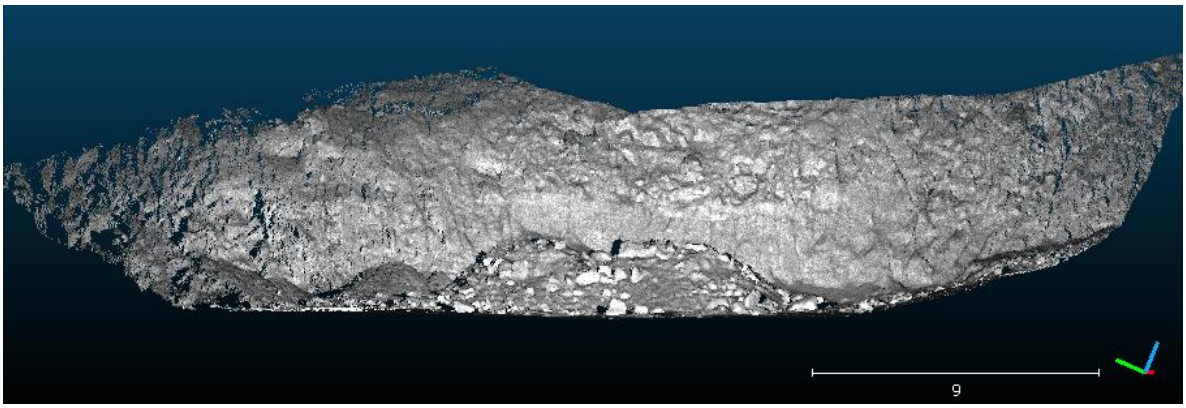

Figure 83. Point cloud of Lesvos_Vrisaki with surface Normals computed and the greyscale of intensity values.

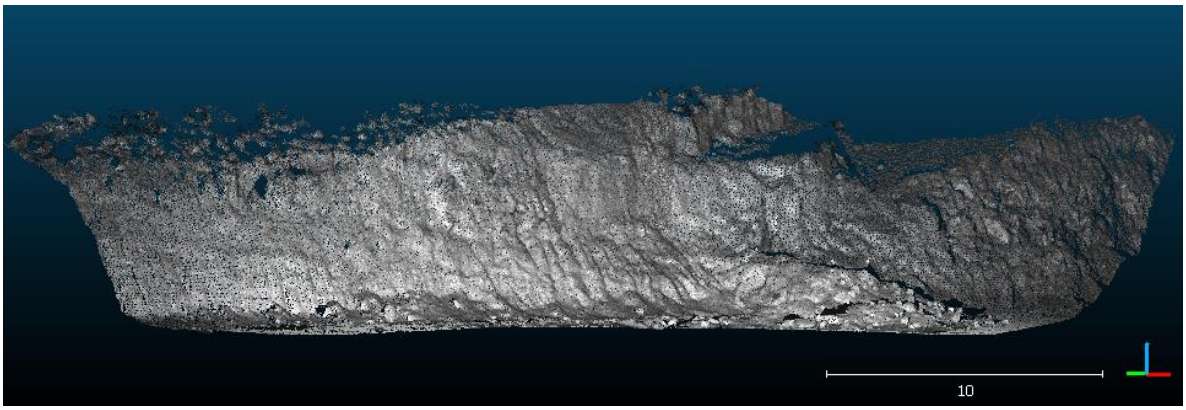

Figure 84.Point cloud of Lesvos_BRY with surface normals computed and the greyscale of intensity values.

The work done in Lesvos was limited in just creating 3D models as there wasn't much tectonic interest in the resulting models. Different methods of creating 3D models were tested such as point cloud with computed normals or intensity values and the Poisson surface reconstruction. Both create good representations of the original target depending on the situation and the data available. The Poisson surface reconstruction proved to be a very useful tool when having to deal with two or more merged point clouds with different point densities and data quality as it eliminates the differences and creates a more accurate representation.

4. Conclusions

4.1. Discussion of Results and future work

During the process of this Thesis, many different methods were tested, both in point cloud editing and structural geology, with some of them giving very interesting results. The knowledge on these matters at the beginning of this Thesis was very narrow and fragmentary, so the main purpose was to develop a methodology for point cloud data, focused mainly on structural geology analyses.

The Stavrakia fault point data produced results concerning structural analysis, especially in geomorphology. The terrestrial's laser scanner ability to acquire high density point cloud, which in turn helped to create a precise DEM, is by itself a major boost in geomorphological analysis, especially in fault escarpments. The combination with point

classification methods, even though it is at an early stage, helped increase the accuracy of the geomorphology results significantly. This came with some interesting results of the Stavrakia fault, of which detailed cross-sections were made, and its escarpment's morphology was analyzed intensively throughout the surveyed part. The results, however, need further testing and with new publications every year on this subject, the method has a lot of potential for further development in morphotectonic analysis. Moreover, georeferencing the data would definitely improve the current method by far and even allow the data to be combined and with other point cloud and DEM data of the same area. This can be achieved with the combined use of TLS and Global Navigation Satellite Systems (GNSS) data.

The survey of the palaeoseismological trench in Tyrnavos town offered a high density point cloud of a fault plane with millimeter accuracy. The 3D model could display even the smallest morphological anomalies of the plane surface creating a very close to real life representation of the fault plane. The analysis of maximum curvature revealed a zone of low values that requires further investigation. The nature of the fault plane, as well as its limited spatial dimensions, did not allow for any other method applied to give solid results and thus was deemed necessary to further investigate the data when more knowledge on the subject has been gained.

Gyrtoni escarpment was surveyed concurrently with the Tyrnavos palaeoseismological trench with the hope that a precise DEM could help the investigation of this fault. The area was used for agricultural activities and the fault escarpment was of small height that did not exceed 12m. As there were not any methods that could be used with the surveyed data, a more extensive research for further data acquisition of the Gyrtoni escarpment is required. More survey of the area with the terrestrial laser scanner along with other methods of acquiring point cloud data of the area (eg. By using Unmanned Aerial Vehicle/UAV imagery) would improve greatly the results of a geomorphological analysis in the future.

The Pidima area is of great geological interest due to the area's tectonic structure and any additional data would be of significant importance. Even though the 3D model of the palaeoseismological trench was only an excellent demonstration of point cloud classification, the fault plane gave many useful and interesting results. Technical reasons did not allow a complete data acquisition of the entire fault plane outcrop but the point cloud analyses were

able to successfully complete. The structural analysis of the fault plane allowed for a detailed logging of its geometrical characteristics, such as the plane's dip and dip direction angles, lineament and corrugation size and disposition. For more conclusive results a complete survey of the fault plane is required with the addition of field data for confirmation and comparison of the results. It is important to mention that a digital image integration in both point clouds would improve the analyzing methods immensely and even allow for more advance methodologies.

Finally, Lesvos scan data was mainly of petrified tree trunks and therefore were used only for methods concerning the creation 3D models. They proved very useful in testing different techniques in order to improve both the accuracy of the representation as well as, visual quality. The 3D models enhanced with color from images would be able to represent very accurately the physical target.

4.2. Concluding remarks

1) The Stavrakia fault escarpment has slope angles mostly ranging from 35°- 40° with the largest part of the slope most of the time representing the stable-debris slope. From the scatter diagrams, it can be deducted that the fault escarpment displays a predominant slope angle of 35°- 40° (average at 36.8° and maximum angle average at 43.5°) for a height that ranges from 50m-100m (average 63.33m).

2) Tyrnavos palaeoseismological trench fault plane allowed the creation of a very accurate and detailed 3D model. The analysis of maximum curvature revealed a zone of low values that requires further investigation. The reason for that was its small spatial dimensions and the absence of a clear surface structure.

3) A detailed visual representation of the Gyrtoni escarpment was created and its maximum height from its base was calculated at 12m with a slope angle of 8°. The low height and angle values were due to the scan angle and the human activities in the area.

4) The Pidima palaeoseismological trench 3D model was able to provide a good visual representation of the target improved greatly by the intensity values. The point classification method was able to effectively clean and edit the point cloud.

5) The Pidima fault plane has an NNW-SSE trend (160°) with a mean dip direction at 250° and dip angle at 70°. The fault plane surface was able to provide information about the geometrical properties of the fault, such as the dip direction and dip angle change throughout its whole surveyed surface. Gaussian curvature identified areas of high surface irregularities and mean curvature offered information about the surfaces lineament and corrugation orientation, with corrugations displaying a width of 75cm. The roughness of the plane's surface revealed an arc of a smoother area upon the plane and a corrugation width of 70cm. The origin of the three arc shaped zones of low roughness values require further investigation.

ABSTRACT

An extensive research was made on LIDAR and Terrestrial Laser Scanner (TLS) applications on Geosciences and various point cloud editing methodologies were tested and applied. The methods were applied on data surveyed during the years 2014 and 2015, in the areas of Stavrakia (Crete), Tyrnavos and Gyrtoni (Thessaly), Pidima (Messinia) and Petrified forest of Lesvos. The Stavrakia fault escarpment point data produced results concerning structural analysis and geomorphology. Detailed cross-sections were made, and its escarpment's morphology was analyzed intensively throughout the surveyed part. The survey of the palaeoseismological trench in Tyrnavos town offered a high density point cloud of a fault plane with millimeter accuracy. The 3D model could display even the smallest morphological anomalies of the plane surface creating a very close to real life representation of the fault plane. The analysis of maximum curvature revealed a zone of low values that requires further investigation. A detailed visual representation of the Gyrtoni escarpment was created and its maximum height from its base was calculated. In the Pidima area, the palaeoseismological trench 3D model was able to provide a good visual representation of the target improved greatly by the intensity values. The point classification method was able to effectively clean and edit the point cloud. The structural analysis of the fault plane allowed for a detailed logging of its geometrical characteristics, such as the plane's dip and dip direction angles, lineament and corrugation size and disposition. Finally, Lesvos scan data was mainly of petrified tree trunks and therefore were used only for methods concerning the creation 3D models. They proved very useful in testing different techniques in order to improve both the accuracy of the representation as well as, visual quality.

Περίληψη

Εκτενής βιβλιογραφική έρευνα έγινε πάνω στα συστήματα LIDAR και τους επίγειους σαρωτές laser (TLS) και τις εφαρμογές τους στις γεωεπιστήμες, καθώς και για μεθόδους επεξεργασίας και ανάλυσης νέφους σημείων. Η εφαρμογή των μεθόδων έγινε σε δεδομένα που συλλέχθηκαν τα έτη 2014 και 2015 τις περιοχές των Σταυρακίων (Κρήτη), Τυρνάβου και Γυρτώνης (Θεσσαλία), Πηδήματος (Μεσσηνία) και του Απολιθωμένου δάσους της Λέσβου. Τα τρισδιάστατα μοντέλα του ρηξιγενούς πρανούς στα Σταυράκια, έδωσαν πολλά στοιχεία για τη γεωμορφολογία του πρανούς και για το χαρακτηρισμό του ως προς τις μορφοτεκτονικές του ιδιότητες, μέσω μορφολογικών τομών που έγιναν κάθετα, κατά μήκος του πρανούς. Η σάρωση της κατοπτρικής επιφάνειας στην παλαιοσεισμολογική τομή του Τυρνάβου πρόσφερε μια λεπτομερή τρισδιάστατη απεικόνιση της με ακρίβεια χιλιοστού. Υπολογίστηκαν τα μορφολογικά στοιχεία και η μέγιστη καμπυλότητα της επιφάνειας, όπου και αποκάλυψαν δομές που χρήζουν περισσότερης διερεύνησης. Η τρισδιάστατη αναπαράσταση της μορφολογίας του ρηξιγενούς πρανούς της Γυρτώνης έδωσε στοιχεία για το ύψος και τη κλίση του πρανούς που θα ήταν πολύ δύσκολο να αποκτηθούν με άλλες μεθόδους. Στην περιοχή του Πηδήματος, η παλαιοσεισμολογική τομή απεικονίσθηκε με μεγάλη ευκρίνεια και σε συνδυασμό με τις τιμές ανακλαστικότητας του φωτός των υλικών που την αποτελούν. Η τομή επεξεργάστηκε γρήγορα και αποτελεσματικά με αυτοματοποιημένες μεθόδους. Η κατοπτρική επιφάνια απεικονίσθηκε και αυτή με τις τιμές της ανακλαστικότητας και εξετάστηκαν οι γεωμετρικές ιδιότητες της, ως προς διάφορες τιμές της καμπυλότητας, τραχύτητας, προσανατολισμού και κλίσης της. Τέλος, από το Απολιθωμένο δάσος της Λέσβου, δημιουργήθηκε μια σειρά τρισδιάστατων μοντέλων πάνω σε απολιθωμένους κορμούς δέντρων και τομές δρόμων με σκοπό τη ολοκληρωμένη απεικόνισή τους για σκοπούς του γεωπάρκου.

5. References

Bergbauer, S., Pollard, D.D., 2003. How to calculate normal curvatures of sampled geological surfaces. J. Struct. Geol. 25, 277–289. doi:10.1016/S0191-8141(02)00019-6

Brodu, N., Lague, D., 2012. 3D terrestrial lidar data classification of complex natural scenes using a multi-scale dimensionality criterion: Applications in geomorphology. ISPRS J. Photogramm. Remote Sens. 68, 121–134. doi:10.1016/j.isprsjprs.2012.01.006

Bubeck, A., Wilkinson, M., Roberts, G.P., Cowie, P.A., McCaffrey, K.J.W., Phillips, R., Sammonds, P., 2015. The tectonic geomorphology of bedrock scarps on active normal faults in the Italian Apennines mapped using combined ground penetrating radar and terrestrial laser scanning. Geomorphology, Geomorphology of Active Faulting and seismic hazard assessment: New tools and future challenges 237, 38–51. doi:10.1016/j.geomorph.2014.03.011

Buckley, S., Vallet, J., Braathen, A., Wheeler, W., 2008. OBLIQUE HELICOPTER-BASED LASER SCANNING FOR DIGITAL TERRAIN MODELLING AND VISUALISATION OF GEOLOGICAL OUTCROPS. Int. Arch. Photogramm. Remote Sens. Spat. Inf. Sci. 37(Part B4).

Bucknam, R.C., Anderson, R.E., 1979. Estimation of fault-scarp ages from a scarp-height–slope-angle relationship. Geology 7, 11–14. doi:10.1130/0091-7613(1979)7<11:EOFAFA>2.0.CO;2

Caputo, R., 1995. Inference of a seismic gap from geological data: Thessaly (Central Greece) as a case study. Ann. Geophys. 38. doi:10.4401/ag-4127

Caputo, R., Catalano, S., Monaco, C., Romagnoli, G., Tortorici, G., Tortorici, L., 2010. Active faulting on the island of Crete (Greece). Geophys. J. Int. 183, 111–126. doi:10.1111/j.1365-246X.2010.04749.x

Caputo, R., Helly, B., Pavlides, S., Papadopoulos, G., 2006. Archaeo- and palaeoseismological investigations in Northern Thessaly (Greece): Insights for the seismic potential of the region. Nat. Hazards 39, 195–212. doi:10.1007/s11069-006-0023-9

Caputo, R., Helly, B., Pavlides, S., Papadopoulos, G., 2004. Palaeoseismological investigation of the Tyrnavos Fault (Thessaly, Central Greece). Tectonophysics 394, 1–20. doi:10.1016/j.tecto.2004.07.047

Caputo, R., Pavlides, S., 1993. Late Cainozoic geodynamic evolution of Thessaly and surroundings (central-northern Greece). Tectonophysics 223, 339–362. doi:10.1016/0040-1951(93)90144-9

Caputo, R., Piscitelli, S., Oliveto, A., Rizzo, E., Lapenna, V., 2003. The use of electrical resistivity tomographies in active tectonics: examples from the Tyrnavos Basin, Greece. J. Geodyn., Active Faults: Analysis, Processes and Monitoring 36, 19–35. doi:10.1016/S0264-3707(03)00036-X

Chatzipetros, A., 1998. Paleoseismological and morphotectonic study of the active fault systems at Mygdonia basin, eastern Chalkidiki and Kozani-Grevena.

Chatzipetros, A., Michailidou, A., Tsapanos, Th.M., Pavlides, S., 2005. Μορφοτεκτονική - σεισμοτεκτονική μελέτη των ρηγμάτων Στρατωνίου - Βαρβάρας και Γοματίου - Μεγάλης Παναγίας (Ανατολική Χαλκιδική) = Morphotectonics and seismotectonics of th Stratoni - Barbara and Gomati - Megali Panagia active fault (Eastern Chalkidiki, N. Δελτίον Της Ελληνικής Γεωλογικής Εταιρίας 37, 127–142.

Delibasis, N., Ziazia, M., Voulgaris, N., Papadopoulos, T., Stavrakakis, G., Papanastassiou, D., Drakatos, G., 1999. Microseismic activity and seismotectonics of Heraklion Area (central Crete Island, Greece). Tectonophysics 308, 237–248. doi:10.1016/S0040-1951(99)00076-1

Delogkos, E., 2009. Χαρτης Γεωλογίας και ενεργών ρηγμάτων νήσου Λέσβου.

Dewez, T.J.B., Girardeau-Montaut, D., Allanic, C., Rohmer, J., 2016. FACETS : A CLOUDCOMPARE PLUGIN TO EXTRACT GEOLOGICAL PLANES FROM UNSTRUCTURED 3D POINT CLOUDS. ISPRS - Int. Arch. Photogramm. Remote Sens. Spat. Inf. Sci. XLI-B5, 799–804. doi:10.5194/isprs-archives-XLI-B5-799-2016

Enge, H.D., Buckley, S.J., Rotevatn, A., Howell, J.A., 2007. From outcrop to reservoir simulation model: Workflow and procedures. Geosphere 3, 469–490. doi:10.1130/GES00099.1

Fassoulas, C., 2001. The tectonic development of a Neogene basin at the leading edge of the active European margin: the Heraklion basin, Crete, Greece. J. Geodyn. 31, 49–70. doi:10.1016/S0264-3707(00)00017-X

Fassoulas, C., Καγιώργη, M., Νικολακάκης, M., 2010. Morphotectonic analysis of Stavrakia fault scarp with emphasis on seismicrisk assessment, Heraklion, Crete, Greece. Επιστημονική Επετηρίδα Του Τμήματος Γεωλογίας ΑΠΘ 39, 111.

Fountoulis, I., Mariolakos, I., Ladas, I., 2014. Quaternary basin sedimentation and geodynamics in SW Peloponnese (Greece) and late stage uplift of Taygetos Mt.

Fowler, A., France, J., Truong, O., 2011. Applications of advanced laser scanning technology in geology.

Ganas, A., Palyvos, N., Mavrikas, G., Kollias, S., Tsimi, C., 2010. GEOMORPHOLOGICAL AND GEOLOGICAL OBSERVATIONS AT THE COAST OF TRIPITI HILL (HERAKLION HARBOUR, CRETE), IN RELATION TO REPORTED ACTIVE FAULTING. Proc. XIX CBGA Congr., Scientific Annals 99 special, 11–20.

García-Sellés, D., Falivene, O., Arbués, P., Gratacos, O., Tavani, S., Muñoz, J.A., 2011. Supervised identification and reconstruction of near-planar geological surfaces from terrestrial laser scanning. Comput. Geosci. 37, 1584–1594. doi:10.1016/j.cageo.2011.03.007

Hancock, P.L., Barka, A.A., 1987. Shear Criteria in Rocks Kinematic indicators on active normal faults in Western Turkey. J. Struct. Geol. 9, 573–584. doi:10.1016/0191-8141(87)90142-8

Hodgetts, D., 2013. Laser scanning and digital outcrop geology in the petroleum industry: A review. Mar. Pet. Geol. 46, 335–354. doi:10.1016/j.marpetgeo.2013.02.014

Hu, H., Fernandez-Steeger, T.M., Dong, M., Azzam, R., 2012. Numerical modeling of LiDAR-based geological model for landslide analysis. Autom. Constr. 24, 184–193. doi:10.1016/j.autcon.2012.03.001

Jones, R.R., Kokkalas, S., McCaffrey, K.J.W., 2009. Quantitative analysis and visualization of nonplanar fault surfaces using terrestrial laser scanning (LIDAR)—The Arkitsa fault, central Greece, as a case study. Geosphere 5, 465–482. doi:10.1130/GES00216.1

Jones, R.R., Mccaffrey, K.J.W., Imber, J., Wightman, R., Smith, S.A.F., Holdsworth, R.E., Clegg, P., Paola, N.D., Healy, D., Wilson, R.W., 2008. Calibration and validation of reservoir models: the importance of high resolution, quantitative outcrop analogues. Geol. Soc. Lond. Spec. Publ. 309, 87–98. doi:10.1144/SP309.7

Kazdam, M., 2005. Reconstruction of Solid Models from Oriented Point Sets.

Kokinou, E., Skilodimou, D., Bathrellos, D., 2013. MORPHOTECTONIC ANALYSIS OF HERAKLION BASIN (CRETE, GREECE). Bull. Geol. Soc. Greece XLVII 2013, 285–294.

Kondo, H., Toda, S., Okumura, K., Takada, K., Chiba, T., 2008. A fault scarp in an urban area identified by LiDAR survey: A Case study on the Itoigawa–Shizuoka Tectonic Line, central Japan. Geomorphology 101, 731–739. doi:10.1016/j.geomorph.2008.02.012

Koukouvelas, I., Kremastas, E., Tsodoulos, I., Pavlides, S., Chatzipetros, A., Valkaniotis, S., Papathanassiou, G., Caputo, R., 2013. New insights from palaeoseismological trench across the Grytoni Fault (Central Greece). Comparison with other Aegean active faults. Geophys. Res. Abstr., EGU General Assembly 2013 15.

Mariolakos, I., Spyridonos, E., 2010. Remarks on the karstification in the wider area of the Upper Messinia closed hydrogeological basin (SW Peloponnesus, Greece). Δελτίον Της Ελληνικής Γεωλογικής Εταιρίας 43, 1785–1791.

Mountrakis, D.M., 2010. Geology of Greece.

Oliveto, A., Mucciarelli, M., Caputo, R., 2004. HVSR prospecting in multi-layered environments: An example from the Tyrnavos Basin (Greece). J. Seismol. 8, 395–406. doi:10.1023/B:JOSE.0000038452.12593.6f

Pavlides, S., Caputo, R., 2004. Magnitude versus faults' surface parameters: quantitative relationships from the Aegean Region. Tectonophysics, Active Faults of the Eastern Hemisphere 380, 159–188. doi:10.1016/j.tecto.2003.09.019

Pavlides, S., Caputo, R., Koukouvelas, I., Kokkalas, S., Chatzipetros, A., 2006. Paleoseismological investigations of Aegean-type active faults in mainland Greece and their implications. Geol. Soc. Am. Spec. Pap. 409, 175–188. doi:10.1130/2006.2409(10)

Rosser, N.J., Petley, D.N., Lim, M., Dunning, S.A., Allison, R.J., 2005. Terrestrial laser scanning for monitoring the process of hard rock coastal cliff erosion. Q. J. Eng. Geol. Hydrogeol. 38, 363–375. doi:10.1144/1470-9236/05-008

Sagy, A., Brodsky, E.E., Axen, G.J., 2007. Evolution of fault-surface roughness with slip. Geology 35, 283–286. doi:10.1130/G23235A.1

Sboras, S., Ganas, A., Pavlides, S., 2010. Morphotectonic analysis of the neotectonic and active faults of Beotia (Central Greece), using G.I.S. techniques. Δελτίον Της Ελληνικής Γεωλογικής Εταιρίας 43, 1607–1618.

Schmid, K., Waters, K., Dingerson, L., Hadley, B., Mataosky, R., Carter, J., Dare, J., 2012. Lidar 101: An introduction to lidar technology, data and applications.

Schumann, A., Arndt, D., Wiatr, T., Götz, A.E., Hoppe, A., 2011. High-resolution terrestrial laser scanning and 3D modelling of a mineral deposit for extraction management optimisation [Hochauflösendes Terrestrisches Laserscanning und 3D-Modellierung einer Kalklagerstätte zur Optimierung des Abbaumanagements]. Z. Dtsch. Ges. Für Geowiss. 162, 435–442. doi:10.1127/1860-1804/2011/0162-0435

Souza, M.K., Veronez, M.R., Tongoli, F.M.W., Silvera Jr., L.G., Inocencio, L.C., Silva, R.M., Modena, R.C.C., 2013. Terrestrial Laser Scanning Application for Measuring of Structures Information in Geological Outcrops. Int. J. Adv. Remote Sens. GIS 2, 260–270.

Tsodoulos, I.M., Koukouvelas, I.K., Pavlides, S., 2008. Tectonic geomorphology of the easternmost extension of the Gulf of Corinth (Beotia, Central Greece). Tectonophysics, Earthquake Geology: Methods and Applications 453, 211–232. doi:10.1016/j.tecto.2007.06.015

Tsodoulos, I.M., Stamoulis, K., Caputo, R., Koukouvelas, I., Chatzipetros, A., Pavlides, S., Gallousi, C., Papachristodoulou, C., Ioannides, K., 2016. Middle–Late Holocene earthquake history of the Gyrtoni Fault, Central Greece: Insight from optically stimulated luminescence (OSL) dating and paleoseismology. Tectonophysics 687, 14–27. doi:10.1016/j.tecto.2016.08.015

Valkaniotis, S., Betzelou, K., Zygouri, V., Koukouvelas, I., Ganas, A., 2015. Late Quaternary tectonic activity and paleoseismicity of the Eastern Messinia Fault Zone, SW Peloponessus (Messinia, Greece)., in: EGU General Assembly Conference Abstracts. p. 13215.

Velitzelos, E., Zouros, N., 1998. New results on the petrified forest of Lesvos. Δελτίον Της Ελληνικής Γεωλογικής Εταιρίας 32, 133–142.

Wallace, R.E., 1977. Profiles and ages of young fault scarps, north-central Nevada. Geol. Soc. Am. Bull. 88, 1267–1281. doi:10.1130/0016-7606(1977)88<1267:PAAOYF>2.0.CO;2

Wiatr, T., Reicherter, K., Papanikolaou, I., Fernandez-Steeger, T., Mason, J., 2013. Slip vector analysis with high resolution t-LiDAR scanning. Elsevier, Tectonophysics 608, 947–957.

Wilkinson, M., 2012. The use of Terrestrial Laser Scanning in characterizing active tectonic processes from postseismic slip to the long term growth of normal faults (Doctoral). Durham University.

Wilkinson, M., McCaffrey, K.J.W., Roberts, G., Cowie, P.A., Phillips, R.J., Michetti, A.M., Vittori, E., Guerrieri, L., Blumetti, A.M., Bubeck, A., Yates, A., Sileo, G., 2010. Partitioned postseismic deformation associated with the 2009 Mw 6.3 L'Aquila earthquake surface rupture measured using a terrestrial laser scanner. Geophys. Res. Lett. 37, L10309. doi:10.1029/2010GL043099

Zouros, N., 2010. Lesvos Petrified Forest geopark, Greece: geoconservation, Geotourism and Local development.

Ζούρος, Ν., Βελιτζέλος, Ε., Βαλιάκος, Η., Λαμπάκη, Ο., 2007. The Plaka petrified forest park in western Lesvos - Grecee. Δελτίον Της Ελληνικής Γεωλογικής Εταιρίας 40, 1880–1891.

Appendix

Note: In this section of the Thesis the cross sections of the Stavrakia and Gyrtoni fault escarpment are displayed in Excel format. The name on each cross section displays the point cloud it belongs first and then the number it has on the Fig. 29-31 for Stavrakia and Fig. 40 for Gyrtoni. Areas of high value anomalies on the charts are due to cite vegetation and therefore were ignored. The charts were first normalized before any information was extracted from them.

Stavrakia Cross Sections

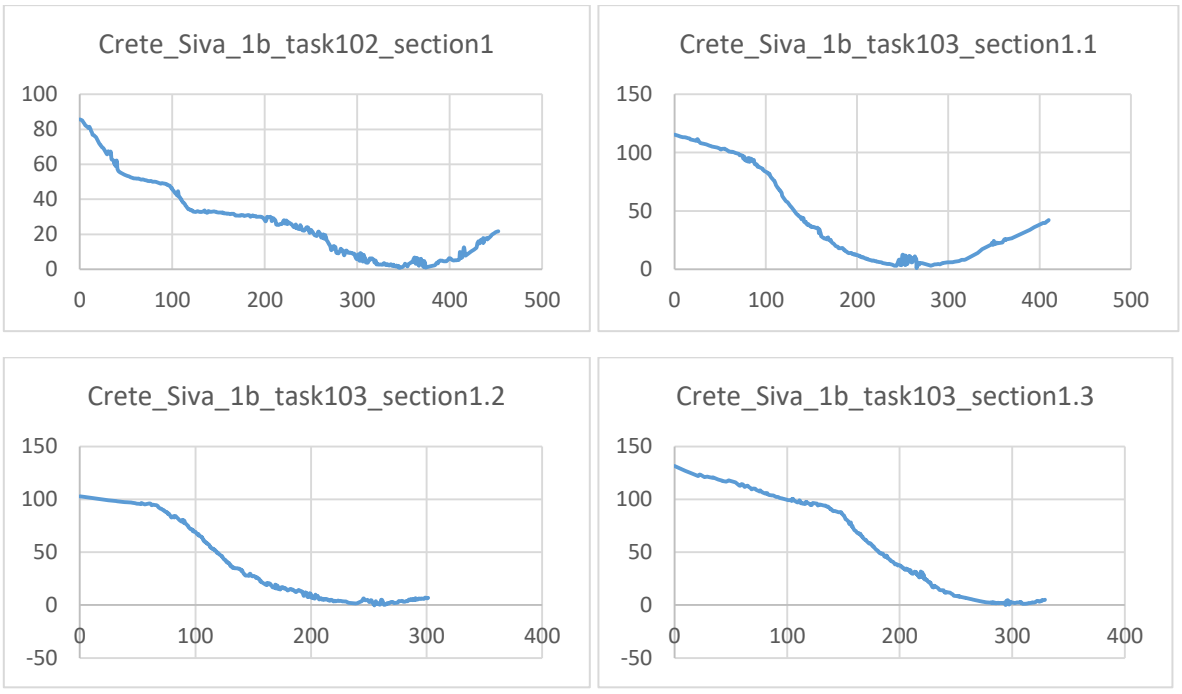

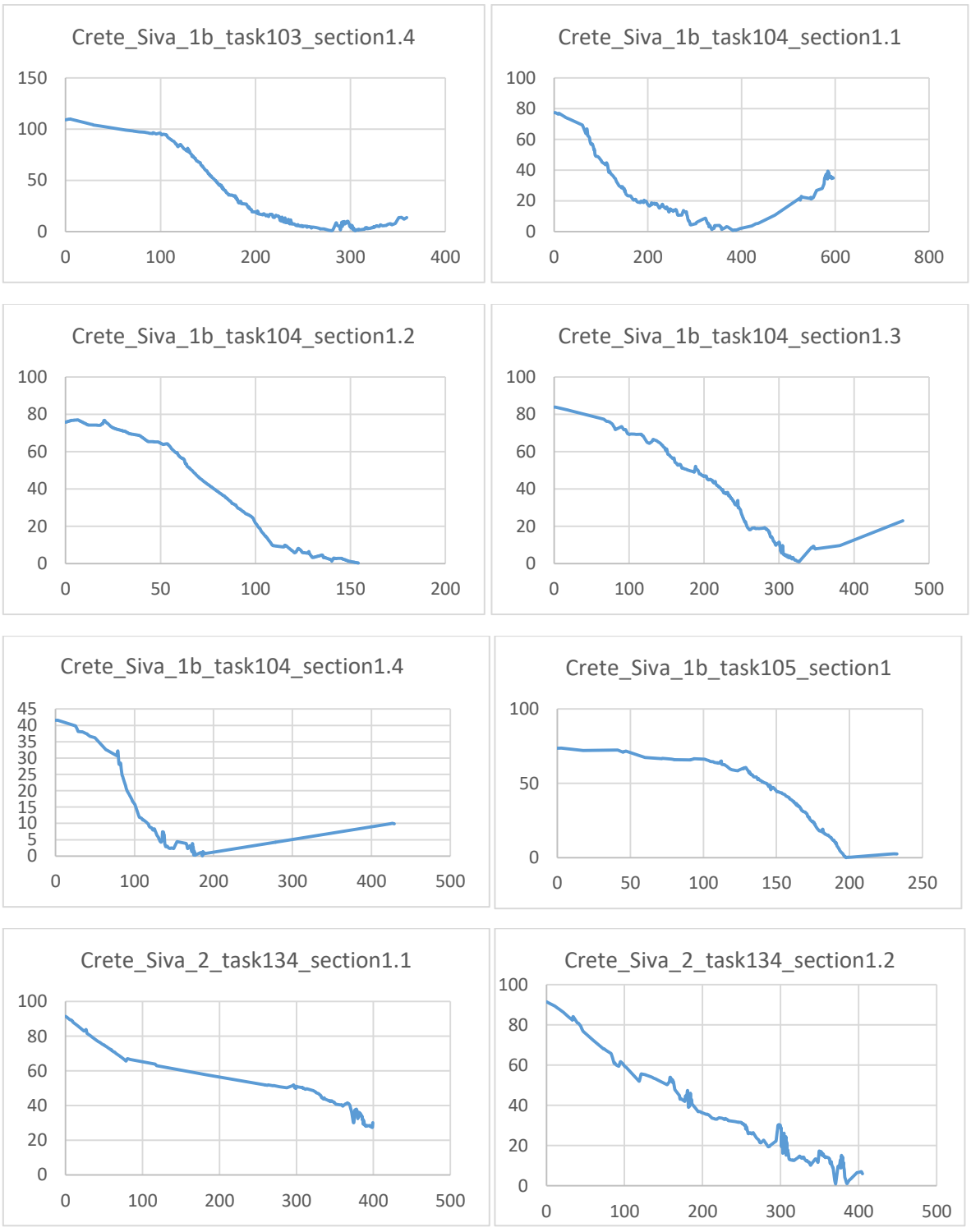
Crete_Siva_1b_task103_section1.4
150
100
50
0
0
100
200
300
400
Crete_Siva_1b_task104_section1.1
100
80
60
40
20
0
0
200
400
600
800
Crete_Siva_1b_task104_section1.2
100
80
60
40
20
0
0
50
100
150
200
Crete_Siva_1b_task104_section1.3
100
80
60
40
20
0
0
100
200
300
400
500
Crete_Siva_1b_task104_section1.4
45
40
35
30
25
20
15
10
5
0
0
100
200
300
400
500
Crete_Siva_1b_task105_section1
100
50
0
0
50
100
150
200
250
Crete_Siva_2_task134_section1.1
100
80
60
40
20
0
0
100
200
300
400
500
Crete_Siva_2_task134_section1.2
100
80
60
40
20
0
0
100
200
300
400
500

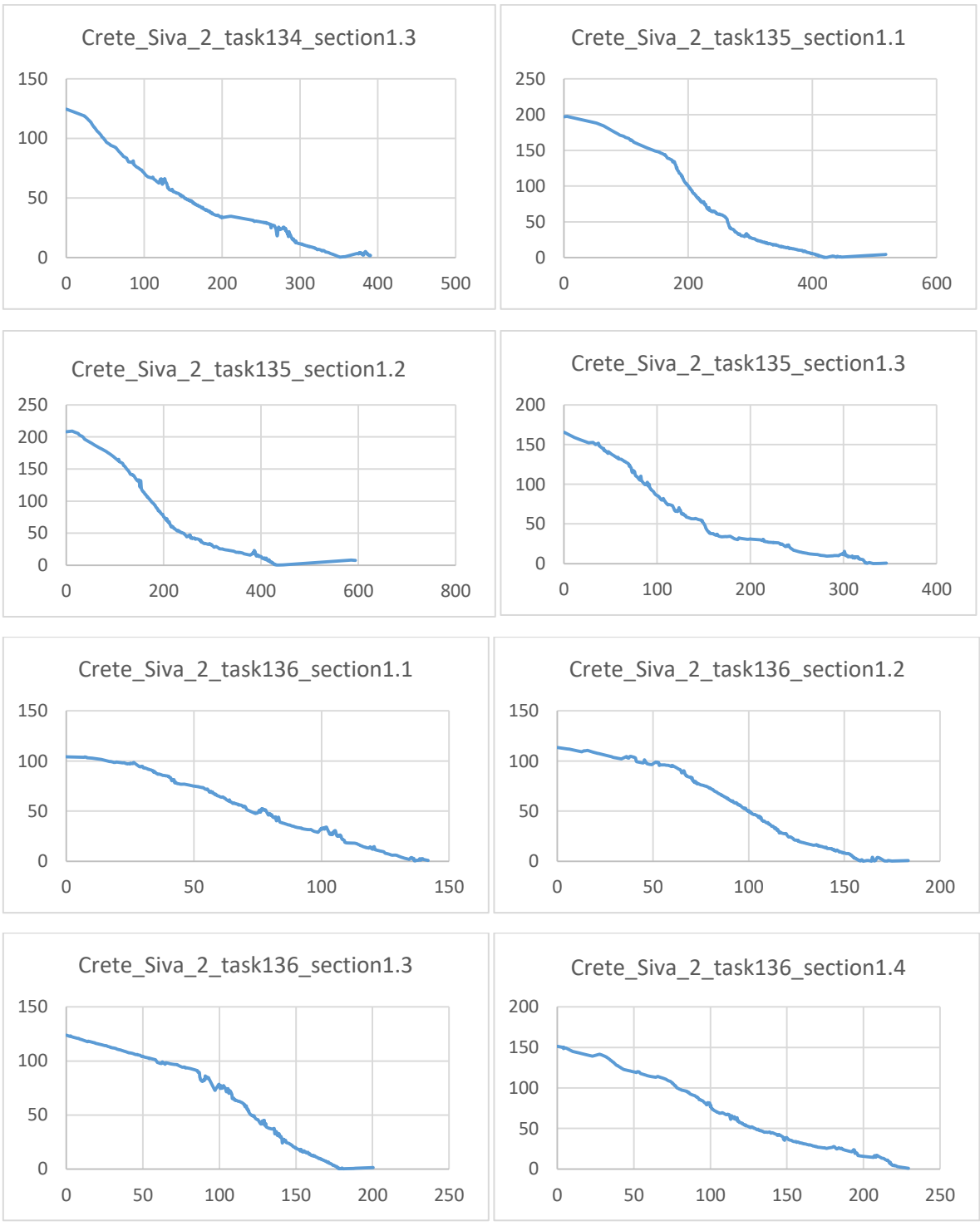
Crete_Siva_2_task134_section1.3
150
100
50
0
0
100
200
300
400
500
Crete_Siva_2_task135_section1.1
250
200
150
100
50
0
0
200
400
600
Crete_Siva_2_task135_section1.2
250
200
150
100
50
0
0
200
400
600
800
Crete_Siva_2_task135_section1.3
200
150
100
50
0
0
100
200
300
400
Crete_Siva_2_task136_section1.1
150
100
50
0
0
50
100
150
Crete_Siva_2_task136_section1.2
150
100
50
0
0
50
100
150
200
Crete_Siva_2_task136_section1.3
150
100
50
0
0
50
100
150
200
250
Crete_Siva_2_task136_section1.4
200
150
100
50
0
0
50
100
150
200
250

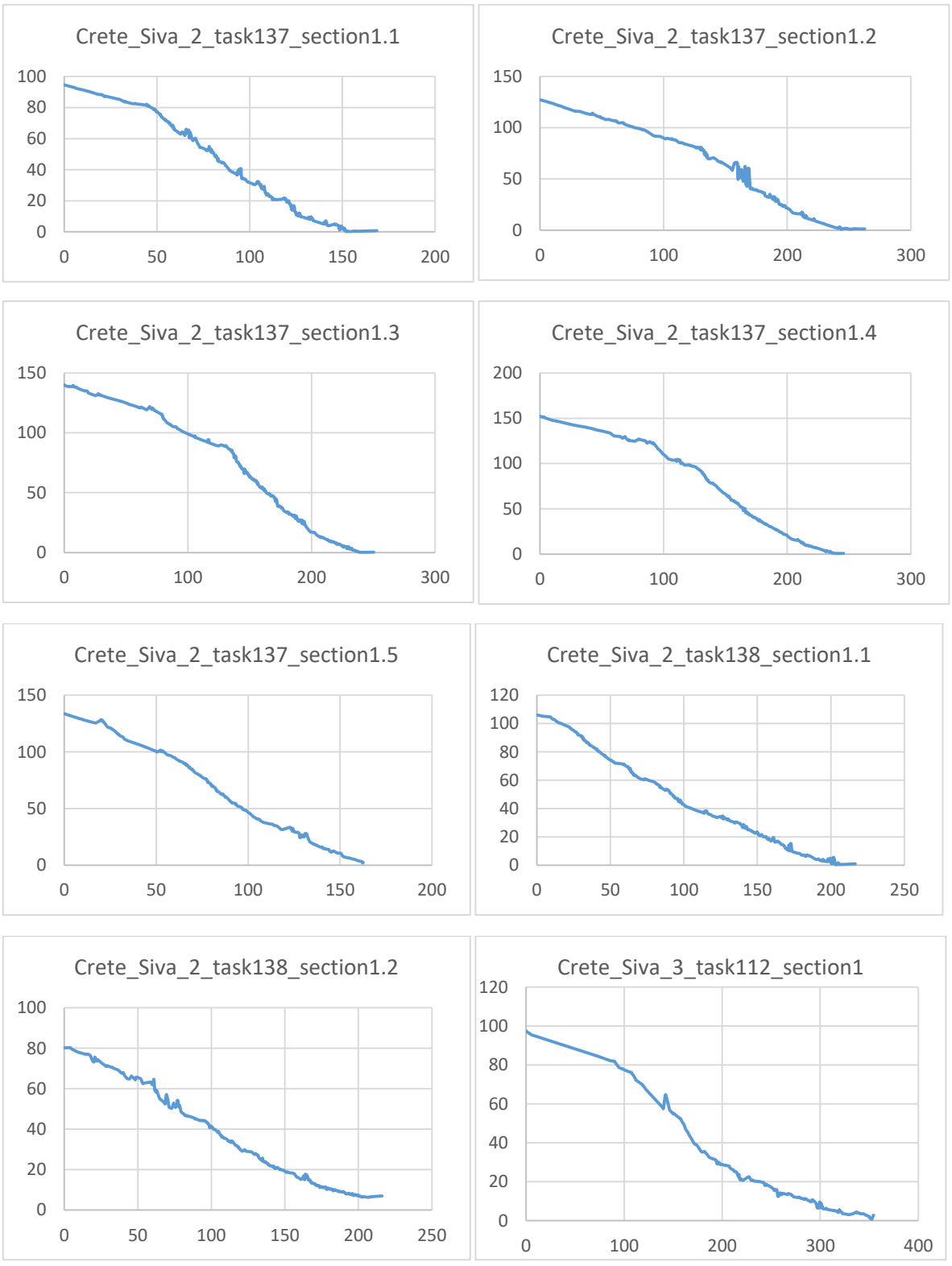
Crete_Siva_2_task137_section1.1
100
80
60
40
20
0
0
50
100
150
200
Crete_Siva_2_task137_section1.2
150
100
50
0
0
100
200
300
Crete_Siva_2_task137_section1.3
150
100
50
0
0
100
200
300
Crete_Siva_2_task137_section1.4
200
150
100
50
0
0
100
200
300
Crete_Siva_2_task137_section1.5
150
100
50
0
0
50
100
150
200
Crete_Siva_2_task138_section1.1
120
100
80
60
40
20
0
0
50
100
150
200
250
Crete_Siva_2_task138_section1.2
100
80
60
40
20
0
0
50
100
150
200
250
Crete_Siva_3_task112_section1
120
100
80
60
40
20
0
0
100
200
300
400

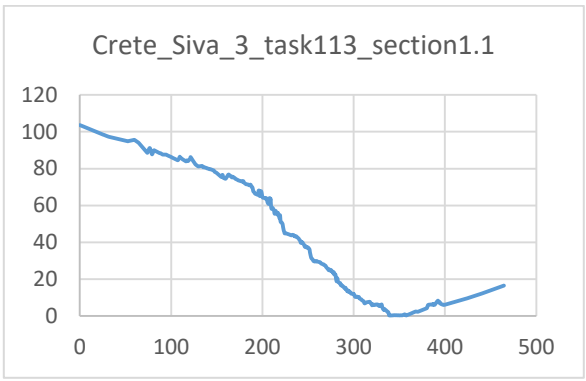
Crete_Siva_3_task113_section1.1
120
100
80
60
40
20
0
0
100
200
300
400
500

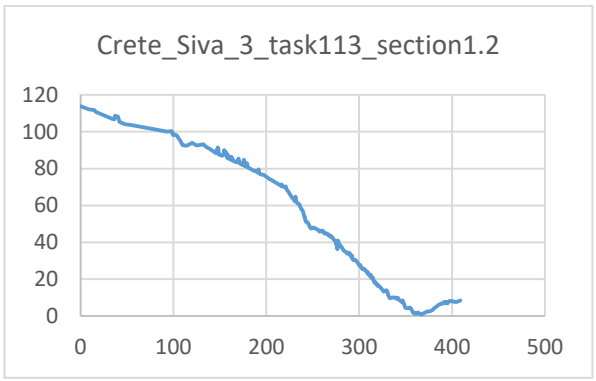
Crete_Siva_3_task113_section1.2
120
100
80
60
40
20
0
0
100
200
300
400
500

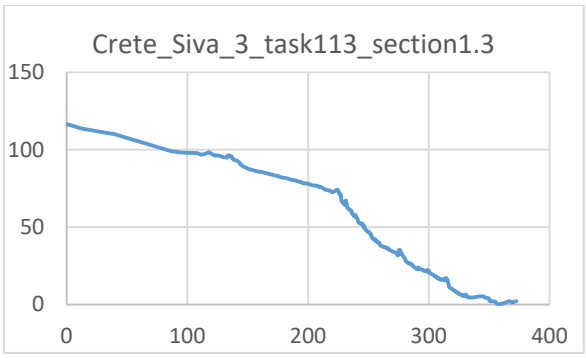
Crete_Siva_3_task113_section1.3
150
100
50
0
0
100
200
300
400

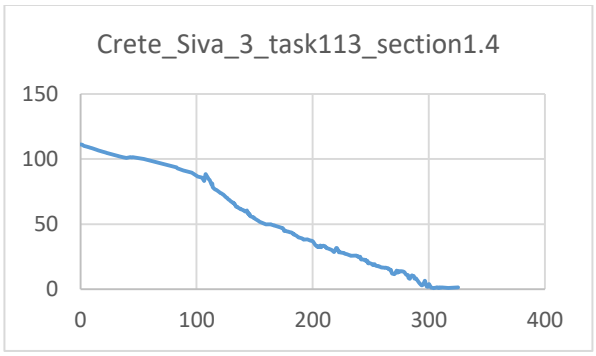
Crete_Siva_3_task113_section1.4
150
100
50
0
0
100
200
300
400

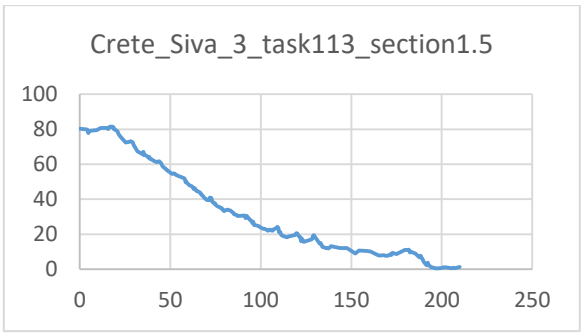
Crete_Siva_3_task113_section1.5
100
80
60
40
20
0
0
50
100
150
200
250

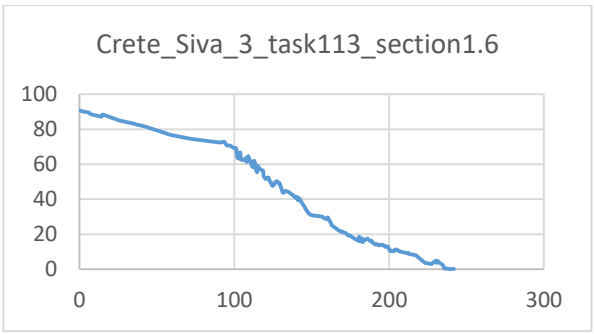
Crete_Siva_3_task113_section1.6
100
80
60
40
20
0
0
100
200
300

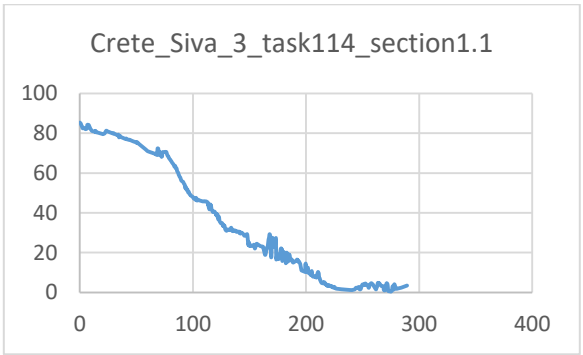
Crete_Siva_3_task114_section1.1
100
80
60
40
20
0
0
100
200
300
400

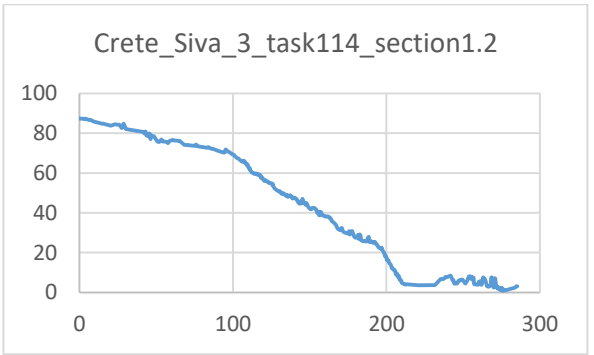
Crete_Siva_3_task114_section1.2
100
80
60
40
20
0
0
100
200
300

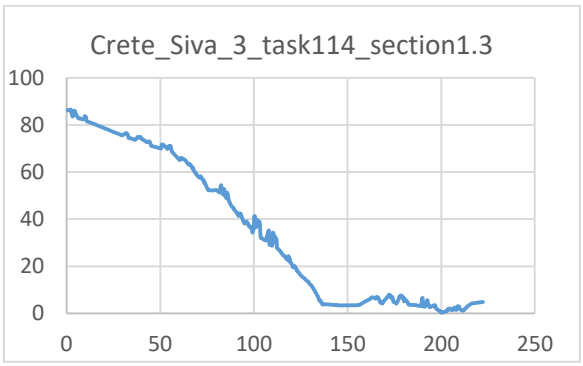
Crete_Siva_3_task114_section1.3
100
80
60
40
20
0
0
50
100
150
200
250

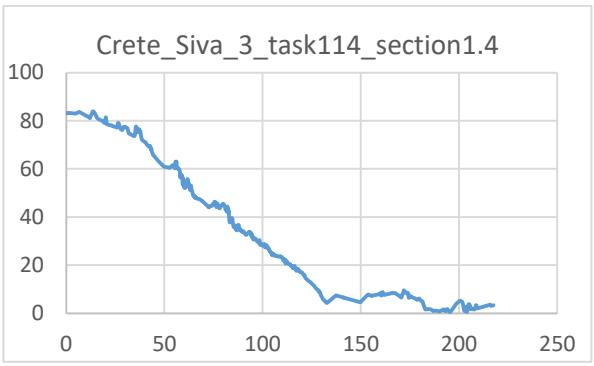
Crete_Siva_3_task114_section1.4
100
80
60
40
20
0
0
50
100
150
200
250

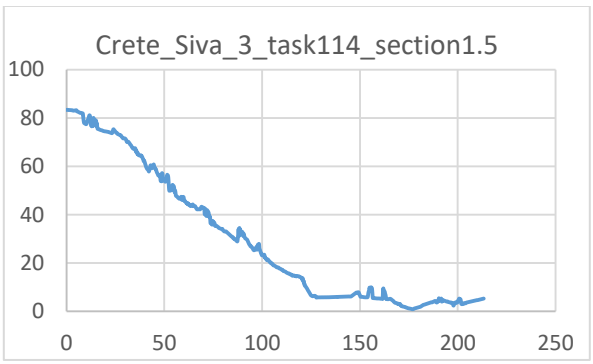
Crete_Siva_3_task114_section1.5
100
80
60
40
20
0
0
50
100
150
200
250

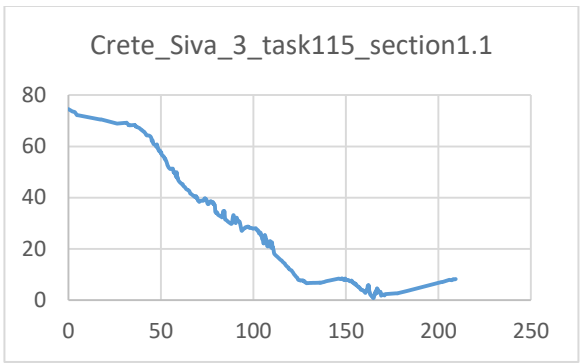
Crete_Siva_3_task115_section1.1
80
60
40
20
0
0
50
100
150
200
250

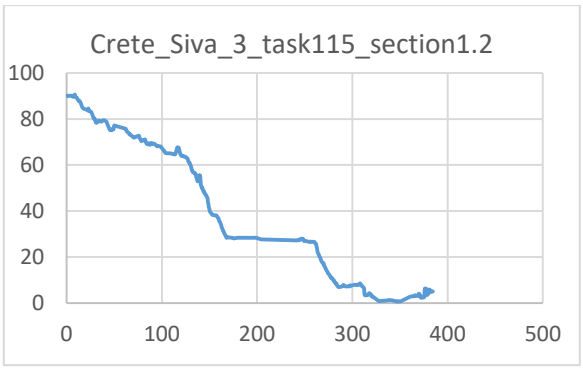
Crete_Siva_3_task115_section1.2
100
80
60
40
20
0
0
100
200
300
400
500

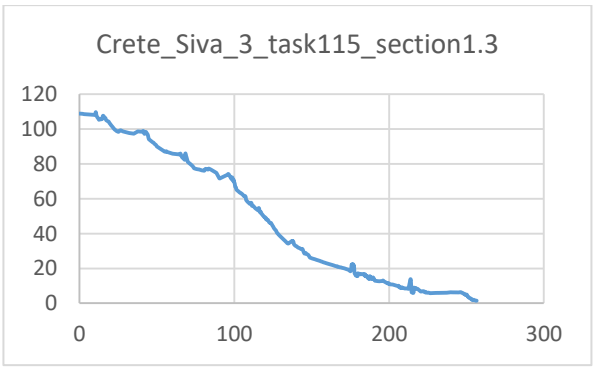
Crete_Siva_3_task115_section1.3
120
100
80
60
40
20
0
0
100
200
300

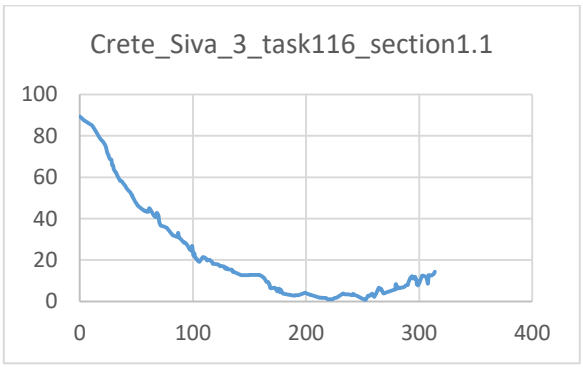
Crete_Siva_3_task116_section1.1
100
80
60
40
20
0
0
100
200
300
400

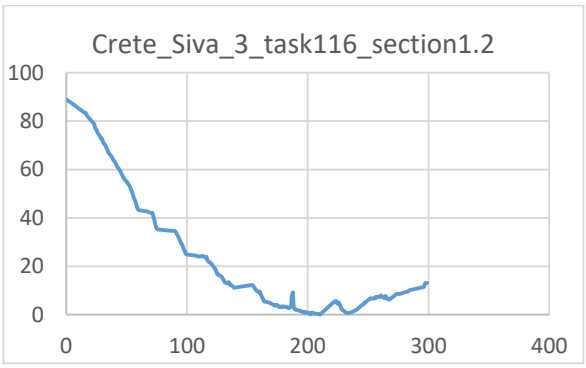
Crete_Siva_3_task116_section1.2
100
80
60
40
20
0
0
100
200
300
400

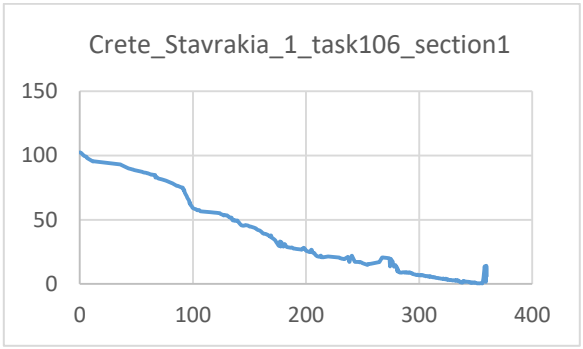
Crete_Stavrakia_1_task106_section1
150
100
50
0
0
100
200
300
400

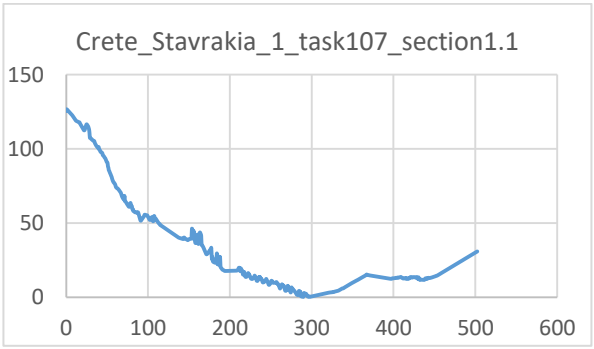
Crete_Stavrakia_1_task107_section1.1
150
100
50
0
0
100
200
300
400
500
600

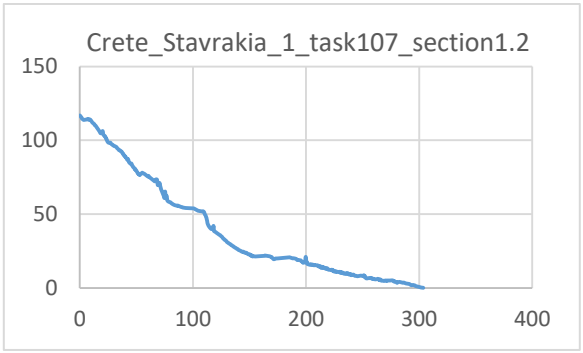
Crete_Stavrakia_1_task107_section1.2
150
100
50
0
0
100
200
300
400

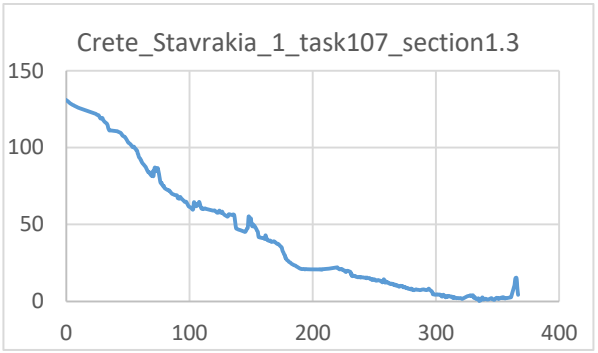
Crete_Stavrakia_1_task107_section1.3
150
100
50
0
0
100
200
300
400

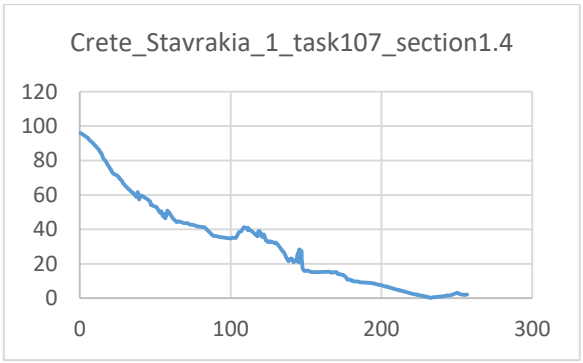
Crete_Stavrakia_1_task107_section1.4
120
100
80
60
40
20
0
0
100
200
300

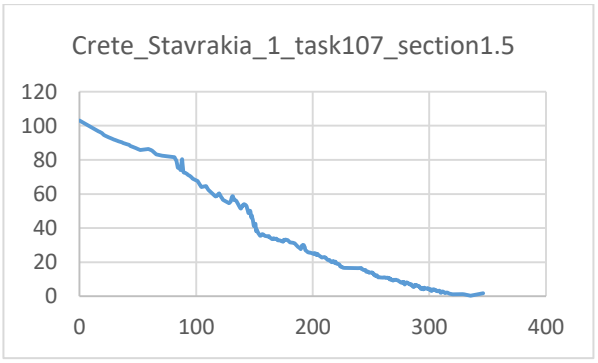
Crete_Stavrakia_1_task107_section1.5
120
100
80
60
40
20
0
0
100
200
300
400


Crete_Stavrakia_1_task108_section1.1
120
100
80
60
40
20
0
0
50
100
150
200
250
300


Crete_Stavrakia_1_task108_section1.2
120
100
80
60
40
20
0
0
100
200
300

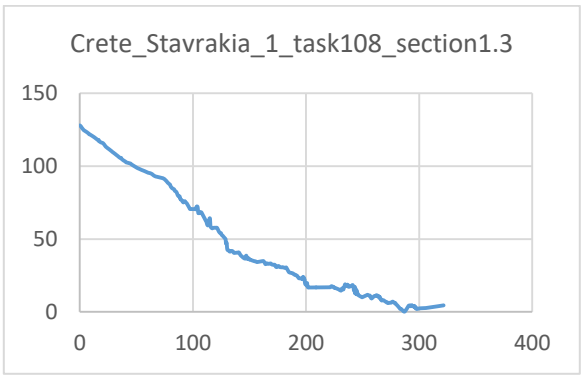
Crete_Stavrakia_1_task108_section1.3
150
100
50
0
0
100
200
300
400

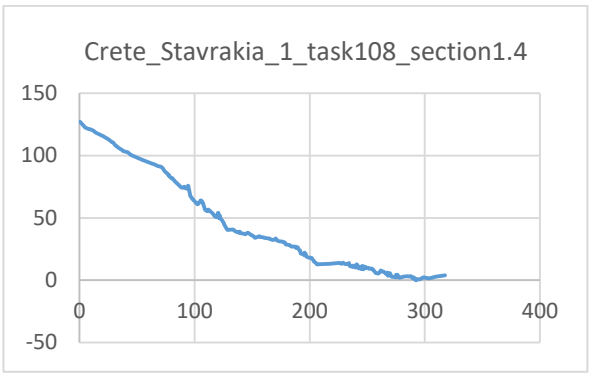
Crete_Stavrakia_1_task108_section1.4
150
100
50
0
-50
0
100
200
300
400

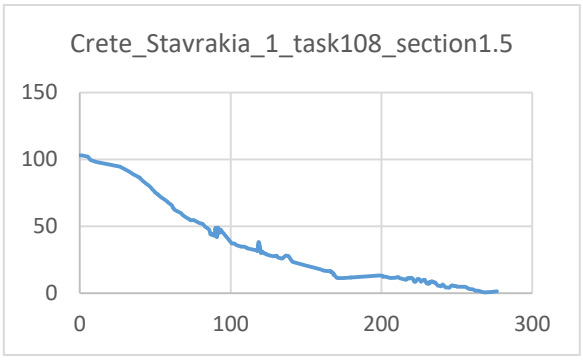
Crete_Stavrakia_1_task108_section1.5
150
100
50
0
0
100
200
300


Crete_Stavrakia_1_task109_section1.1
150
100
50
0
0
100
200
300

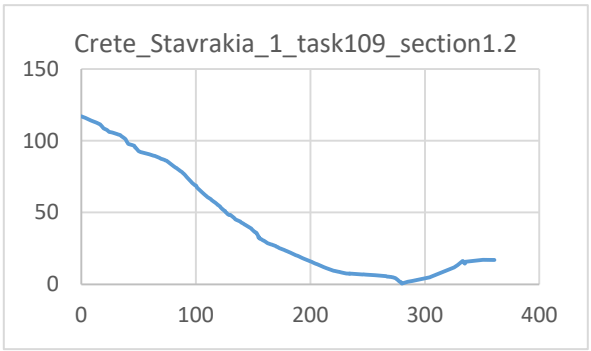
Crete_Stavrakia_1_task109_section1.2
150
100
50
0
0
100
200
300
400

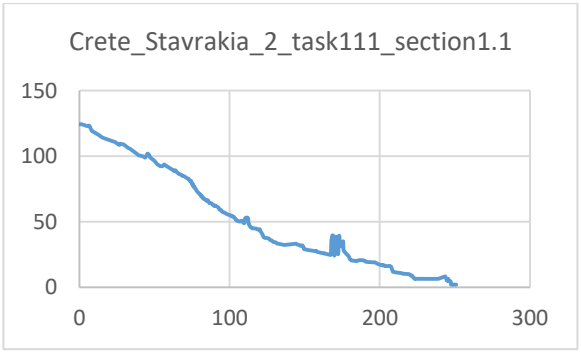
Crete_Stavrakia_2_task111_section1.1
150
100
50
0
0
100
200
300

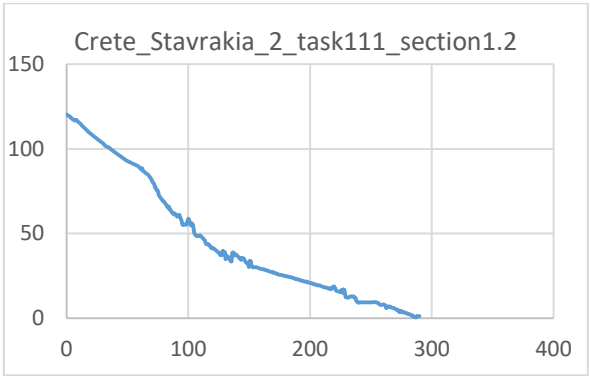
Crete_Stavrakia_2_task111_section1.2
150
100
50
0
0
100
200
300
400

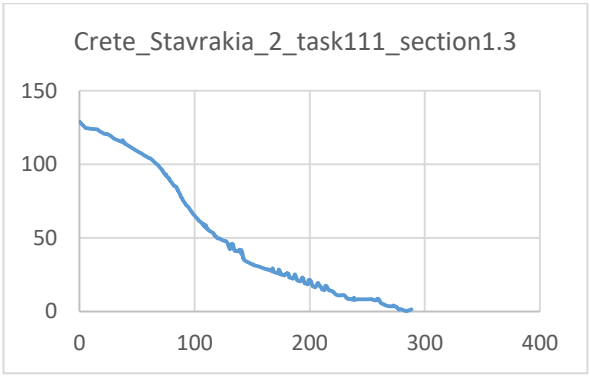
Crete_Stavrakia_2_task111_section1.3
150
100
50
0
0
100
200
300
400


Crete_Stavrakia_2_task111_section1.4
150
100
50
0
0
100
200
300
400

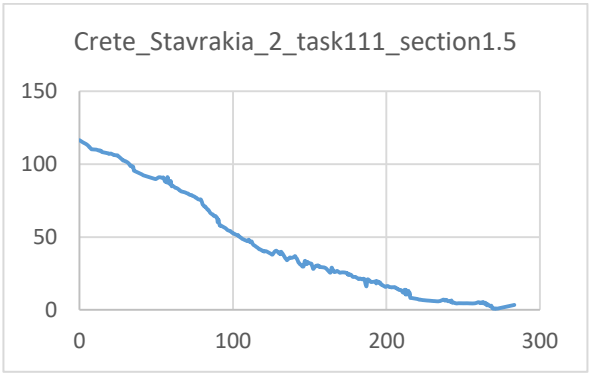
Crete_Stavrakia_2_task111_section1.5
150
100
50
0
0
100
200
300

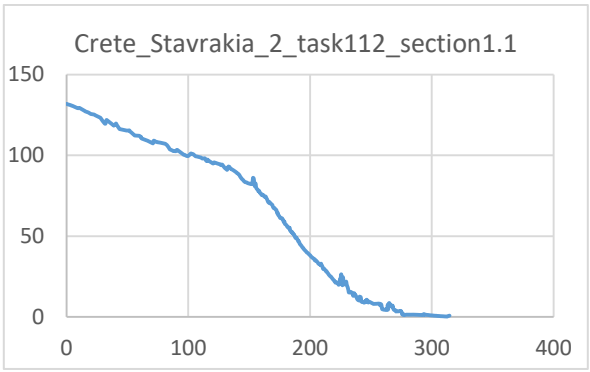
Crete_Stavrakia_2_task112_section1.1
150
100
50
0
0
100
200
300
400


Crete_Stavrakia_2_task112_section1.2
150
100
50
0
0
100
200
300
400

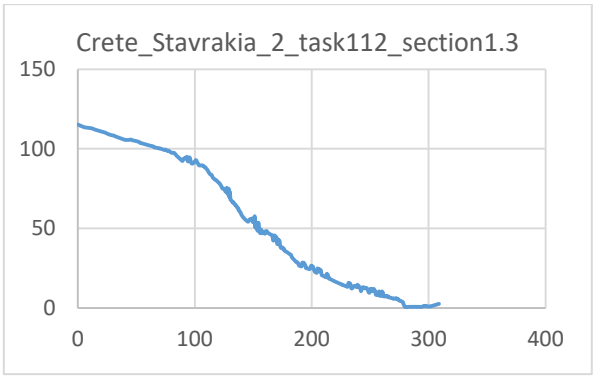
Crete_Stavrakia_2_task112_section1.3
150
100
50
0
0
100
200
300
400


Crete_Stavrakia_2_task112_section1.4
150
100
50
0
0
100
200
300
400

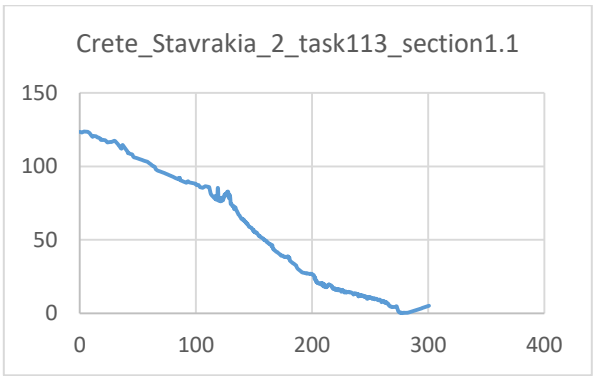
Crete_Stavrakia_2_task113_section1.1
150
100
50
0
0
100
200
300
400


Crete_Stavrakia_2_task113_section1.2
150
100
50
0
0
100
200
300
400

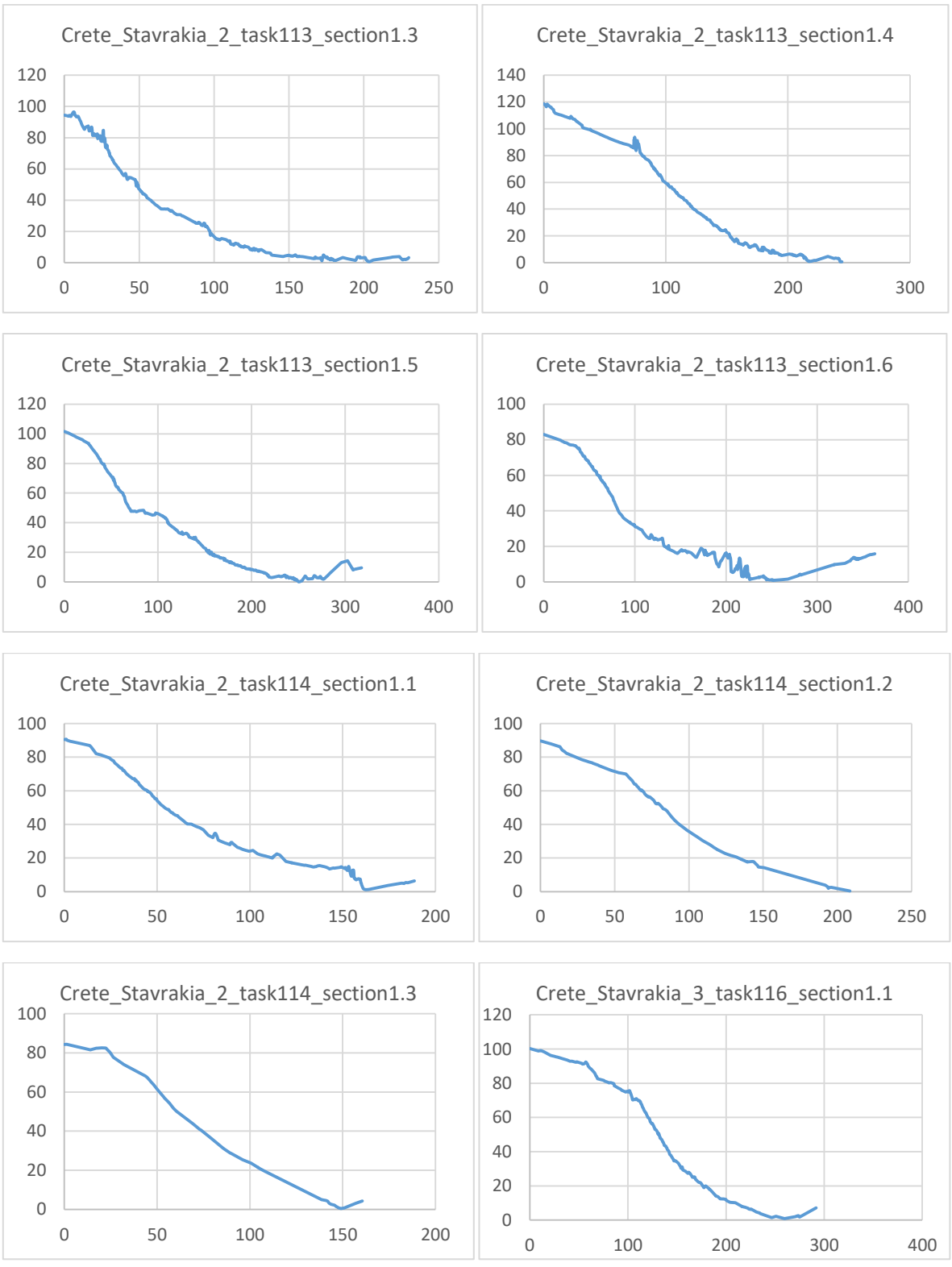
Crete_Stavrakia_2_task113_section1.3
120
100
80
60
40
20
0
0
50
100
150
200
250
Crete_Stavrakia_2_task113_section1.4
140
120
100
80
60
40
20
0
0
100
200
300
Crete_Stavrakia_2_task113_section1.5
120
100
80
60
40
20
0
0
100
200
300
400
Crete_Stavrakia_2_task113_section1.6
100
80
60
40
20
0
0
100
200
300
400
Crete_Stavrakia_2_task114_section1.1
100
80
60
40
20
0
0
50
100
150
200
Crete_Stavrakia_2_task114_section1.2
100
80
60
40
20
0
0
50
100
150
200
250
Crete_Stavrakia_2_task114_section1.3
100
80
60
40
20
0
0
50
100
150
200
Crete_Stavrakia_3_task116_section1.1
120
100
80
60
40
20
0
0
100
200
300
400

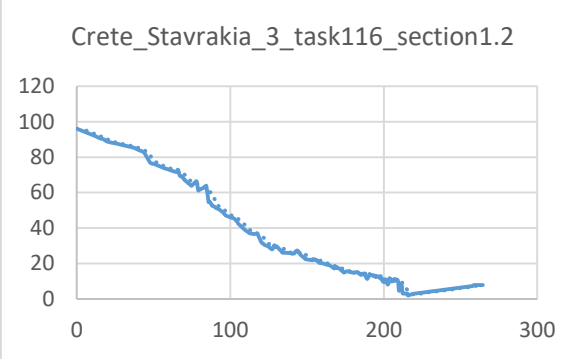
Crete_Stavrakia_3_task116_section1.2
120
100
80
60
40
20
0
0
100
200
300

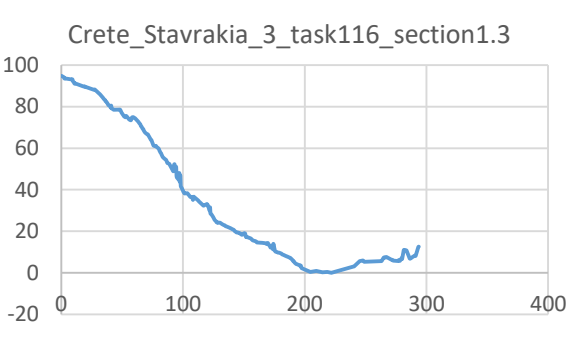
Crete_Stavrakia_3_task116_section1.3
100
80
60
40
20
0
-20
0
100
200
300
400

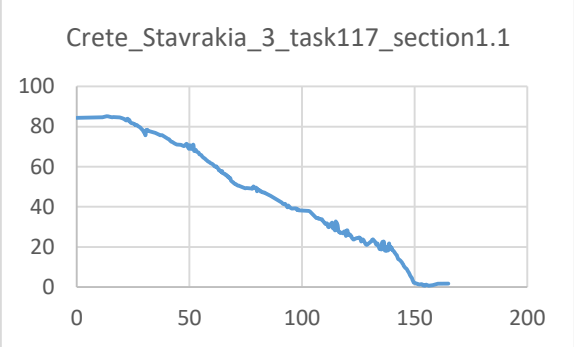
Crete_Stavrakia_3_task117_section1.1
100
80
60
40
20
0
0
50
100
150
200


Crete_Stavrakia_3_task117_section1.2
200
0
0
200
400
600
800
1000


Crete_Stavrakia_3_task117_section1.3
60
40
20
0
0
100
200
300
400


Crete_Stavrakia_3_task117_section1.4
100
80
60
40
20
0
0
50
100
150
200
250
300

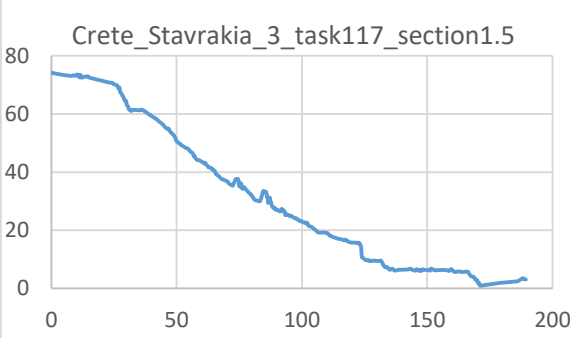
Crete_Stavrakia_3_task117_section1.5
80
60
40
20
0
0
50
100
150
200

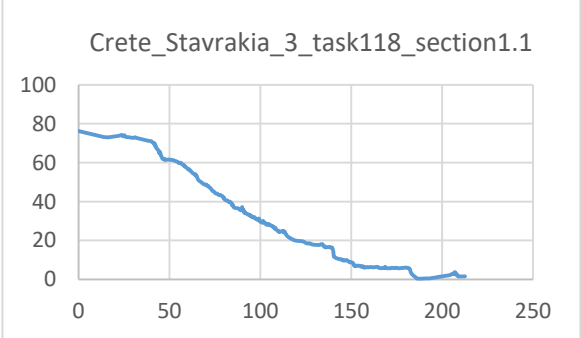
Crete_Stavrakia_3_task118_section1.1
100
80
60
40
20
0
0
50
100
150
200
250

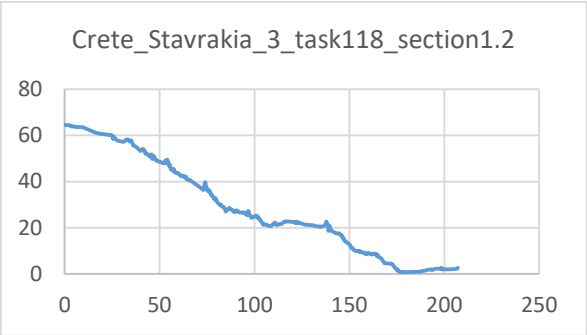
Crete_Stavrakia_3_task118_section1.2
80
60
40
20
0
0
50
100
150
200
250


Crete_Stavrakia_3_task118_section1.3
60
40
20
0
0
50
100
150
200
250

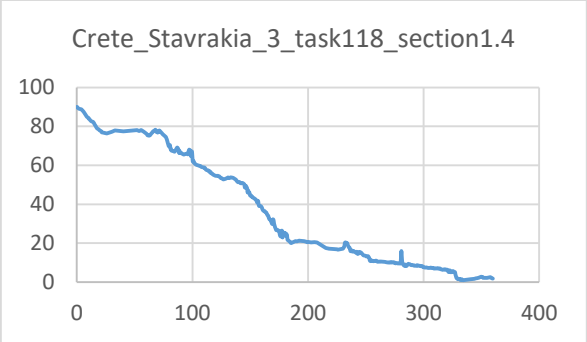
Crete_Stavrakia_3_task118_section1.4
100
80
60
40
20
0
0
100
200
300
400

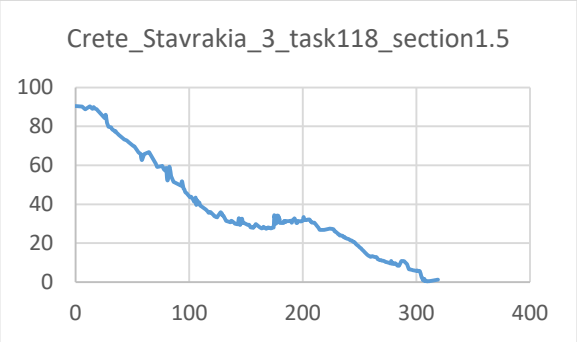
Crete_Stavrakia_3_task118_section1.5
100
80
60
40
20
0
0
100
200
300
400


Crete_Stavrakia_3_task119_section1.1
50
40
30
20
10
0
0
50
100
150
200


Crete_Stavrakia_3_task119_section1.2
50
40
30
20
10
0
0
50
100
150
200

Gyrtoni Cross Sections